1-1-2012

The Effect Of Biodiesel Blends On A Multi-Cylinder Engine And The Impact On Aftertreatment

Amy Peterson
Wayne State University,

THE EFFECT OF BIODIESEL BLENDS ON A MULTI-CYLINDER ENGINE AND THE IMPACT ON AFTERTREATMENT

by

AMY PETERSON

DISSERTATION

Submitted to the Graduate School

of Wayne State University,

Detroit, Michigan

in partial fulfillment of the requirements

for the degree of

DOCTOR OF PHILOSOPHY

2013

MAJOR: MECHANICAL ENGINEERING

Approved by:

_____
Advisor Date

_____

_____

_____

DEDICATION

To my parents, Bill and MaryAnn Symons, and to my family, Todd and Alexis

- with your support I can do anything.

ACKNOWLEDGMENTS

I want to thank Wayne State University and the Department of Mechanical Engineering for the opportunity to study and conduct research with such a diverse and talented group of individuals. The administrative, machine shop and support staff have been so helpful in answering questions and providing their much needed guidance.

I want to thank the group members both past and present for their support and help in the lab and out. Many of the past group members helped me focus and get started in the right direction. Dr. Xingbin Xie, Dr. Hoisan Kim, Dr. K.S. Im, Atsushi Matsumoto, Ming Li, and Dr. Peng Quan have provided me with experiences and instruction that will not be forgotten. I would like to give a very special thank you to Po-I Lee for his help, knowledge, and friendship during all of the trials and successes that we had in lab 1354.

I want to thank my committee members; Dr. Singh, Dr. Henien, and Dr. Ng for their time and guidance through this process. I also want to thank my advisor; Dr. Ming-Chia Lai for all his encouragement, patience, and understanding. He has been my mentor and teacher during my time here at Wayne State and his extensive knowledge and dedication has made my research possible as well as enjoyable.

Finally I would also like to thank my family for their continuous support and encouragement. My parents, husband Todd and daughter Alexis have inspired me to work hard and to enjoy every moment.

TABLE OF CONTENTS

LIST OF TABLES

LIST OF FIGURES

CHAPTER 1

INTRODUCTION

Recently, topics including global warming, increased environmental awareness, recycling, and organically produced meat and vegetables have been prevalent in the media and research arenas. The rapidly increasing cost for fossil fuels and the pursuit of environmental conservation has brought about the interest in a renewable and clean burning fuel, specifically biodiesel. Biodiesel, or vegetable oil ester as it was originally referred to, has been improving and progressing since the early 1900's. A speech given by Rudolph Diesel in 1912 stated that ". . . the use of vegetable oils for engine fuels may seem insignificant today, but such oils may become, in the course of time, as important as petroleum and the coal-tar products of the present time" [2]. The use of raw vegetable oil was known during Diesel's time to start and power an internal combustion diesel engine. In fact, the French Otto Company designed an engine that was powered by raw peanut oil at the Paris Exposition of 1900. Fortunately, significant advancement in the understanding of raw vegetable oil as a fuel as well as converting it to ethyl or methyl esters, now known as biodiesel, has been evolving for nearly a century after.

The most prevalent growth for vegetable oil derived fuels is seen during the late 70's after implementation of the OPEC oil embargo act. The embargo act nearly doubled the price per barrel of petroleum overnight, escalating the need for research of a viable alternative diesel fuel.

In 1982 a conference held in Fargo, North Dakota, sponsored by the American Society of Agricultural Engineers (ASAE), published a collection of papers focusing on the use of vegetable oil and the conversion to methyl esters as a feasible fuel for application in diesel engines. Although the majority of the papers concentrated on using raw vegetable oil, research done by The Agricultural Research Service in Peoria Illinois, USDA [3], Deere and Company [4], and The University of North Dakota [5] focused on the use of vegetable oil esters as a fuel. In fact the first use of vegetable oil esters to fuel a diesel engine in the United States was reported by Fort et al. [6] with the use of cottonseed methyl esters.

Vegetable oil esters obtained through the process of transesterification, although well known and documented at this time, was further advanced by the published work of Hawkins et al. [7] documenting the production of fuel quality vegetable esters using sunflower oil. The first industrial biodiesel pilot plant (1987) and industrial plant (1989) was constructed by an Austrian Company, Gaskoks with a capacity of 30,000 metric tons of rapeseed methyl ester per year.

The objective of the following work is predicated on the potential marketing of biodiesel blends, up to 20% by volume, without modification to standard production available engines to be used by the average consumer. The NextEnergy Biodiesel program is a collaborative effort involving a variety of disciplines and expertise. Objectives include developing manufacturing methods for soy-based biodiesel, evaluate and record parameters such as cetane number, oxidative stability, and lubricity made from different feedstocks to be used for engine testing. Evaluate selected fuels to be blended with ULSD and tested in single and multi-cylinder engines. To evaluate the impact of biodiesel blends on a variety of aftertreatment devices with respect to performance and effectiveness. Finally, to record all experimental findings in one easily accessible location and cultivate the possibility of worldwide use which will accelerate the aid in the development of ASTM standards for biodiesel production and storage. The proceeding work focuses on results from a multi-cylinder engine coupled with a diesel oxidation catalyst, diesel particulate filter and a selective catalytic reductive catalyst and the effect that biodiesel blends has on their performance and effectiveness.

CHAPTER 2

LITERATURE REVIEW AND BACKGROUND

In this chapter, background information about biodiesel, fuel properties, biodiesel emissions, and combustion strategies are provided. The first section presents information of the structure and transesterification of biodiesel followed by an explanation of NOx and PM formations. The second section of this chapter is dedicated to different aftertreatment devices and the effect of biodiesel fuel found in literature on these emission control devices. The final section of this chapter covers low temperature combustion and the resulting emissions.

2.1 Chemical Structure and Composition of Biodiesel

A variety of different feedstocks can be used to make biodiesel. These feedstocks include vegetable oils such as soybean, cottonseed, rapeseed, and algae as well as animal fats such as poultry fat (lard) and yellow grease. In order to further explain the chemical composition of biodiesel, it is important to investigate the chemical structure of the vegetable oils or animal fats used in the transesterification process to produce biodiesel. Figure 2.1 shows the chemical structure of vegetable oil, also called a triclyglyerol, or triglyceride.

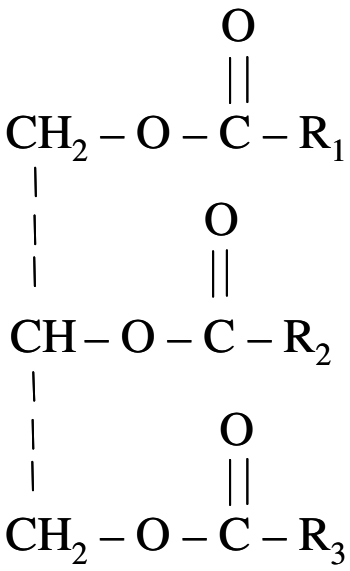

Figure 2.1. The chemical structure of vegetable oil [8]

A Triglyceride is composed of glycerin esters with long chain acids, called fatty acids [9]. The long hydrocarbon chains are represented by R1, R2, and R3 in the figure.

Triglycerides which are solid at room temperature are called fats, typically derived from animals and contain saturated fatty acids (containing no carbon-carbon double bonds). Saturated fatty acids are tightly packed together giving the triglycerides a relatively high melting point. Triglycerides which are liquid at room temperature are called oils. These oils are typically derived from plants such as soybean, peanuts or cotton seed and are composed of triglycerides with unsaturated fatty acids (containing carbon-carbon double bonds). They do not pack tightly together yielding a lower melting point and yielding a liquid product when at room temperature.

Fatty acids compose the majority of mass of a triglyceride molecule; therefore

they have the most influence on the properties of different bio-fuels. Depending on the oil or fat used, the fatty acid composition differs as well as the carbon chain length and the number of carbon-carbon double bonds. The most common fatty acid chains in vegetable oils and animal fats are shown in table 2.1. The structures of these chains are designated by two numbers separated by a colon. The first number indicates the number of carbon atoms in the chain and the second number indicates the number of double bonds. The difference in the physical properties can be seen specifically in melting point, where those containing more palmitic fatty acids have a higher melting point than those having a higher percentage of Linolenic fatty acids.

Fatty Acid	Structure	Cotton Seed	Safflower	Soybean	Peanut	Lard	Yellow Grease	Melting Point
Myristic	14:0	0-2	0	0	0	1-2	2.43	
Palmitic	16:0	25-28	8.60	6-10	8-11	28	23.24	64 ℃
Stearic	18:0	0-1	0-2	2-5	2-5	12	12.96	70 ℃
Oleic	18:1	10-13	10-12	20-23	45-48	48	44.32	16 ℃
Linoleic	18:2	50-57	70-77	50-55	28-31	6	6.97	-5 ℃
Linolenic	18:3	0	0	5-6	0-1	0	0.67	-11 ℃

Table 2.1. Fatty acid composition of vegetable oils and animal fats %, by weight [8, 10, 11]

2.2 Transesterification Process

In order to reduce the viscosity of bio-fuels, a process called transesterification is used. There are three main methods to produce esters from vegetable oils and animal fats: 1. base catalyzed transesterification of the oil with alcohol, 2. Direct acid catalyzed esterification of the oil with methanol, and 3. Conversion of the oil to fatty acids, and then to Alkyl esters with acid catalysis. The majority of biodiesel made today utilizes method one with a base catalyst reaction. This method is preferred due to the low temperature and pressure, high conversion rate and low reaction time, and direct conversion to methyl ester [12].

The production of biodiesel, called transesterification, is a chemical reaction between long chain fatty acids with an alcohol such as methanol or ethanol in the presence of a catalyst to produce mono-alkyl esters (biodiesel) and glycerin. R1, R2, and R3 represent long chains of carbon and hydrogen atoms, called fatty acids. The transesterification process is shown in the following figure.

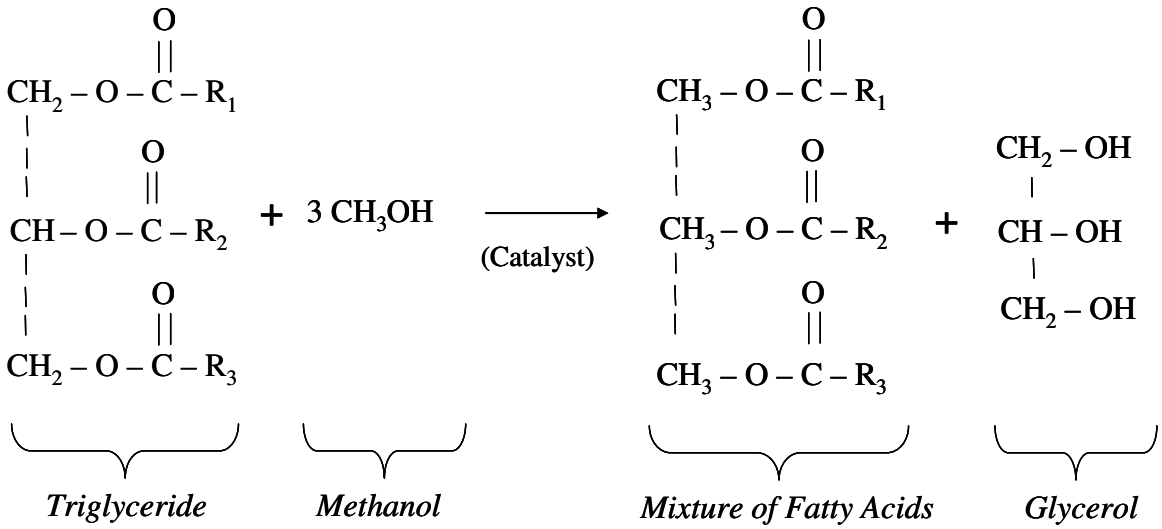

Figure 2.2. Transesterification process of triglyceride with methanol [8]

In this process, a triglyceride, which is an ester, is reacted with an alcohol (methanol) and a catalyst (KOH, $NaOCH_3$, or NaOH) the triglyceride molecule splits into two products: glycerol and a mixture of fatty acid esters called biodiesel.

2.3 Technical Background of Biodiesel

Biodiesel is defined as a mono-alkyl ester, or long chain fatty acid, derived from vegetable oils or animal fats [12]. In addition, all production biodiesel is tested and must conform to ASTM D6751 standards. Those not meeting these standards are technically not biodiesel, thereby protecting the quality and integrity of each batch of biodiesel produced and distributed for consumer use. Biodiesel or "neat" biodiesel refers to the pure fuel before it is mixed with diesel fuel. Biodiesel blends are denoted as BXX where

XX refers to the percentage by volume of biodiesel added to the diesel fuel. It is completely soluble in petroleum based diesel fuel, so biodiesel can be used as a blend and utilizes one fuel tank for both fuels. This is a unique advantage over other alternative fuels and gives the consumer the option of choosing biodiesel blends without significant engine modification.

In addition to its renewable quality, substantial research has been conducted on its reduction of harmful emissions when used to fuel compression ignition engines. Carbon Dioxide (CO_2), a leader in the increase of greenhouse gases, is consumed by the feedstocks used to produce biodiesel. Furthermore, due to the oxygenated nature of biodiesel approximately 11% by weight, this may result in more complete engine combustion and possibly lower exhaust emissions.

Further restrictions on exhaust emissions by the Environmental Protection Agency (EPA) have mandated levels of sulfur in petroleum diesel fuel to be 15ppm or less as of June 1, 2006. Unfortunately the hydrotreating process used to reduce the amount of sulfur in the fuel has lead to inadequate lubrication of internal engine components, or decreased lubricity. The lubricity of the fuel is defined as measurement of the scarring or wearing between two metal parts in contact with each other. Lubricity analysis is done using a high-frequency reciprocating rig (HFRR) or by using the scuffing load ball on cylinder evaluator (SL-BOCLE). The reduction of fuel lubricity has been linked to the removal of oxygen and nitrogen in the fuel which occurs simultaneously during sulfur removal [13, 14]. Anastopoulos et al conducted research using biodiesel blends and found a decrease in HFRR with blends as low as 0.15%-5% biodiesel by volume. However, Wadumesthrige et al found that lubricity levels sharply

increase with the addition of biodiesel fuel with maximum benefit at approximately 2 vol% with the HFRR method [15].

Despite the positives associated with replacing petroleum oil with biodiesel, there are a number of disadvantages that need further research and development. Biodiesel has a lower heating value than petroleum oil as well as a higher price/gallon due to the current production costs and feedstocks used to produce biodiesel. The fuel is shown to have increased viscosity measurement at lower temperatures making cold weather starting an important issue to research. Cold flow impacts require research of the cloud point and cold filter plugging point of biodiesel. The cloud point is defined as the temperature at which small solid crystals begin to form. The cold filter plugging point (CFPP) is defined as the temperature at which fuel will cause a fuel filter to plug due to fuel components that have begun to crystallize or gel. Furthermore, biodiesel exhibits poor oxidative stability, especially in long term storage, and can be attacked by bacteria and mold growth in the presence of water. Oxidative stability is defined as the propensity of fuels to react with oxygen at temperatures near ambient or room temperature. This reaction is often slower than that of thermal stability, changes in fuel due to increased temperatures, producing varnish deposits and sediment in the tank and engine components.

2.4 Physical Properties of Biodiesel

The properties of biodiesel and diesel fuel are quite similar. Therefore the direct application of biodiesel fuel in diesel fueled engines is a strong contender as an

alternative fuel. The table below shows variety of typical feedstocks used to make biodiesel and properties compared to ultra-low diesel fuel.

Property	ULSD	Cotton Seed	Soybean	Peanut	Lard	Yellow Grease	Choice White Grease
Kinematic Viscosity, (mm2/sec)40C	2.7	4.2	4.4	4.9	4.85	5.62	4.7
Cetane Number	42	58.3	47.2	54	63.6	57.8	58.4
Cloud Point (C)	-2	3	2-6	5	14	42	9
Pour Point (C)	-11	-3	0	-	11	12	-
Flash Point (C)	153		167	176	128	160	164
Lower Heating Value (MJ/kg)	43.9		39.8	33.6	39.9	40.0	43.0
Density (kg/m3)	0.8475		0.887	0.883	0.8762	0.8789	0.8721

Table 2.2. Physical properties of biodiesel and ULSD [16, 17]

2.5 NOx and PM Formation and effects

Internal combustion engines are a significant source contributing to the declining air quality in the United States. Diesel engines in particular emit emissions of hydrocarbons (HC), nitrogen oxides (NOx), carbon monoxide (CO), and particulate matter (PM) in addition to nonregulated emissions of Poly (cyclic)-aromatic

hydrocarbons (PAH), sulphur dioxide (SO2) and aldehydes. The following section will discuss NOx and PM emissions.

2.5.1 NOx Emissions

NOx emissions, usually defined as Nitric oxide (NO) and nitrogen dioxide (NO_2), are produced during combustion. NO is the predominant species produced due to the oxidation of Nitrogen in the atmosphere. The principal reactions governing NO formation from molecular Nitrogen in combustion near stoichiometric fuel-air mixtures are known as the extended Zeldovich mechanism and are shown below [18].

$$O + N_2 \rightarrow NO + N \quad (2.1)$$

$$N + O_2 \rightarrow NO + O \quad (2.2)$$

$$N + OH \rightarrow NO + H \quad (2.3)$$

Equations 2.1 and 2.2 are known as the Thermal NO mechanism, introduced by Ya. B. Zeldovich, and describe the NO formation in the post flame region. In 1956, Fenimore and James proposed a third reaction, equation 2.3, to address reactions that are fuel rich.

NOx emissions produced during engine combustion include nitrogen oxide, nitric acid, nitrous oxide, nitrates, and nitric oxide. The emission of these compounds into the environment has been found to adversely affect our health and environment; more specifically, the production of smog and acid rain. This increase in environmental

pollution has been found to affect breathing and respiratory function, as well as the degradation of our ground water supply due to acid rain.

Numerous researches have been conducted to determine the quantity and the effect that raw exhaust gasses have on the environment. In particular, the emissions produced using biodiesel fuel has stirred much controversy. The majority of research indicates an agreement in the reduction of SOF and particulate matter or soot. However, the effect of biodiesel fuel on NOx emissions has been reported with conflicting results. Early reported research of biodiesel blends on engine emissions indicated a reduction of CO, PM, and THC with a slight increase in NOx when compared to diesel fuel [19-28]. In response to the conflicting claims of increasing or decreasing NOx emissions with the use of biodiesel fuel, the Environment Protection Agency (EPA) published an extensive report in 2002 [22]. This report contained a compilation of data from research that was conducted by a variety of researchers regarding the effect of NOx on compression ignition engines fueled with biodiesel. The EPA report concluded that engines fueled with B20 increased NOx emissions by 2% and those fueled with B100 was increased by 10%. They further concluded that regulated emissions of carbon monoxide, total unburned hydrocarbon, and particulate matter were reduced considerably with the used of BD compared to diesel fuel. This quantification by the EPA spurred further investigation as well as questions regarding the validity of the conclusions. The National Renewable Energy Laboratory (NREL) published data regarding the effect of BD on vehicle emissions and addressed the earlier EPA report [29]. They concluded that there does not seem to be a discrepancy on NOx emissions. Although individual engines may show an increase or decrease in NOx, the net effect was very small. Furthermore, the EPA report evaluated data that was obtained from

older engines with the majority of the engines tested from the model year 1997, and some as early as 1991. In addition, nearly half of the engines reported were from one engine manufacturer. The data compiled by the EPA also contained both light and heavy duty engine testing, different testing conditions and emission testing cycles, and different biodiesel feedstocks.

Recently, more studies reporting NOx emissions to be similar and possibly lower than that of ULSD emissions based on the engine strategy used [29-33].

2.5.2 The effect of biodiesel fuel on particulate matter

Particulate matter (PM) is a complex mixture that consists of "primary" and "secondary" particles that are generated during the combustion process. Primary diesel particulates form from the carbon in the fuel and incomplete combustion of fuel hydrocarbons which occurs during combustion with oxygen deficiency or poor fuel mixing. Secondary particles are formed when diesel exhaust gases react with the atmosphere. Soot formation is predominately in the temperature range of 1000 – 2800K at pressures of 50 – 100 atm and with sufficient air to burn the fuel. Overall the entire process takes only milliseconds to complete [18].

It is well know that biodiesel (neat and blends) can reduce diesel particulate matter in the exhaust stream [22, 23, 34]. However, Boehman et al. have indicated additional benefits with respect to particulate matter [35]. Specifically, the variation in oxidative reactivity between soot derived from different fuels thereby enhancing the rate of soot oxidation. Biodiesel fuel was also found to increase the SOF content of the

particulate matter providing reactive hydrocarbons to react in the DPF. Similar investigations have shown that particulate matter produced with biodiesel fuel changes the characteristics of the insoluble fraction of particulates by altering the nanostructure of the primary soot particles, yielding a more amorphous soot structure and oxidative reactivity [35-37]. The increase in oxidative reactivity of the soot particles from biodiesel translates to an enhanced rate of soot oxidation on the diesel particulate filter during regeneration as well as a lower temperature required to achieve regeneration [35, 38, 39].

2.5.3 Effect of EGR on Combustion and Emissions

Exhaust Gas Recirculation (EGR) is a very effective method in reducing NOx emissions. The overall principle of EGR is to use part of the exhaust gas to dilute the intake air before entering the cylinder chamber. Cooled EGR, exhaust gas that uses a small EGR cooler before mixing with the intake air, will lower the in-cylinder temperature in several ways. First, the EGR gas dilutes the oxygen concentration with CO_2 and H_2O into the charge air, in order to reduce the reaction rate. Second, the EGR gas increases the specific heat of the charge air to absorb some of the energy. Ladommatos et al documented that the addition of EGR prolongs the ignition delay due to lower oxygen concentration [40]. This longer ignition delay causes the combustion process shifting toward the expansion stroke and the combustion gases spending shorter periods at high temperatures, leading to lower NOx formation. However, adverse effects due to increased EGR rates include an increase in brake specific fuel consumption, particulate matter, and CO emissions [41, 42].

2.6 Exhaust Emissions Control

The increasing restrictions on vehicle exhaust gas emissions has led to the development of numerous aftertreatment products. Products to remove harmful CO and HC emissions lead to the development of the diesel oxidation catalyst (DOC). The diesel particulate filter advanced to trap particulate matter and meet EPA particulate matter restrictions. Finally, NOx emissions have brought about the invention of lean NOx traps (LNT) and Urea-SCR. The following sections will discuss these aftertreatment systems in more detail.

2.6.1 Diesel Oxidation Catalyst

A diesel oxidation catalyst is a flow through device containing a honeycomb structure or substrate. The substrate has a large surface area that is coated with a catalytic washcoat, typically platinum or palladium. As the exhaust gas flows over the substrate HC, CO, and some PM are oxidized, thereby reducing harmful pollutants in diesel engine emissions.

The role of the oxidation catalyst is to transform pollutants such as CO, gaseous and liquid HC into CO_2 and water through the process of oxidation. Oxidation is defined as the loss of electrons by a molecule, atom or ion; or simply defined as the increase in oxidation number. Therefore, sufficient oxygen must be present in the exhaust gas to oxidize the HC and CO either by lean combustion or introducing air into the exhaust stream. Approximately 20-30% of total PM mass of diesel exhaust is attributed to saturated hryrocarbons, or soluble organic fraction (SOF) and are the most difficult to

oxidize [18]. Under certain operating conditions, DOC's have been documented to show SOF reduction of 80 – 90%.

Baik [43] studied a 6 cylinder diesel engine with and without a DOC and compared the effect of ULSD and B20 on engine performance and emissions. Overall, the addition of the DOC showed a slight decrease in engine power and increase in fuel consumption for the fuels tested as expected. The B20 blend had a slightly higher reduction in power than the ULSD due to the lower heating values of biodiesel. However, the B20 blend showed an 18% reduction in PM compared to 5% with ULSD. CO and HC decreased 6% - 17% respectively with B20.

2.6.2 The diesel particulate filter

The diesel particulate filter (DPF) is an emission reduction device designed to remove particulate matter (PM) or soot from the exhaust stream of a diesel engine. Particulate matter is the byproduct of incomplete combustion comprised primarily of unburned fuel hydrocarbons; with a smaller contribution being from the lubricating oil [18]. The DPF physically traps, stores and oxidizes the particulate matter generated during combustion that is present in the exhaust, significantly reducing PM emissions emitted into the atmosphere. The physical structure of the DPF is characterized as a wall-flow monolith or a segmented ceramic structure. The two most widely used ceramics are Cordierite and Silicon Carbide. Typically a filter manufactured with Cordierite is done by an extrusion process and is one whole piece, or a monolith. However, filters manufactured with Silicon Carbide are extruded into segments which are then connected together to form the correct filter size. A monolithic Cordierite and a

segmented Silicon Carbide filter are shown below.

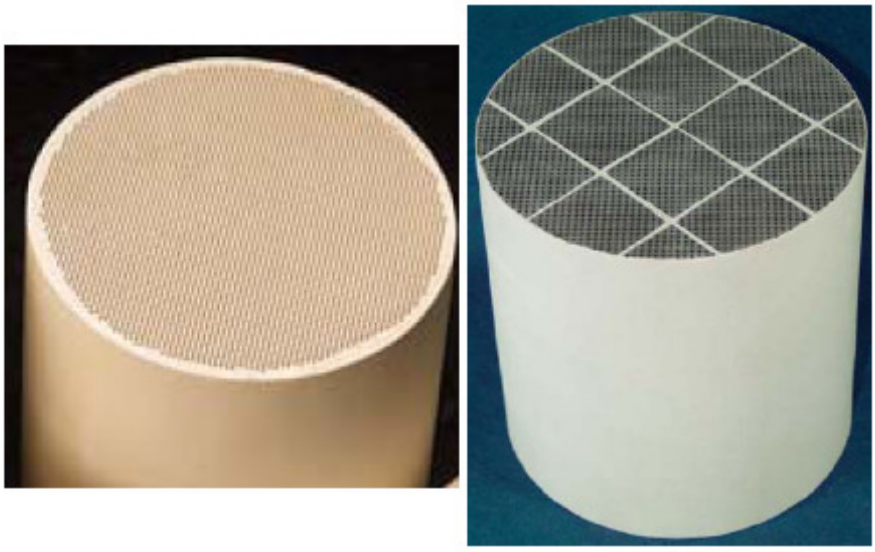

Figure 2.3. Monolith and Segmented Diesel Particulate Filter [44]

The exhaust gas enters the open channel and is forced through the porous walls dividing the channels leaving the soot behind and clean exhaust out. Due to the nature of the DPF, it is essential to have a regeneration technique to burn off the soot and prevent the trap from getting clogged. Although numerous techniques have been proposed, they can be simplified into two main categories; passive and active regeneration.

Regeneration types and strategies

Regeneration is the process of elevating the exhaust temperature flowing through the DPF to burn the soot trapped within the core of the filter. This process restores the DPF allowing exhaust gas to flow through the device and preserving

performance and efficiency of the engine. Regeneration types and strategies depend on the engine use and control capabilities and are defined as passive or active regeneration.

Passive regeneration occurs when engine temperatures elevate from 200℃ to 400℃ due to normal driving conditions to continuously burn off small amounts of trapped soot within the DPF. This type of regeneration is done automatically through the ECU calibration and utilizes a catalyzed DPF to reduce the ignition temperature of the soot.

Active regeneration can occur at idle or during driving conditions to burn off large amounts of soot at one time. A regeneration event typically requires exhaust temperatures of approximately 600℃ to burn off the soot. This type of regeneration is done automatically when the pressure drop, or local exhaust temperature, reaches a predetermined level. The pressure drop steadily increases as the soot accumulates on the filter, reducing the volume of exhaust gas that can flow through the device. Precise control of the pressure drop is required to eliminate excessive fuel penalties and thermal runaway within the DPF [18].

Active regeneration is initiated by the injection of fuel or hydrocarbons into the exhaust stream. This is accomplished by either directly injecting the fuel into the exhaust stream or by adding a post injection scheme to the ECU. The addition of fuel in the exhaust will initiate hydrocarbon combustion when it reacts with the diesel oxidation catalyst, elevating the temperature within the desired range before it enters the DPF.

Williams et al [39] evaluated the effect of biodiesel blends on DPF performance

utilizing a passive regeneration strategy. A 2002 5.9L Cummins engine was equipped with a 12L catalyzed continuously regenerating technology (CCRT) DPF by Johnson Matthey. This system is comprised of a DOC followed by a wall flow through DPF. This passively regenerated system is used in applications with average exhaust temperatures of 200℃-250℃. Overall, results showed that the balance point temperature was 45℃ lower for B20 and 112℃ lower for B100. Regeneration rates between the fuels were also recorded showing a measurable increase in the rate of DPF regeneration at a specific operating point for biodiesel blends over ULSD. PM was also found to oxidize quicker with biodiesel blends than ULSD with blends as little as 5% by volume of biodiesel.

Research conducted at Pennsylvania State University on a Cummins ISB 5.9L direct injection turbo diesel engine investigated the DPF regeneration behavior of biodiesel particulates [35]. They utilized a fixed steady state engine loading condition to load the DPF followed by a two step low and high temperature passive regeneration strategy. In this study, the break even temperature (BET) was determined from the slope of the variation of pressure drop as the temperature is increased similar to other research [39]. Tests were conducted with ULSD, B20 and B100. They found a 30℃ reduction in BET temperature with B100 compared to ULSD. This temperature shift in the BET corresponded to a maximum NO_2 production over the DPF. Therefore the correlation suggests that the internal NO_2 production in the DPF is a mechanism for neat biodiesel to lower the BET temperature.

2.6.3 Urea-Selective Catalytic Reduction

Urea-selective catalytic reduction or Urea-SCR aids in the reduction of nitrogen oxides, or NOx from diesel engine applications. A dosing system injects the diesel exhaust fluid, specifically urea, into the hot exhaust gas stream prior to the catalyst. The spray droplets then undergo hydrolysis and thermoylsis in the catalyst thereby reducing NOx emissions. Fang and Fisher both provided a more detailed explanation of this reaction [45, 46] when urea is used as the reductant. The reduction of NOx from the exhaust is defined by the NOx conversion efficiency, or deNOx efficiency. This process begins after the urea is injected into the hot exhaust stream. The urea decomposes in two steps: Thermolysis of finely sprayed urea into ammonia and isocyanic acid and Hydrolysis of isocyanic acid shown in the following equations respectively.

$$(NH_2)_2CO \rightarrow NH_3 + HNCO \quad (2.4)$$

$$HNCO + H2O \rightarrow NH_3 + CO2 \quad (2.5)$$

These two steps correspond to the overall urea decomposition shown in the following equation.

$$(NH_2)_2CO + H_2O \rightarrow 2NH_3 + CO_2 \quad (2.6)$$

Furthermore, conversion within a SCR catalyst is a function of: temperature, mass flow, NO/NO_2 balance, NH_3 distribution and NOx/NH_3 ratio, as well as the ageing of the catalyst.

2.7 Fuel oil dilution

The constant evolvement of emission requirements in the United States has driven the development and addition of numerous aftertreatment devices for diesel engines as well as an interest in alternative fuels. Each individual aftertreatment device has specific requirements for exhaust components and temperatures required to work efficiently. Meeting these requirements, specifically for an actively regenerated diesel particulate filter (DPF), can lead to fuel dilution of the engine oil.

The dilution of fuel in engine oil is a function of the engine operating strategy and properties of the fuel used. Biodiesel, in particular, is made of fatty methyl esters which are inherent to different physical attributes compared to ULSD: higher surface tension, higher viscosity and lubricity, and lower volatility. The mechanism for oil dilution, regardless of fuel used, is driven by the low volatility components in the fuel. These low volatile components require longer vaporizing after injection which may deposit on the cylinder walls during combustion. As the piston moves down during the power stroke, these deposits can be pushed down into the crankcase. Fuel dilution of motor oil can be detrimental to an engine and its components. Viscosity, in particular, is an important factor in the quality of engine oil. As the viscosity decreases metal to metal contact can occur causing catastrophic failure of bearings and the wearing of the pistons and rings.

Blackburn et al. [47] conducted engine tests on a four cylinder direct injection diesel engine fueled with soybean B100. They found unacceptably high ester contamination of the crankcase lubricant at 0.2% of the fuel flow rate. The gradual contaminant of unburned fuel in the crankcase oil reduced the viscosity followed by an oxidative thickening and subsequent increase in viscosity. Total base number (TBN),

total acid number (TAN), and insolubles remained within satisfactory limits over the length of the experiment. However, evidence was found of copper/lead bearing corrosion following engine inspection.

Andreae et al. [48] measured the fuel dilution and evaporation rates of ULSD and B20 of a six cylinder turbocharged diesel engine. The engine was equipped with a diesel oxidation catalyst (DOC) followed by a DPF. The fuel oil dilution was monitored during regeneration mode utilizing late in-cylinder injection at two different operating points. Results showed that the late injection led to significant fuel dilution, particularly at low speeds and loads. Evaporation of the fuel in the oil was found to be a function of the concentration and operating point showing higher evaporation at increased load and speed. B20 showed higher dilution rates than ULSD, and showed lower rates of evaporation due to higher distillation temperatures of methyl esters as compared to ULSD.

Parks et al. used Laser-induced fluorescence (LIF) spectroscopy to evaluate the oil dilution that can occur when in-cylinder fuel injection strategies for rich operation are used on a Mercedes 1.7L diesel engine [49]. This technique utilizes a florescent dye which is added to the fuel and measured by fiber optic probes located in the engine oil pan. They found, comparing the LIF to the Gas Chromatography (GC) technique, a magnitude of 7 of fuel in oil concentration. This discrepancy is due to the lack of evaporation of the dye used in the LIF technique. Therefore as the fuel evaporates from the engine oil under normal engine conditions, the LIF technique would show a higher value. However, this technique is valuable for rapid feedback and controls development. Overall observations from the experiments found that fuel oil dilution

increases as post injection events are further from TDC. Longer post injection events have also been found to increase the rate of fuel oil dilution.

2.8 Low Temperature Combustion

Conventional diesel combustion is plagued with higher soot and NOx emissions, while producing lower THC and CO emissions. Conventional diesel combustion mixes fuel and air prior to ignition, with ignition of the mixture typically before the fuel is fully mixed. The fuel that is not burned during the premixed combustion burns in the diffusion flame at close to stoichiometric conditions. The high temperatures associated with stoichiometric conditions attributes to the formation of NOx, with soot formed primarily during the diffusion flame burn.

In contrast, operating the engine in the low temperature combustion (LTC) mode provides a promising alternative to CIDI combustion, concurrently reducing soot and the formation of NOx emissions. The LTC strategy used in conjunction with biodiesel fuels will incorporate two relevant topics predominant in research today to meet stringent EPA requirements.

2.8.1 Modulated Kinetics Combustion

The MK concept is a combustion phenomenon developed by researches at Nissan Motor Company [50, 51]. It can be defined as a low temperature, premixed combustion strategy which concurrently reduces PM and NOx emissions. The basic concept of MK combustion developed by Kimura et al can be seen in the schematic of

figure 2.4.

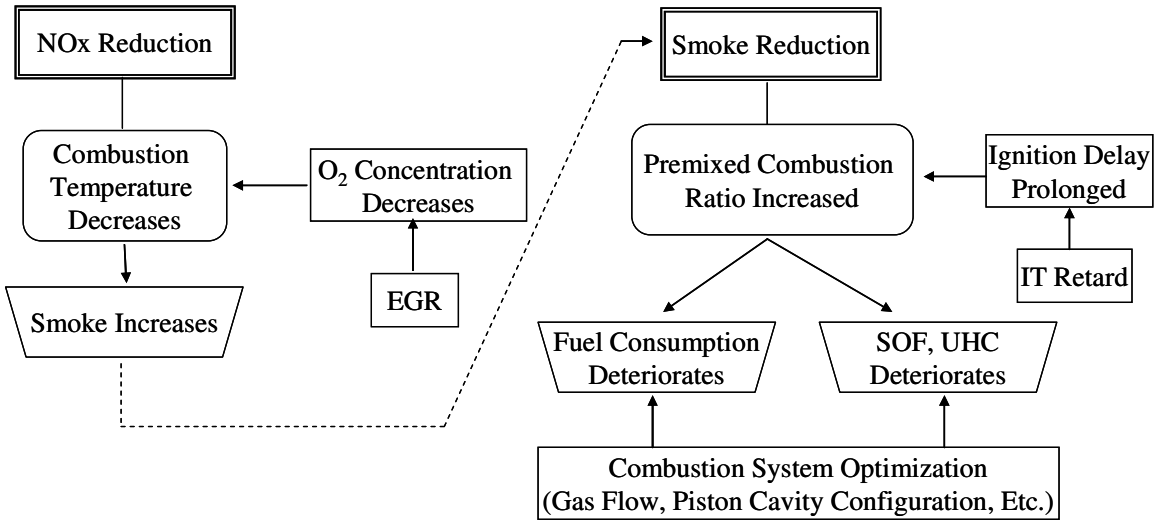

Figure 2.4. Scheme of modulated kinetics combustion [50]

The formation of in-cylinder NOx, discussed earlier in section 2.5.1, is exceptionally sensitive to the combustion temperature. Therefore an effective strategy to reduce NOx formation is to reduce the in-cylinder combustion temperature. The MK concept achieves this by increasing the exhaust gas recirculation (EGR) to deplete the O_2 concentration available for combustion. However, this reduction in O_2 concentration produces a trade off and increases the smoke, or particulate matter. Kimura et al then concluded that the particulate formation could be decreased by operating the engine in a premixed combustion process. Premixed combustion thoroughly mixes the fuel and oxygen before ignition begins. This is done by retarding the timing thereby prolonging the ignition delay to operate in the premixed combustion regime. However, utilizing the MK combustion concept deteriorates fuel consumption, SOF, and UHC. In order to

expand the MK combustion region, optimization of the combustion system is needed. The piston cavity configuration can be expanded to avoid the penalty of increasing UHC due to higher injection pressures which cause the fuel injection spray to hit the cylinder wall. The use of cooled EGR and lower compression ratios can be used to prolong the ignition delay and larger nozzle holes can be used to shorten the injection duration. Finally, increased swirl ratio can be applied to minimize the deteriorating fuel consumption due to retarded injection timing can all be utilized to minimize these tradeoffs.

2.8.2 Smokeless Rich Diesel Combustion

Toyota Motor Company has developed another low temperature combustion technique called smokeless rich diesel combustion [52]. Akihama and coworkers have used a similar approach by using high levels of cooled EGR, in excess of 50%, while advancing injection timing to reduce the flame temperature. The flame temperature is reduced to a level that results in no soot or NOx formation in the cylinder. Furthermore, Akihama found that the quantity of EGR required for low particulate formation decreased slightly as the EGR temperature was lowered from 150℃ to 100℃.

The equivalence ratio and temperature (Φ - T) map is shown in figure 2.5. The Φ - T map was developed from constant volume bomb experiments coupled with KIVA simulation. Three different zones have been labeled in the figure to take advantage of the low soot and NOx operating points: Kamimoto's [53] high temperature combustion method, and two low temperature regions: HCCI and smokeless rich or LTC combustion. Operating the engine in the lower temperature range prevents the

formation of polycyclic aromatic hydrocarbon (PAH) in cylinder from progressing into soot particles.

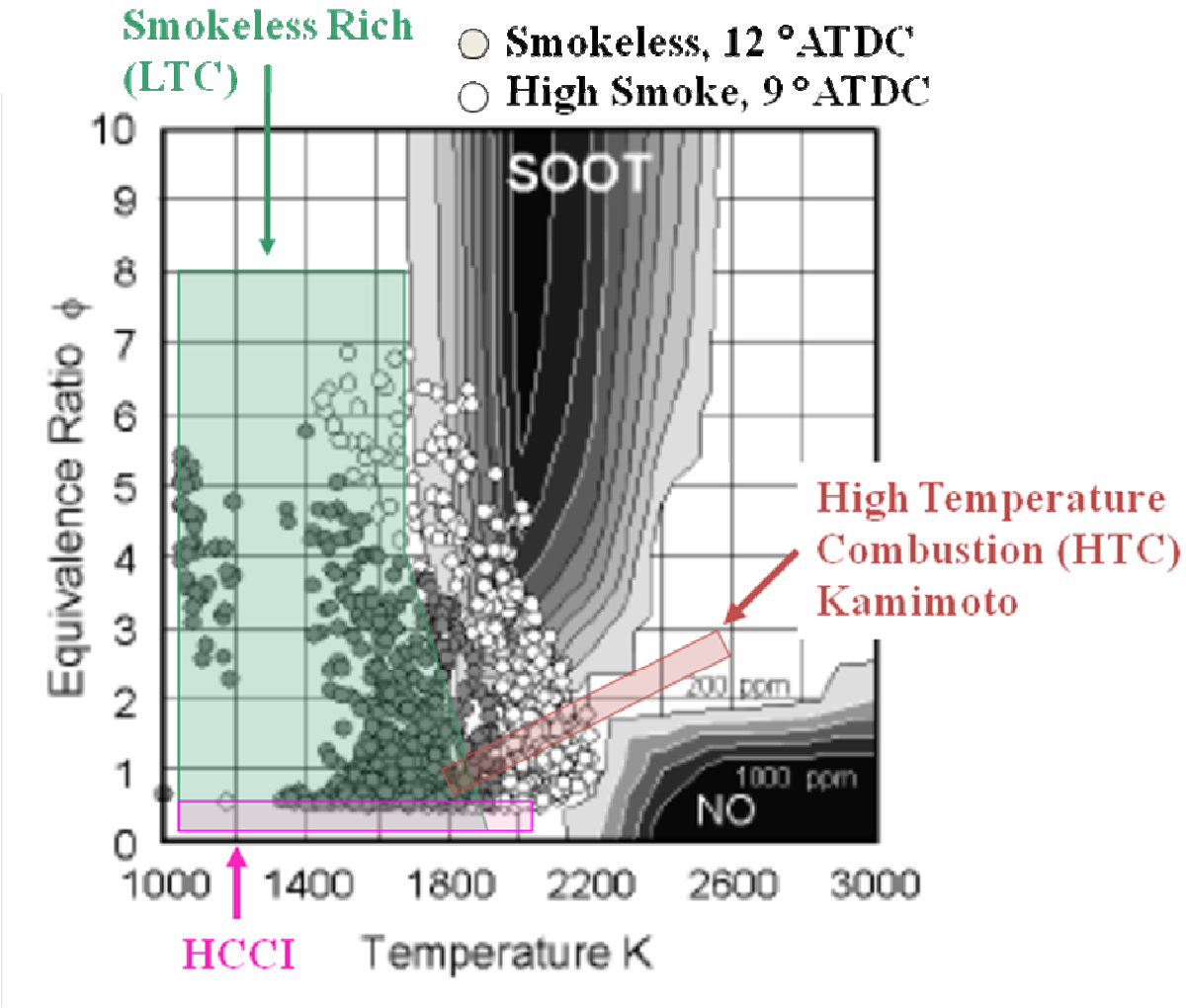

Figure 2.5. Combustion strategies at maximum heat release [52]

2.8.3 Homogeneous Charge Compression Ignition Combustion (HCCI)

Homogeneous charge compression ignition combustion (HCCI) incorporates the principle of premixed combustion to reduce emissions and improve efficiency. HCCI implements the best of both spark ignition (SI) engines and compression ignition (CI) engines to simultaneously reduce both particulate matter and NOx. The HCCI strategy utilizes a premixed homogenous fuel/air mixture which is spontaneously ignited by compression of the piston. The fuel/air mixture is diluted either by utilizing lean combustion with low equivalence ratios, or through the use of high levels of EGR.

In principal, HCCI combustion is an ideal combustion process due to the high thermal efficiencies and extremely low NOx and PM emissions. However, unless the engine geometry or operational conditions are adjusted, the HCCI strategy has a very narrow operating range as seen in figure 2.5. Specifically, the main challenges hindering HCCI implementation in CI engines are:

1. High cylinder pressures and peak pressure rise rates (PPRR) at high loads.
2. Low load combustion efficiency.
3. Difficulty in controlling the autoignition combustion process.

2.8.4 The Influence of Biodiesel on Low Temperature Combustion

Low temperature combustion is an emerging strategy used to attain the simultaneous reduction of soot and NOx formation for diesel fueled engines. In addition, further LTC research is ongoing with respect to the application of biodiesel fuels and the effect these fuels have on LTC combustion. Zheng et.al [54, 55] studied the effect of biodiesel fuel in a 4-cylinder direct injection diesel engine with engine speed at 1500rpm and 8bar IMEP. The amount of EGR applied to the engine was tested from 0% - 70% and the start of injection (SOI) varied with respect to the test group. Overall, they found that biodiesel produced comparable engine out NOx emissions with soot, CO, and UHC emissions lower compared to diesel fueled engine. Furthermore, biodiesel was found to have sustainable combustion for both high EGR rates and retarded SOI. This is explained by the higher cetane number of biodiesel and increased oxygen accessible during combustion.

Fang et.al [56] studied an optical single cylinder direct injected engine for both late and early low temperature combustion strategies for diesel and soy based biodiesel fuel blends. Testing was done at 1500 rpm and 2 bar IMEP using single injection strategies. They found that a longer ignition delay could be seen with increased biodiesel content. This is due to the higher boiling point of the biodiesel fuel. In addition, optimum results were obtained with retarded post-TDC injection timing. This resulted in the simultaneous reduction of soot and NOx with reasonable fuel economy. They concluded that the combination of injection timing optimization with biodiesel fuel blending ratio will optimize the soot/NOx tradeoff for optimum results in diesel engines.

Recent work at the University of Michigan by Northrop et.al [57] studied the effect of late LTC combustion in a multi-cylinder diesel engine operating at 1500rpm, 400 kpa BMEP and EGR percentage at 50%. Injection pressure was varied at 800,1000, and 1200 bar with injection timing at 5,7 and 9 degree BTDC. Testing was done for soy-based biodiesel, B100, B50, B20, and ULSD. They found that NOx emissions were a function of combustion phasing and were found insignificant with respect to the increase in biodiesel blends.

Karra et.al [58] studied the effect of biodiesel fuel (B0, B20, and B100) on low temperature combustion for a medium duty diesel engine. Single and multiple injection strategies were used with engine speed at 1400rpm, EGR at 0% and 30%, and the engine load at 7.11, 6.85, and 5.97 bar BMEP with respect to increasing biodiesel content. They found that the increase in injection pressure resulted in an increase in NOx and a decrease in soot, regardless of the fuel type. This became less significant at higher EGR percentages. The use of double injection strategies were shown to reduce both NOx and soot emissions simultaneously. Furthermore, the increase in NOx emissions during LTC combustion regimes was not affected with B20 blends.

CHAPTER 3

EXPERIMENTAL METHODS AND APPARATUS

The following chapter describes in detail the experimental methods and apparatus used to conduct the study. The first part of the chapter includes a description of the diesel engine setup, data acquisition, and emission measurement system. The remainder of the chapter is devoted to the aftertreatment devices and fuels used during this investigation and their properties.

3.1 The Scope of Experimental Investigation

The following work will examine the fuel effect between biodiesel blends (B20) and ultra-low sulfur diesel fuel. The investigation of aftertreatment devices, specifically a diesel oxidation catalyst coupled with a diesel particulate filter and Urea-SCR will be tested to determine the B20 fuel effect on their performance and effectiveness. Furthermore, low NOx combustion regimes will be studied to understand the difference in operation on combustion and emissions between the two fuels.

3.2 VM 2.8L Engine Setup

Experiments were conducted on a 2005 model year 2.8L VM Motori direct injection, 4 cylinder, common rail, variable geometry turbocharged engine equipped with cooled high pressure EGR. The basic engine specifications are listed in table 3.1. The engine was coupled to a 112kW General Electric DC dynamometer used to load and

motor the engine for steady state testing. The engine test cell is seen in the following figure.

Quantity	**Description**
Manufacturer/Year	VM Motori 2005
Rated Power (KW)	120 @ 3800 rpm
Maximum torque (Nm)	400 @ 1800 rpm
Bore (mm)	94
Stroke (mm)	100
Compression ratio	17.5:1
Inlet Valve Opens (CAD)	15.6° ±2° ATDC
Inlet Valve Close (CAD)	64.4° ±2° ABDC
Exhaust Valve Open (CAD)	66° ±2° BBDC
Exhaust Valve Close (CAD)	32° ±2° ATDC
Firing Order	1-3-4-2
Maximum Common Rail Pressure (Bar)	1350

Table 3.1 Engine Specifications

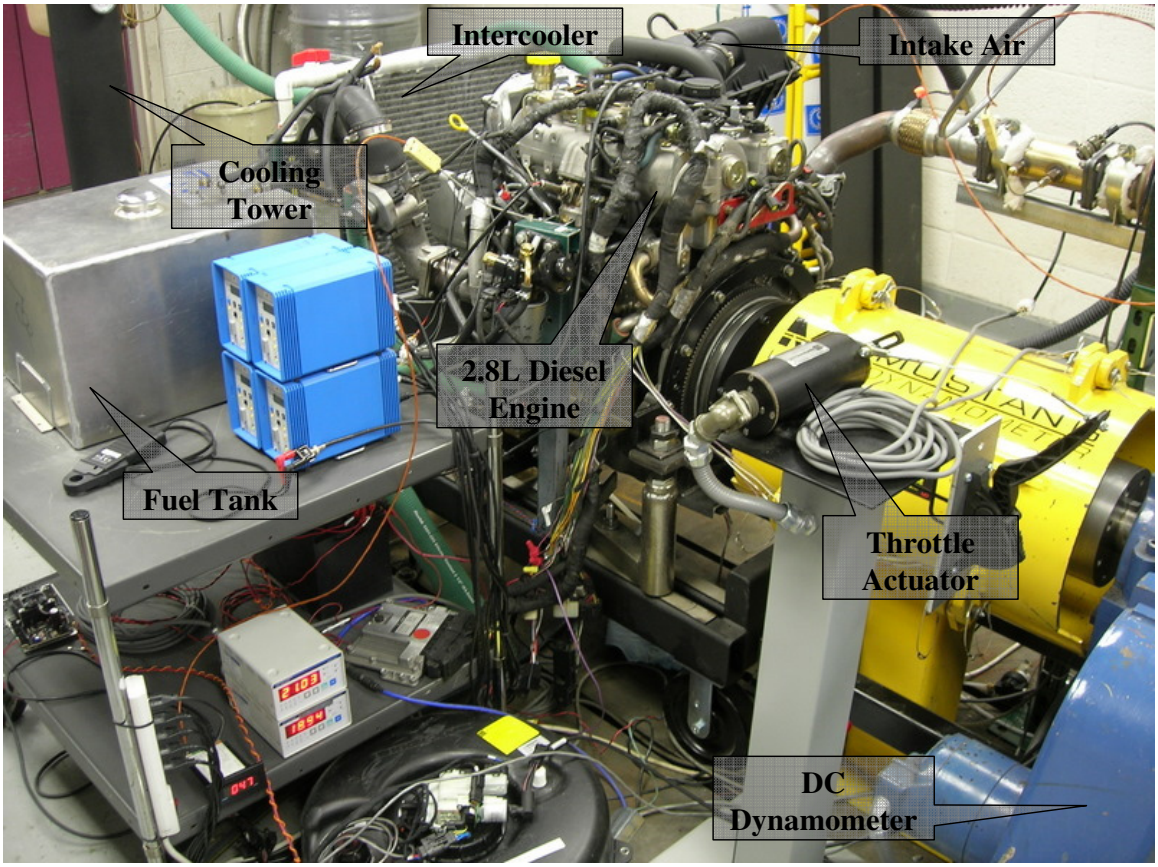

Figure 3.1. 2.8L Diesel Engine Setup

The basic engine remains similar to production, but the open ECU configuration was used to modify calibration of the injection quantities and timing, EGR valve control, etc. utilizing ETAS software INCA v5.4. The engine was further instrumented to measure the following operating parameters.

The instantaneous engine speed is measured using a BEI incremental optical shaft encoder. The encoder is attached at the pulley end of the crankshaft by means of a flexible coupler. The encoder produces 720 pulses per revolution or 1440 pulses per

cycle. The optical encoder consists of a LED light which passes through a disk with patterned lines or slots. The slots in the disk separate the light beam which is then picked up by the photosensor. A square wave signal is produced and inputted into the high speed data acquisition software to record the data in crank angle degrees.

Figure 3.2. BEI optical shaft encoder

The pressure variation in the cylinders is measured by four Kistler piezoelectric transducers mounted in the existing glow plug holes utilizing customized sleeve adaptors. The output of each transducer is directed to a Kistler charge amplifier that converts charge signal into voltage. The charge amplifier scale and sensitivity settings are entered for each calibrated pressure transducer to ensure accurate pressure readings within the cylinders.

High speed data acquisition is done using an engine combustion analyzer provided by Electro-Mechanical Associates. Utilizing the engine cylinder pressure data

and crank angle encoder cylinder to cylinder pressure and combustion differences as well as combustion duration is recorded.

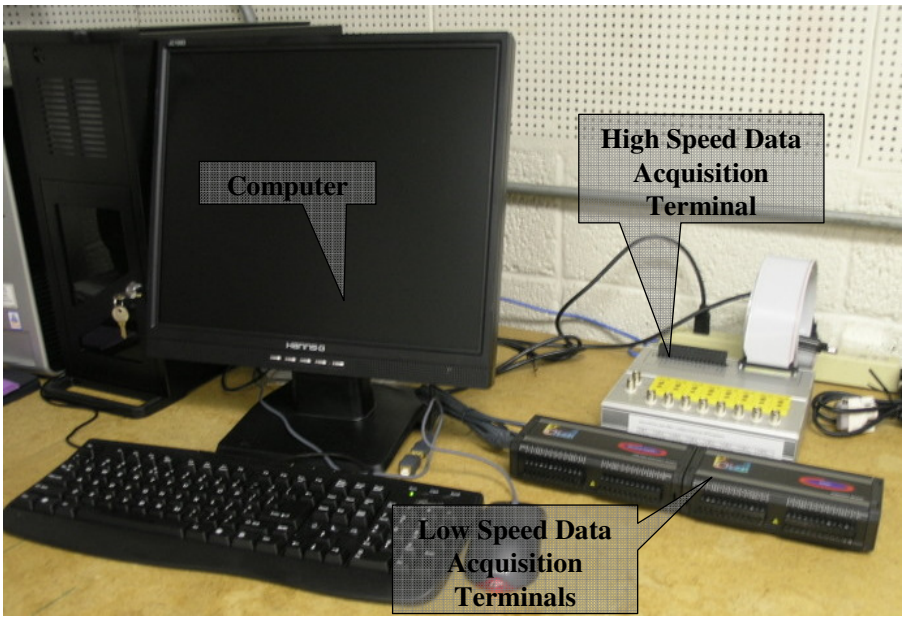

Figure 3.3. High and low speed data acquisition computer from EMA

Due to the scope of the project, the majority of the parameters monitored during testing are measured after the turbocharger. Exhaust emissions are monitored using a Horiba OBS-2200 series capable of on-board vehicle emission measurement system. The system consists of a vibration proof gas analyzers, a laptop PC for control and data logging, and a tail pipe attachment with pitot tube to measure exhaust flow rate. Exhaust species measurement include CO and CO_2 measured by an NDIR analyzer without water extraction, THC concentration using a FID analyzer, and NO and NOx concentrations measured by a CLD analyzer.

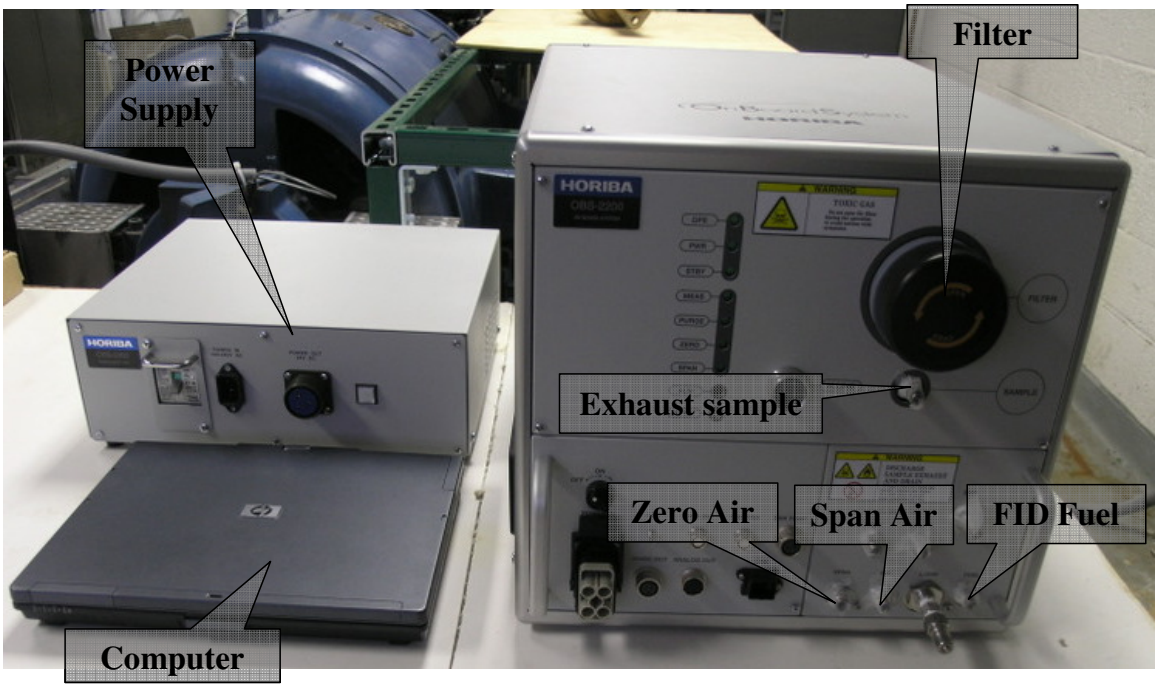

Figure 3.4. Horiba Emissions Bench OBS-2200

The air fuel ratio (A/F), excess air ratio (□), and Oxygen (%O_2) concentrations in the engine exhaust is measured using a Horiba Mexa-700□ analyzer. This instrument is utilized to verify and monitor the percent Oxygen in the exhaust during post injection and maintain high exhaust temperatures for DPF regeneration.

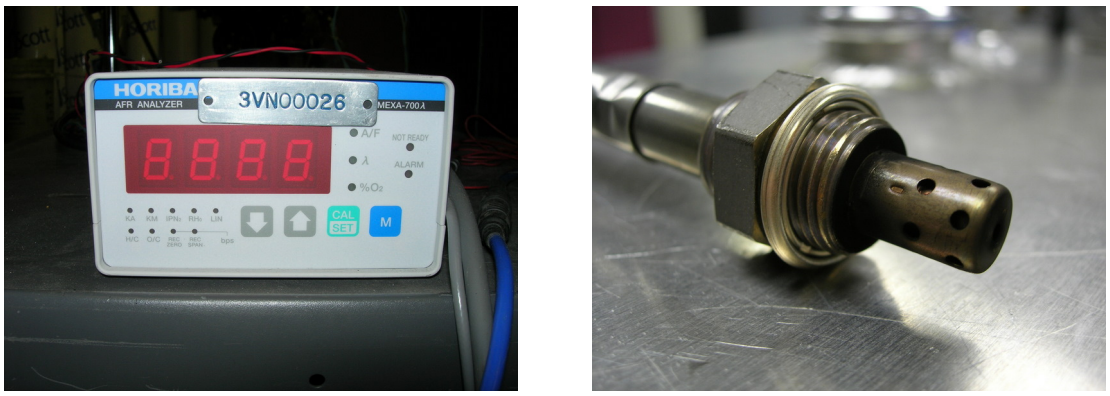

Figure 3.5. Horiba Mexa-700λ display and sensor

Pressure measurements in the proposed aftertreatment configuration are recorded using a MKS Baraton 220 absolute and differential heated pressure transducer capable of measuring from 0-19psi. In the case of the absolute sensor, the reference side is pumped with 1x10-7 Torr and sealed having only one connector on the measurement port. The differential pressure transducer has connectors on both the reference, or low pressure, and the measurement port. The differential pressure transducer is used to measure the pressure drop associated with soot loading of the diesel particulate filter.

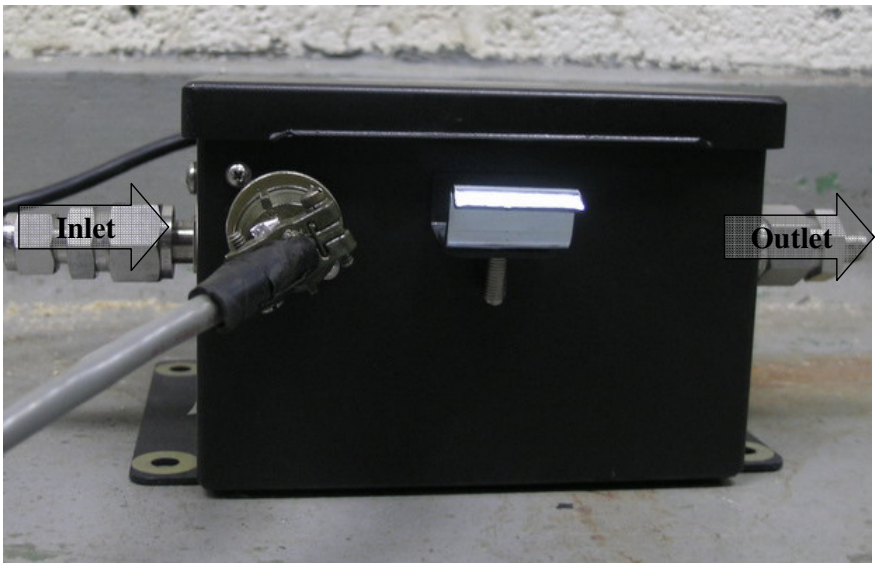

Figure 3.6. MKS heated differential pressure transducer

Exhaust speciation is done using a MKS type 2030 multi-gas analyzer. The multi-gas is a Fourier transform infrared (FTIR) based gas analyzer used to measure multiple exhaust gases. When a gas sample is introduced into the gas cell, the infrared beam is partially absorbed by the gas species present. The resulting spectral

frequencies absorbed and their intensities are due to the atoms associated with the chemical bond and strength of that bond. The absorption spectrum is unique for each infrared-active gas. The multi-gas analyzer measures the absorption spectrum, and its analysis algorithm measures the concentration of each gas using pre-loaded calibrations.

Figure 3.7. MKS Multi-Gas 2030 FTIR exhaust gas analyzer

An AVL 415S smoke meter is used to measure the soot content of the diesel exhaust. The smoke meter is a filter-type that passes a defined flow rate sampled from the engines exhaust and passed through clean filter paper. The blackening of the filter paper is detected by a photoelectric measuring head and the resulting measurement is displayed as the Filter Smoke Number (FSN). The measurement range for the smoke

value is from 0 -10 FSN with a soot concentration of 0 -32000 mg/m^3. The smoke meter has a resolution of 0.001 FSN and 0.01 mg/m^3.

Figure 3.8. Interior of AVL 415S Smoke Meter

3.2.1 Emission Measurement Principle

The measurement of CO and CO_2 utilizes a heated NDIR (non-dispersive infrared) analyzer. Figure 3.9 shows the configuration of the analyzer which consists of a light source, a heated sample cell and a light chopper.

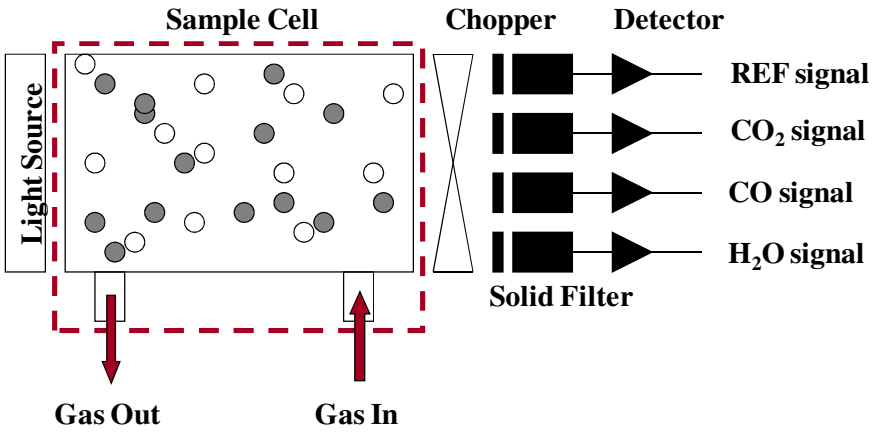

Figure 3.9. Schematic of a Non-dispersive Infrared Analyzer

The analyzer is equipped with optical filters and solid state sensors, specified for CO, CO_2, H_2O, and a reference wavelength. The analyzer works by introducing infrared light passing through the heated sample cell. The light is modulated by the chopper and then reaches the sensors. The optical filters select the wavelength that is characteristic to the sample compounds. During operation when the sample gas in the heated cell contains CO, CO_2, H_2O, infrared radiation is adsorbed by the component of interest in the sample. The quantity of infrared radiation that is adsorbed is proportional to the component concentration. Thereby reducing the light intensity measured by the detector. The decrease in light intensity is a direct relation to the concentration of CO and CO_2 in the sample gas and is calculated using the output of each sensor. H_2O concentration is monitored as to compensate the H_2O interference on the other two components. The sample gas is heated up to 120C so that wet sample gases can be measured without water extraction.

The measurement of total hydrocarbon (THC) is done using a flame ionization detector (FID). Hydrogen flame ionization uses the detection of ions generated by the heat energy when hydrocarbons are introduced into a hydrogen flame. Hydrogen and air are supplied to a burner and a hydrogen flame is formed. A DC voltage is applied to electrodes located on either side of the flame. The sample gas mixed with the fuel H_2 is exposed to the hydrogen flame generating ions. The ions migrate towards the electrode and are detected as current. The current signal corresponds approximately in proportion of reduced carbon atoms in the flame.

The measurement for NOx is done by using a chemi-luminescence detector (CLD). Sample gas with nitric oxide is combined with ozone gas (O_3) in a reactor to form NO_2 in an excited or activated state. The activated NO_2 release light visible to infrared light as it returns to the ground state. The degree of light is directly proportional to the number of NO molecules before the reaction. Thus, the NO concentration in the sample can be acquired by measuring the amount of light emission. To determine the amount of NO_2 in a sample, it must first be converted to nitric oxide (NO) because NO_2 is not chemiluminescent.

3.3 Development of Post Injection

Regeneration is the process of elevating the exhaust temperature flowing through the cDPF to burn the soot trapped within the core of the filter. This process restores the cDPF allowing the exhaust gas to flow through the device and preserving performance and efficiency of the engine. Regeneration types and strategies vary depending on the engine used and control capabilities. For this work an active

regeneration scheme is utilized by the initiation of an added in-cylinder post injection late in the cycle to the ECU calibration. The late post injection provides the hydrocarbons needed to initiate hydrocarbon combustion when it reacts with the diesel oxidation catalyst. The heat generated increases the temperature within the desired range before it enters the cDPF.

Before any work could be done to regenerate the cDPF, extensive knowledge of the exothermic reaction occurring in the DOC needed to be determined for each of the fuels used. Post injection quantities, EGR values, as well as speed and load were modified to carefully control the temperature before it entered the cDPF. Strategies were developed to produce repeatable temperatures before the cDPF so that the fuel effect could be determined for the regeneration rate and the temperature at which regeneration begins.

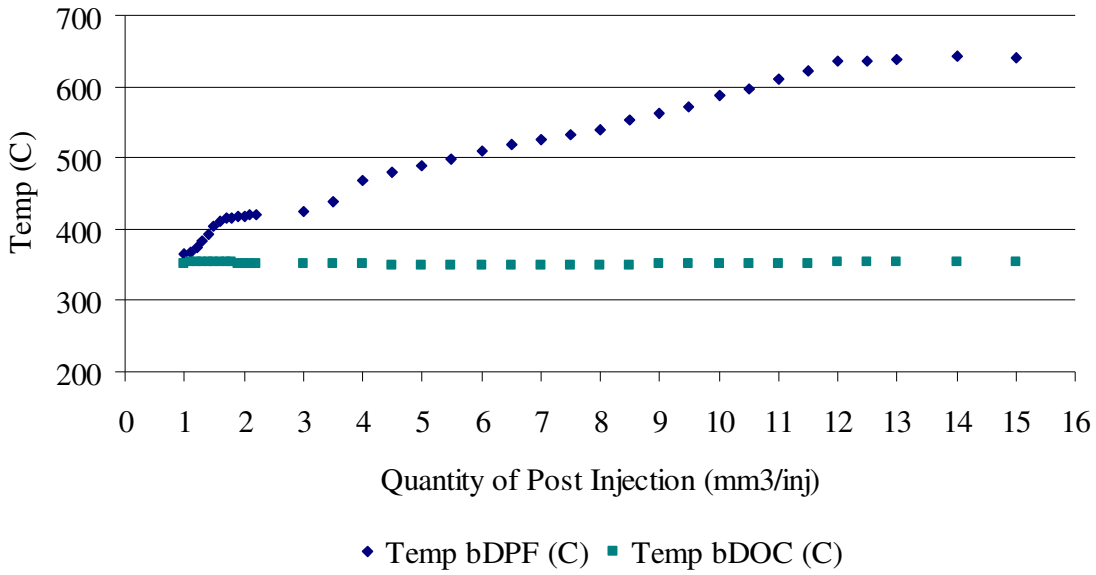

Figure 3.10. Exhaust temperature before and after the DOC during post injection

The temperature difference across the DOC is at a maximum of 250℃ which can be seen in the figure. Exceeding temperatures of 250℃ may result in catalyst degradation and premature failure of the DOC. This procedure was duplicated for B20 fuels.

3.4 Heat Release Data

The fundamentals of conventional diesel combustion heat release plots must be explained in order to compare different combustion modes. The following figure shows the average pressure trace of all four cylinders measured with the Kistler in-cylinder pressure transducers. The figure depicts the engine motoring and firing at a steady state condition 4 bar BMEP, 1200 rpm, and a dual-pilot+main injection strategy.

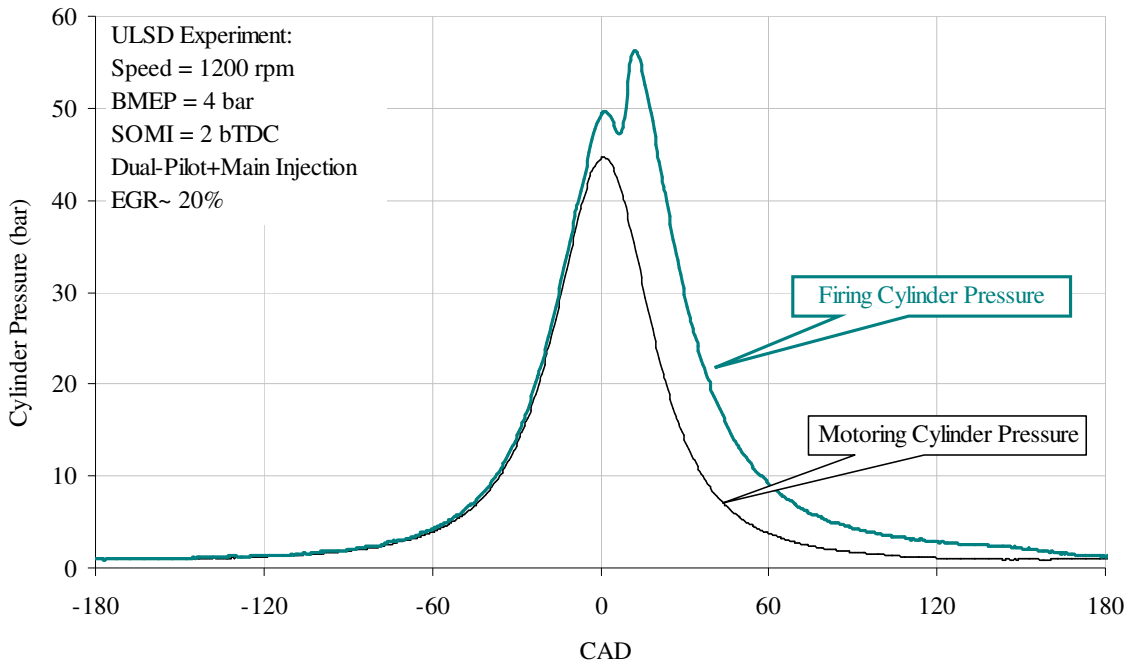

Figure 3.11. Example of pressure trace

The following figure shows the Apparent Heat Release Rate (AHRR) plot for the VM Motori engine calculated using the measured cylinder pressure.

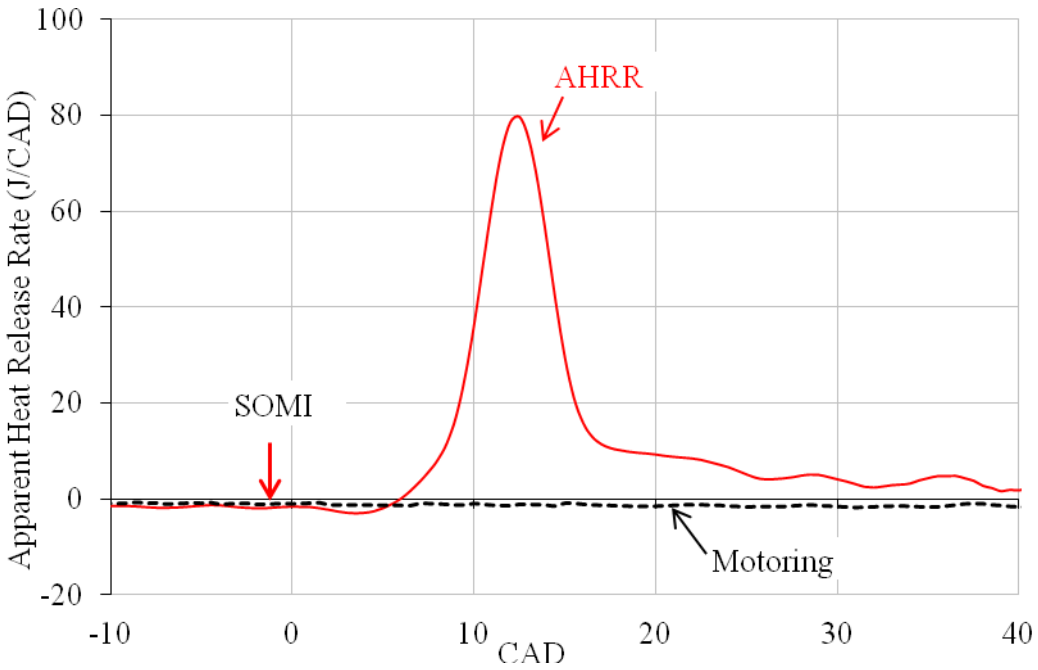

Figure 3.12. Example of Heat Release

The graph depicts the engine calibration of a single main injection (SOMI = 2 bTDC). The red line indicates the heat release while the black line represents the motoring engine condition. After the injection of the fuel, the heat release rate becomes negative due to the fuel evaporation and heat transfer from the cylinder gas to the cylinder walls. The heat release rate will continue to be negative until the exothermic reactions produce more energy than lost in the evaporation of the fuel. This is followed by the premixed combustion regime which is defined at the point the AHRR reaches the motoring curve until the peak of the heat release curve. This represents the lighter components of the fuel burning followed by the heavier components of the fuel burning as the AHRR begins

to decrease. The remaining regime represents the heat release due to the diffusion combustion of the fuel.

The following figure depicts the engine calibration with a dual-pilot injection followed by a main injection. The above description of the AHRR plot is the same with the addition of the small bump in the heat release curve after the two pilot injections. This represents the cool flame regime and completion of the exothermic reactions from the small pilot injections. The main injection follows which leads to the premixed combustion followed by the diffusion combustion.

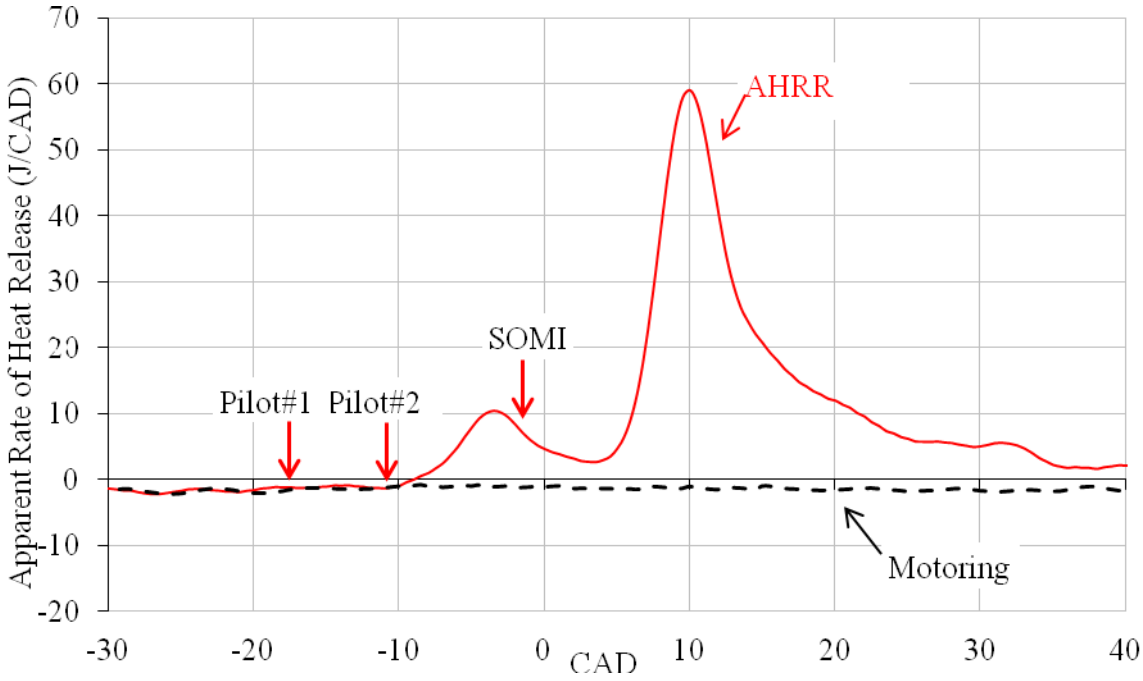

Figure 3.13. Example of Heat Release with Dual-Pilot and Main Injection

3.5 Diesel Oxidation Catalyst

The diesel oxidation catalyst (DOC) used for the following study is provided by Delphi Corporation. The DOC and a picture of the inside catalyst is shown in the following figures. The DOC has a platinum wash coat and has a length of 3 and a diameter of 4.6 inches. The catalyst has a cell density of 400 cells/in^2.

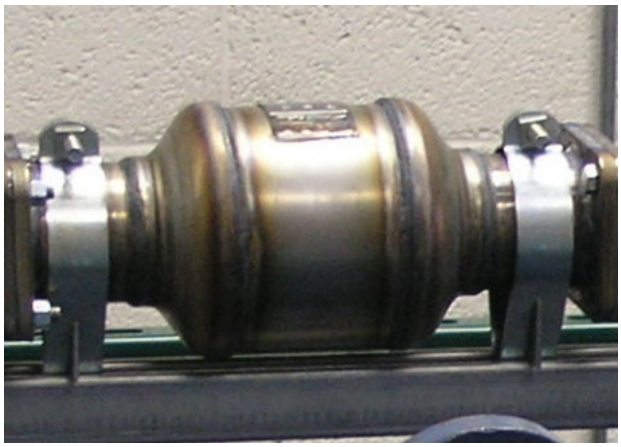

Figure 3.14. Diesel oxidation catalyst and inside catalyst

3.6 Catalyzed Diesel Particulate Filter

The catalyzed diesel particulate filter (cDPF) used for the following study is provided by Delphi Corporation. The DPF is a catalyzed silicon carbide (SiC) wall flow type diesel particulate filter. The filter is sized at four liters with a diameter of 5.66 inches and length of 10 inches. The cDPF has a cell density of 200 cells/in^2.

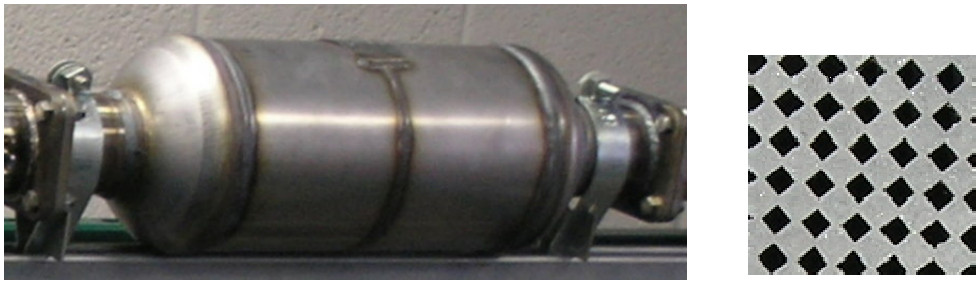

Figure 3.15. Diesel particulate filter and inside catalyst

3.7 Urea-Selective Catalytic Reduction

The urea-selective catalytic reductant (Urea-SCR) system used in the following study is provided by both Delphi and Bosch. The catalyst, provided by Delphi, is a Cu-zeolite based catalyst which is 5.66 inches long has an O.D of 12 inches with a cell density of 400 cpsi. The experimental setup examines two types of entrance lengths, long and short, and is shown in the following figure.

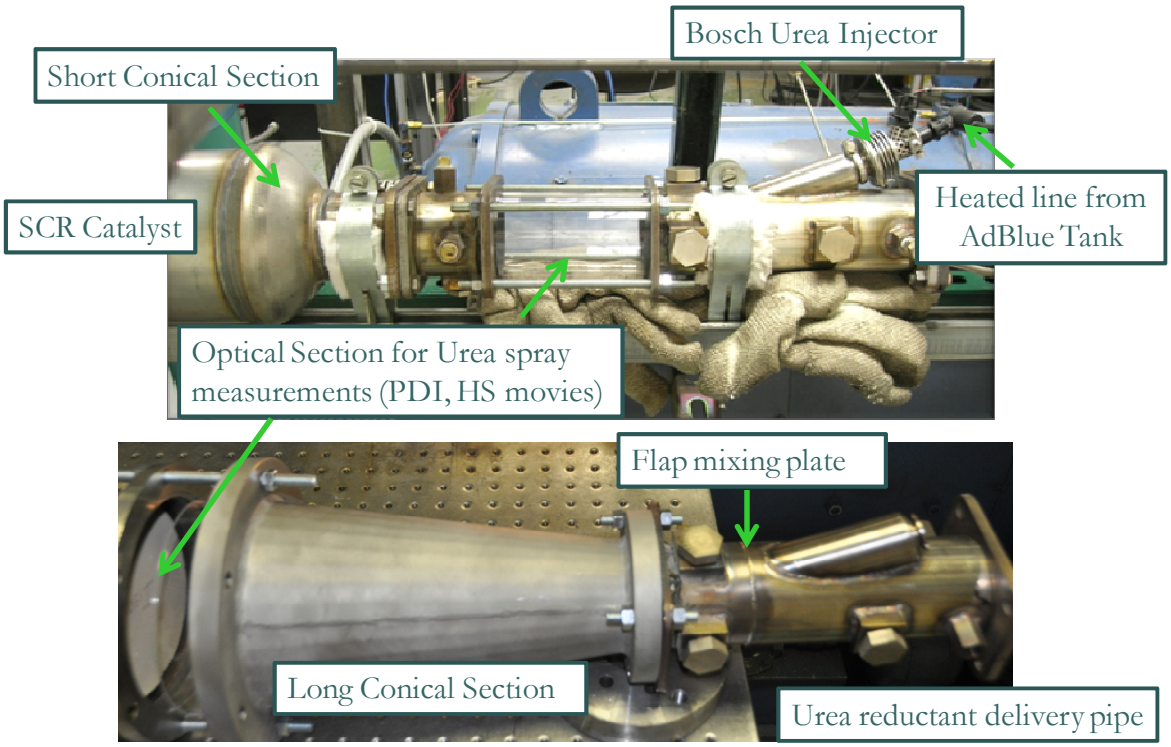

Figure 3.16. Urea-SCR setup for long and short conical sections

The Urea dosing system is provided by Bosch and contains an injector placed after the cDPF followed by a flap mixer to mix the urea before entrance into the SCR catalyst. The flap mixer and injector are shown in figure 3.17.

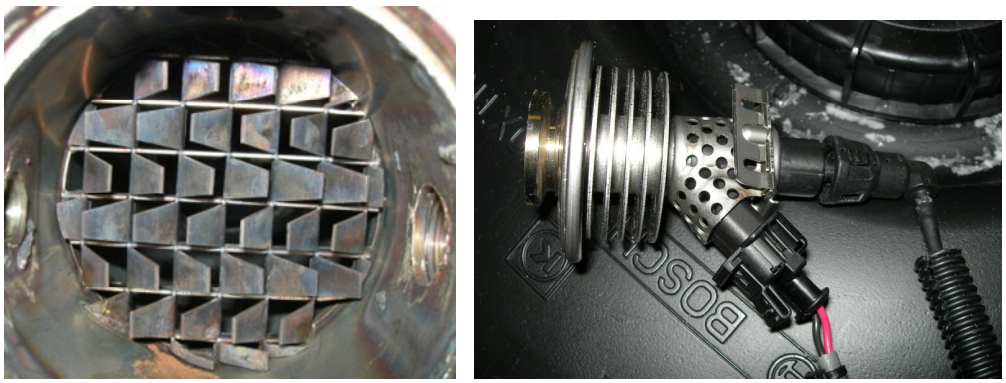

Figure 3.17. Flap Mixer and Urea injector

The injector has a three hole spray pattern and is fixed at a 30 degree angle on the exhaust pipe wall before the mixer. Detailed experimental data is shown by Lee et.al [59].

3.8 Fuel Specifications

The biodiesel fuel used in this study was provided by NextDiesel in Adrian, MI with all analysis provided by NextEnergy in Detroit, MI. Ultra low sulfur 2007 certification diesel was supplied by Haltermann.

FA	Choice White Grease (wt%)
C14:0	1.86
C16:0	22.56
C16:1	2.97
C18:0	12.82
C18:1	41.23
C18:2	16.91
C18:3	1.65
C20:0	0

Table 3.2. Choice white grease biodiesel composition provided by NBEL at NextEnergy

Property	ASTM	Limits	NextDiesel
Calcium & Magnesium	EN 14538	5ppm Max	< 1 ppm
Flash Point (closed cup)	D93	93C Min	164C
Alcohol Control			
Methanol Content	EN14110	0.2% Max	0
Flash Point	D93	130C Min	164C
Water & Sediment	D2709	0.05% Max	0.035%
Kinematic Viscosity, 40C	D445	1.9-6.0 mm2/sec	4.7
Sulfated Ash	D874	0.02% Max	<0.001
Sulfur			
S15 Grade	D5453	0.0015% mass Max	0.0011
S500 Grade	D5453	0.05% mass Max	
Copper Strip Corrosion	D130	No. 3 Max	1a
Cetane Number	D613	47 Min	58.4
Cloud Point	D2500	Degrees C	9 C
Carbon Residue – 100%	D4530	0.05% Max	<0.05
Acid Number	D664	0.50 mg KOH/g Max	0.42 mg KOH/g
Free Glycerin	D6584	0.020% Max	0.005
Total Glycerin	D6584	0.240 % Max	0.134
Phosphorus Content	D4951	0.001% Max	0.0001
Distillation, T90 AET	D1160	360C Max	344
Sodium & Potassium	EN14538	5 ppm Max	5.0 ppm
Oxidation Stability	EN14112	3 hrs Min	3.01 hr

Table 3.3. Lab analysis results provided by Nest Diesel (5/20/2008)

CHAPTER 4

DATA ACQUISITION AND ANALYSIS OF AFTERTREATMENT SYSTEMS

The following chapter describes the aftertreatment configuration used as well as the testing procedure followed. The effect of loading and regenerating a catalyzed diesel particulate filter is explored with further analysis of the possibility of fuel oil dilution that occurs during post injection regeneration events.

4.1 Diesel Oxidation Catalyst and Diesel Particulate Filter

The aftertreatment configuration tested consists of a diesel oxidation catalyst (DOC) followed by a catalyzed diesel particulate filter (cDPF). The objective of this portion of the study was to look at the effect biodiesel fuel will have on the loading and regeneration rate as well as the speciation of exhaust emissions. Further analysis is done to evaluate the effect of post injection on fuel oil dilution for B20 and ULSD.

4.1.1 The Experimental Configuration

A platinum coated DOC, 4.6 inches OD and 3 inches in length, and 400 cells/in^2 cell density is provided by Delphi Corporation. The DOC is located 18 inches from the turbo exit and followed by the cDPF. The DPF is a catalyzed silicon carbide (SiC) wall flow type diesel particulate filter. The filter is sized at four liters with dimensions of 5.66 inches in diameter and 10 inches long in length with a cell density of 200 cells/in^2 and is also provided by Delphi Corporation. A schematic in figure 4.1 is shown to indicate the aftertreatment configuration and location of sensors.

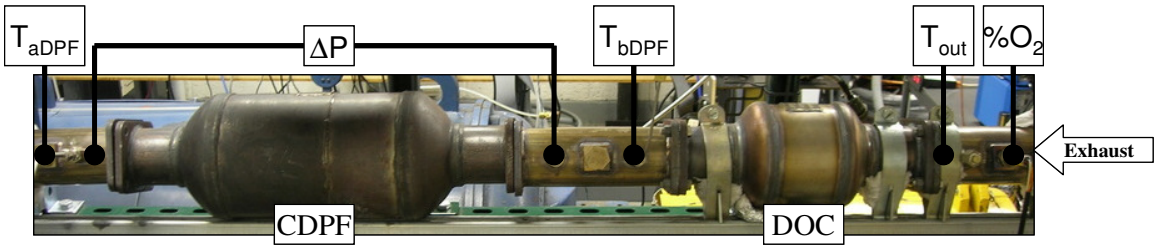

Figure 4.1 Aftertreatment Schematic

K-type thermocouples measure the temperature at four locations: after the turbo, before the DOC, after the DOC and after the cDPF. A MKS heated pressure transducers records the pressure before the DOC and across the cDPF to monitor soot loading and the regeneration rate. A backpressure valve is used to maintain a similar load point and constant EGR flow at the different operating speeds/test points. The oxygen concentration at the cDPF outlet was analyzed by an A/F meter (Horiba, MEXA 110). Exhaust emissions were recorded using the Horiba OBS-2200 system and speciation is done using a MKS 2030 Multi-Gas analyzer.

4.1.2 Diesel Particulate filter loading

As seen from the particulate matter studies of different engine injection strategies and fuel effects, loading time will vary between ULSD and B20 due to lower PM values for B20. Loading curves were developed to determine the time required to load the DPF with 5g/L of soot. Prior to the loading curve study, the initial clean hot cDPF weight is determined. The engine is run at a high speed and load utilizing the

post injection strategy to elevate the temperature of the cDPF to 650C. This temperature is held for 30 minutes to burn off any remaining binders on the catalyst. The initial base weight of the cDPF is 8251.2 ±0.3 grams. This initial clean weight was achieved after each regeneration event.

The level of particulate loading of the filter will affect filter performance, therefore individual loading curves for each of the fuels used is developed. Experiments are conducted to understand how to repeatedly load the cDPF with the same amount of particulate, and how to quantify that amount. In all experiments the 4L cDPF is loaded to approximately 5g/L or 60% of typical engine use loading levels. However, different fuels require different loading times to accumulate the same loading level. Therefore the following loading curve procedure is used to determine the time required to repeatedly load the cDPF with 20gm of soot.

The cDPF starts out clean and the initial cold weight is recorded. The engine is warmed up at 1200rpm and 20% load until the engine coolant temperature stabilizes at 80℃. The engine is then brought up to the speed and load of the first test point. When the exhaust temperature has stabilized for five minutes the hot cDPF is weighed again. All temperatures, pressures, speed and load, as well as emissions is recorded at this point. This determines the zero point of the loading curve and sub sequential data from this initial point will develop the loading curve at test point #1. The cDPF is weighed as a function of time until the soot loading is met, approximately 60% of the maximum recommended loading, thereby developing a soot loading curve at that specific test point and fuel. It is important to note that the weighing procedure of the cDPF during soot loading is essential in establishing repeatability from test to test. Williams et al.

reported significant differences in weight with respect to weighing procedures. They found that the most robust procedure was to quickly remove the cDPF while hot and quickly record the weight, as the DPF starts to immediately gain moisture weight as the temperature begins to cool [39]. Care was taken to measure the DPF at approximately 400℃ each time to eliminate any additional water gain.

The loading curve is shown in figure 4.2 for both B20 and ULSD as a function of time. The soot loading time with B20 gives a 26% increase in time compared to ULSD. This is a benefit to using B20 over ULSD because of longer loading time and decreased number of regeneration events extending cDPF life and efficiency.

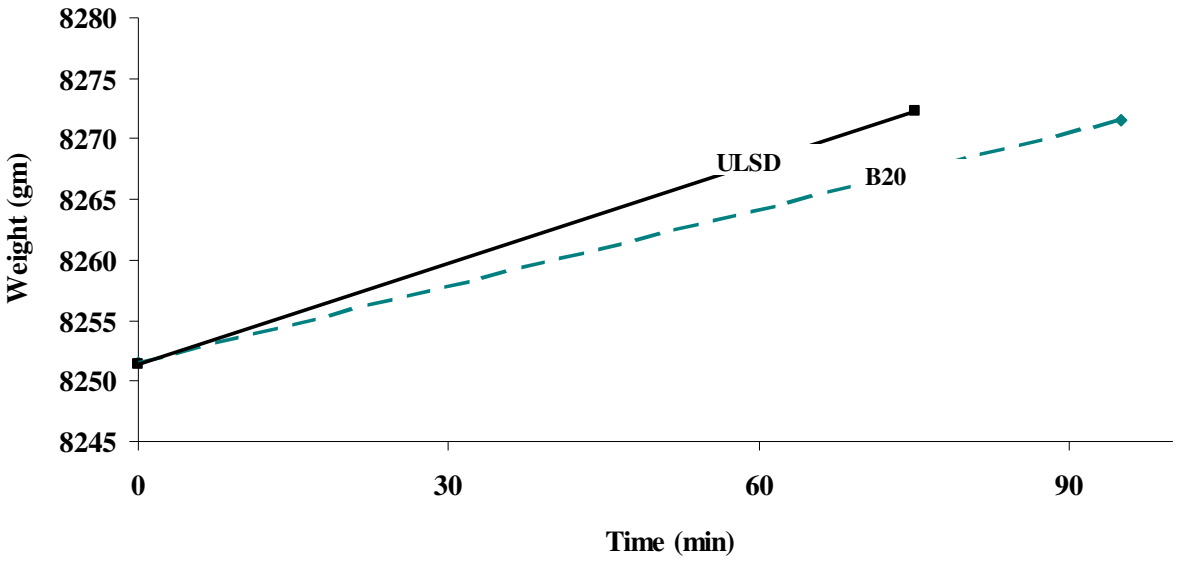

Figure 4.2. Soot loading curve of the cDPF for B20 and ULSD fuels.

Figure 4.3 below shows the repeatability of the cDPF loading point. Subsequent soot loading obtained accuracies of ±3 grams of soot. However, after multiple loadings

of the cDPF, a drop in soot accumulation was noted during the ULSD loading of the cDPF. Figure 4.4 shows a picture of the inlet of the DOC after the cDPF was loaded. Significant blockage and soot accumulation was found on the front of the DOC. This accumulation on the DOC was accredited to the loss of overall cDPF weight saw in loading of ULSD for the second time.

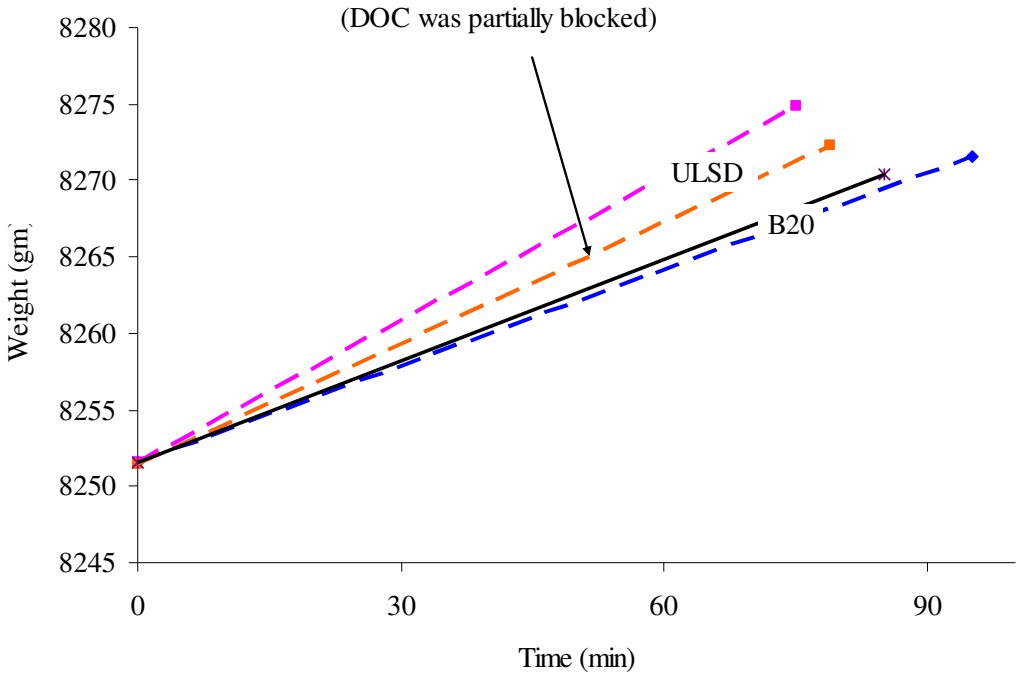

Figure 4.3. Repeatability of cDPF loading

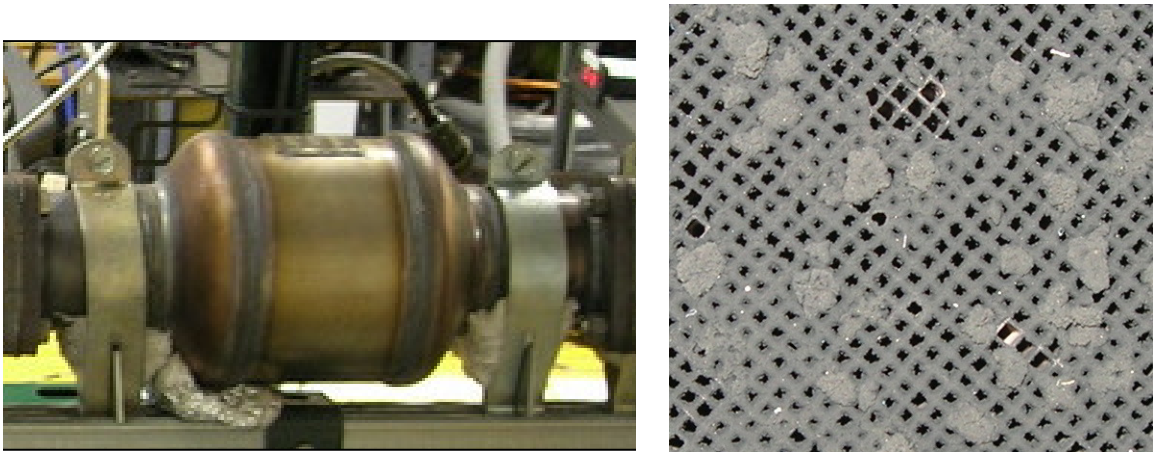

Figure 4.4. Picture of the inlet of the DOC after loading the cDPF

4.1.3 Regeneration Strategy

Regeneration is the process of elevating the exhaust temperature flowing through the cDPF to burn the soot trapped within the core of the filter. This process restores the cDPF allowing the exhaust gas to flow through the device and preserving performance and efficiency of the engine. Regeneration types and strategies vary depending on the engine used and control capabilities. For this work an active regeneration scheme is utilized by the initiation of an added in-cylinder post injection late in the cycle to the ECU calibration. The late post injection provides the hydrocarbons needed to initiate hydrocarbon combustion when it reacts with the diesel oxidation catalyst. The heat generated increases the temperature within the desired range before it enters the cDPF.

Before any work could be done to regenerate the cDPF, extensive knowledge of the exothermic reaction occurring in the DOC needed to be determined for each of the

fuels used. Post injection quantities, EGR values, as well as speed and load were modified to carefully control the temperature before it entered the cDPF. Strategies were developed to produce repeatable temperatures before the cDPF so that the fuel effect could be determined for the regeneration rate and the temperature at which regeneration begins.

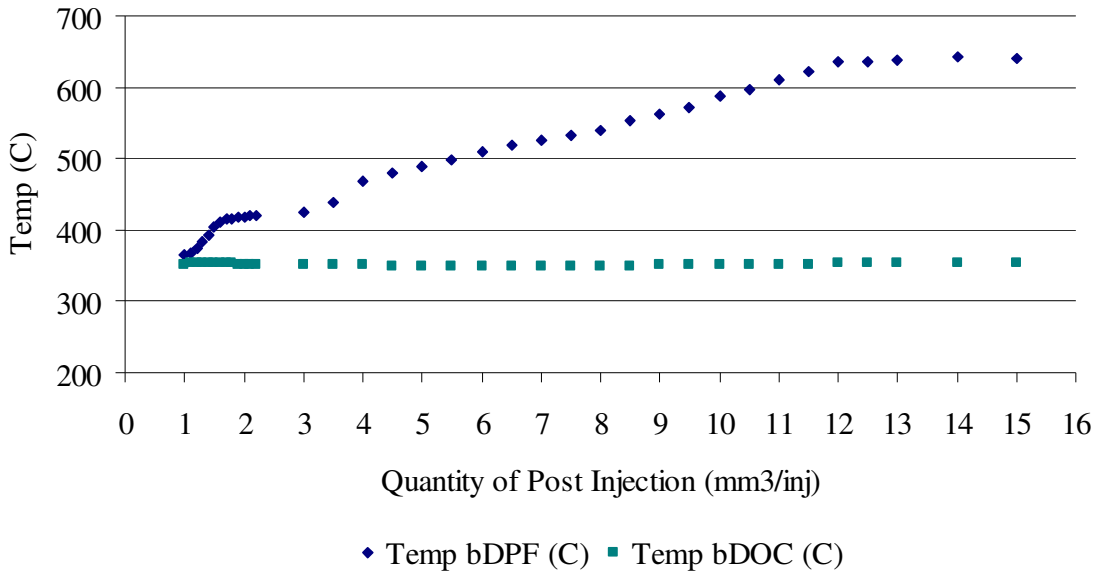

Figure 4.5. Exhaust temperature before and after the DOC during post injection

The temperature difference across the DOC is at a maximum of 250℃ which can be seen in the figure. Exceeding temperatures of 250℃ may result in catalyst degradation and premature aging of the DOC.

4.1.4 Determination of the brake-even temperature

The brake even temperature is defined as the cDPF inlet temperature at which the rate of soot particle oxidation approximately equals the soot particle collection. Therefore, the cDPF should not experience a net gain or loss of particulate matter and the differential pressure should remain constant. This temperature is of interest because soot loaded using different fuels would have different brake-even temperatures and would thereby start regeneration at a lower temperature. Brake-even temperature tests were conducted to compare the operation of a cDPF on 2007 certification diesel fuel and a B20 blend. The brake-even temperature was determined using the following test.

The cDPF was completely regenerated to its base weight of 8251.3 ±0.3 grams. The cDPF was then preloaded with 5 gram/liter of soot with the engine running at a steady state condition. An active regeneration strategy is employed to increase the temperature of the exhaust stream and determine the lowest ignition temperature of the soot when loaded using ULSD. The same testing procedure is repeated for B20. The engine is maintained at a low speed and load with the post injection quantity at $2mm^3$/cyc. The post injection quantity is gradually increased as the temperature of the cDPF reaches steady state condition. This sequence is repeated until the pressure drop across the cDPF begins to decrease, indicating the start of regeneration. Figure 4.6 shows the variation of temperature in the start of regeneration which shows the dependence upon the test fuel used. The temperature at which the slope changes from a positive to a negative value indicates the temperature at which the soot ignites and the start of the cDPF regeneration is defined. This test was repeated twice for B20 and

ULSD. The break-even temperature for B20 is found to be about 63°C lower than soot loaded with ULSD which began to regenerate at about 559°C.

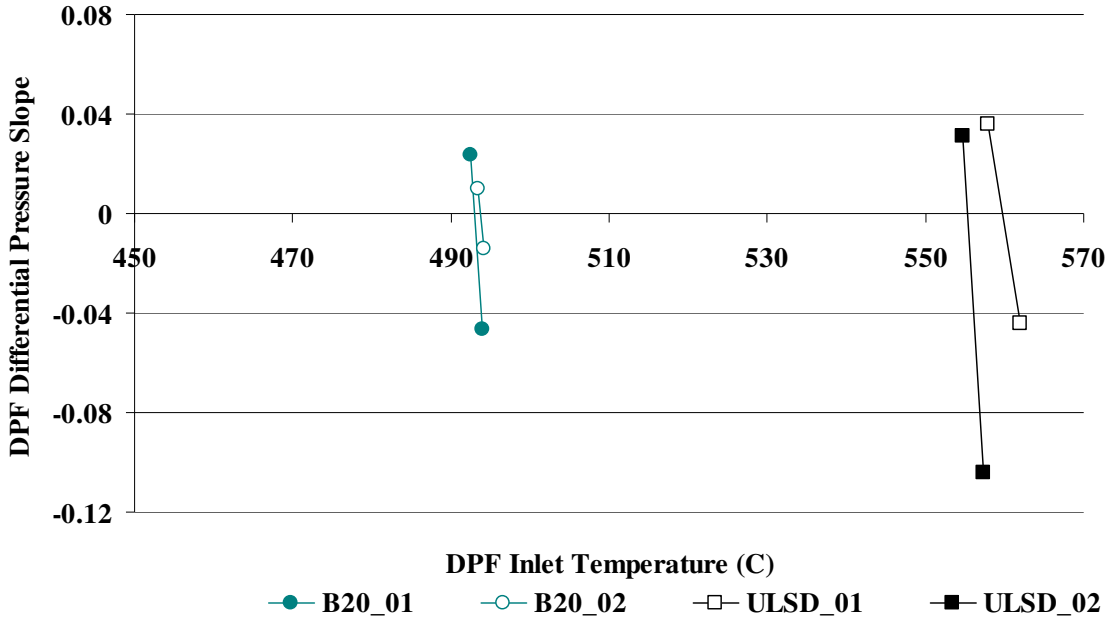

Figure 4.6. Evaluation of the brake-even temperature for B20 and ULSD

The following figures show the outlet of the cDPF when fully loaded with soot and after the regeneration event. It is clear that the cDPF returns to its original state prior to soot loading.

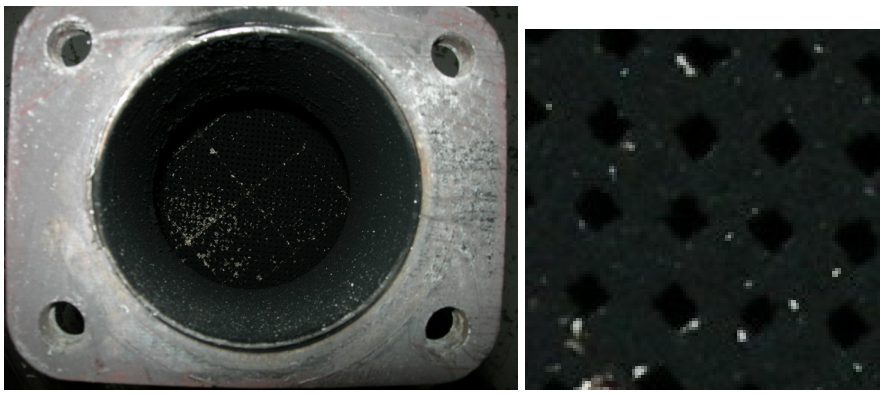

Figure 4.7. Outlet of the catalyzed DPF when loaded with soot

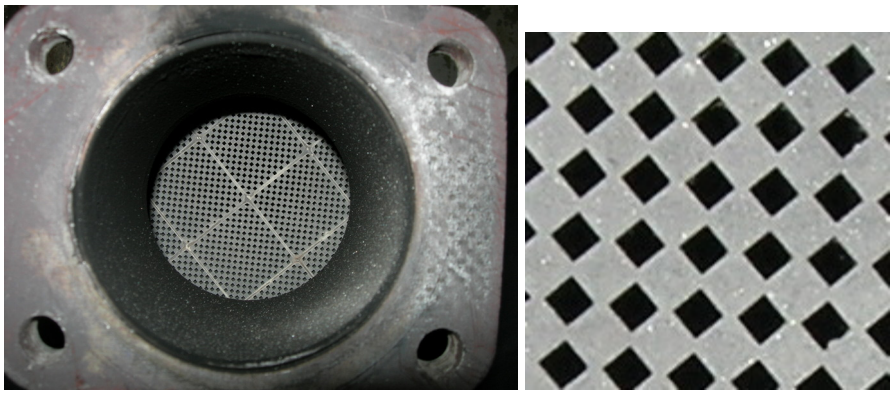

Figure 4.8. Outlet of the catalyzed DPF after regeneration event

4.1.5 Effect of fuel on regeneration rate

To further understand the effect of B20 on the performance of the aftertreatment systems, the rate at which regeneration occurs is analyzed. The same engine setup is used with a DOC followed by a catalyzed DPF. The cDPF is fully regenerated to its base weight and preloaded to 5 grams/liter at a medium load and speed to simulate

25% recommended cDPF loading and regeneration conditions similar to the brake-even temperature testing. However, instead of stepping through the post injection strategy, the injection is set to 10mm^3/cyc to maintain a temperature of 600°C. The temperature is held constant for both B20 and ULSD to eliminate any temperature effect and to evaluate the difference of regeneration rate behavior between the two fuels. Figure 4.9 shows the regeneration rate results for B20 and ULSD.

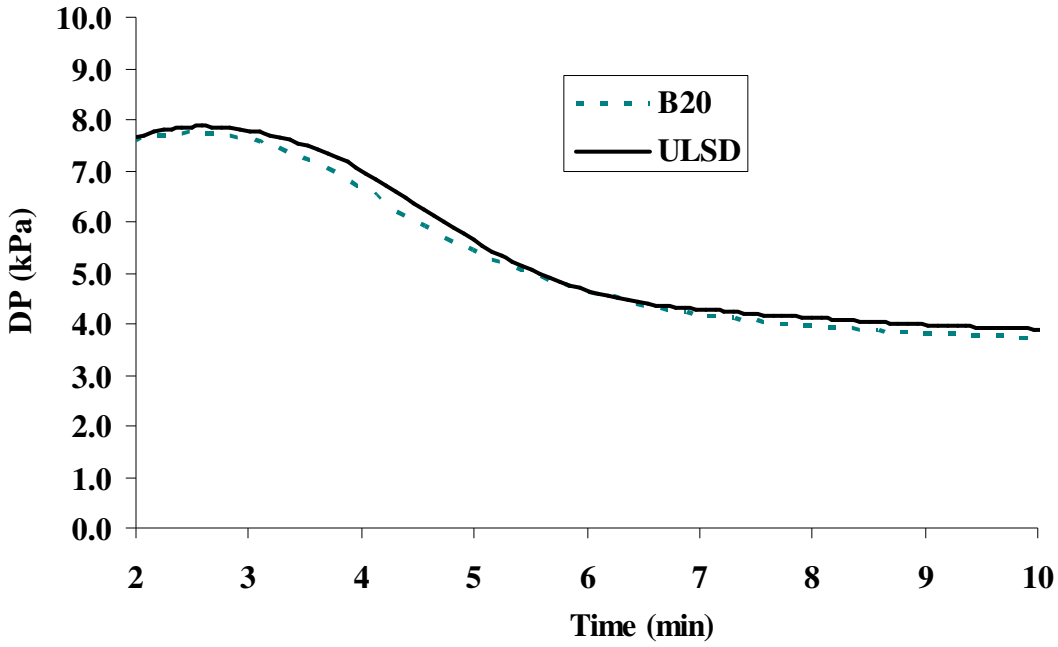

Figure 4.9. Regeneration rate results for B20 and ULSD

Holding the regeneration temperature shows the soot loaded with B20 has a faster regeneration rate compared to the soot loaded with ULSD. This data is similar to data reported in previous studies [39, 60]. Explanations of the faster regeneration rate

are accredited to the soot of the B20 being more reactive due to higher oxygen content and amorphous soot structure [35].

4.1.6 Exhaust speciation during regeneration

During regeneration, a catalyzed DPF uses the conversion of NO into the aggressive soot oxidant NO_2. The potential of a small increase in NOx emissions when B20 is used could be a factor for the faster regeneration rate and lower regeneration temperature required when compared to soot loaded with ULSD. The use of an oxygenated fuel such as biodiesel could supply more oxygen to the catalyzed DPF surface enhancing DPF regeneration. Therefore, analysis of the exhaust speciation before and after the catalyzed DPF could be useful in understanding this result during DPF regeneration.

Tests were conducted to measure the CO_2, H_2O, NO, NO_2, and NOx emissions before and after the catalyzed DPF during a regeneration event. Unregulated exhaust species formaldehyde, acetaldehyde, ethylene, ethane, and methane were also measured to further understand the impact of soot loaded with B20 fuel and the effect it has during regeneration. All speciation data was taken using an MKS-2030 high speed FTIR multi-gas analyzer.

Figure 4.10 shows the methane, ethane, formaldehyde, and ethylene present in the exhaust stream before and after the DPF during the active regeneration event. The data depicts the transient response of the species measured by the FTIR during the first 8 minutes of regeneration. The first 30 seconds of data is the exhaust at a steady state

condition. The first peak shown in the figure is a result of the initialization of the post injection strategy. The temperature before the DPF rapidly increases as a result of the exothermic reaction of the hydrocarbons on the DOC catalyst which corresponds to the initial peak of the methane, the formaldehyde, and the ethane concentrations. Comparison of the two fuels used shows that the formaldehyde for B20 is higher than that of ULSD. This is possibly due to the additional oxygen found in B20. ULSD also has a 'delayed' formation of formaldehyde compared to B20. This is attributed to the decreased oxygen concentration in the exhaust stream with ULSD compared to B20.

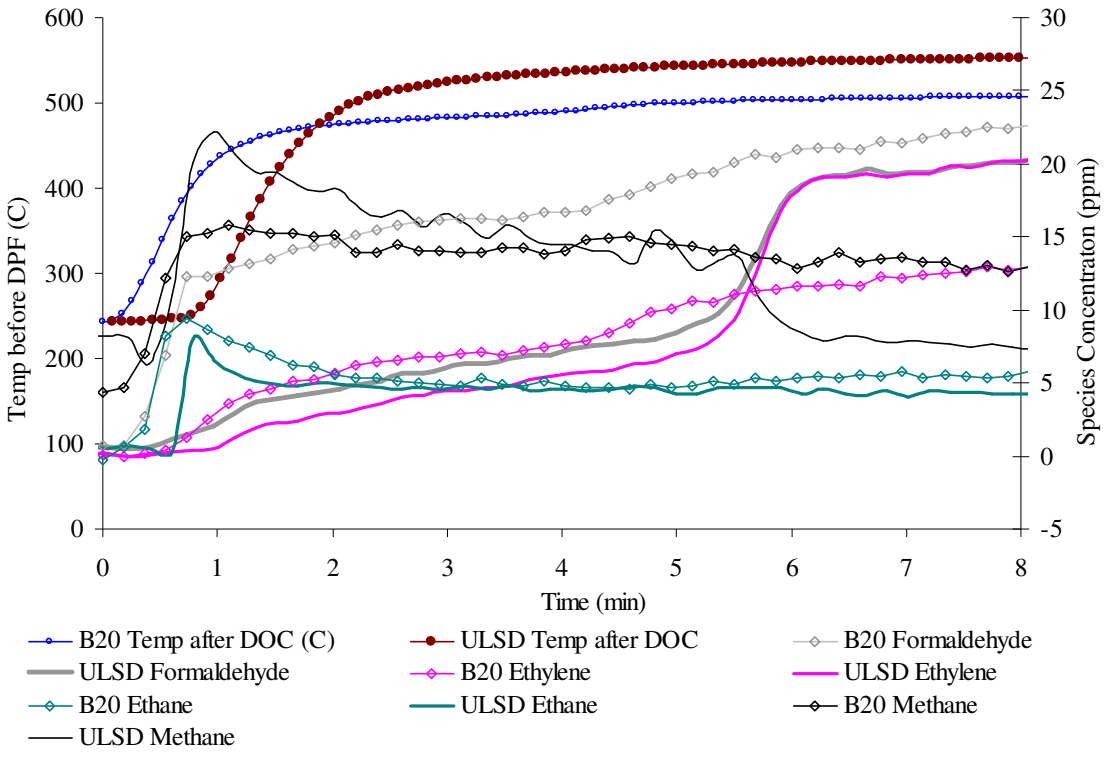

Figure 4.10. Speciation of the exhaust before the cDPF for B20 and ULSD

Figure 4.11 and 4.12 show the H_2O and CO_2 after the DPF for ULSD and B20 respectively. A sharp increase is seen for both H_2O and CO_2 after the DPF with B20, with a more gradual increase of these species for ULSD. This suggests that the B20 products, specifically formaldehyde and acetaldehyde produced after the DOC, are more reactive than the ULSD products. This increase in the oxygenated species will increase the regeneration rate of the DPF.

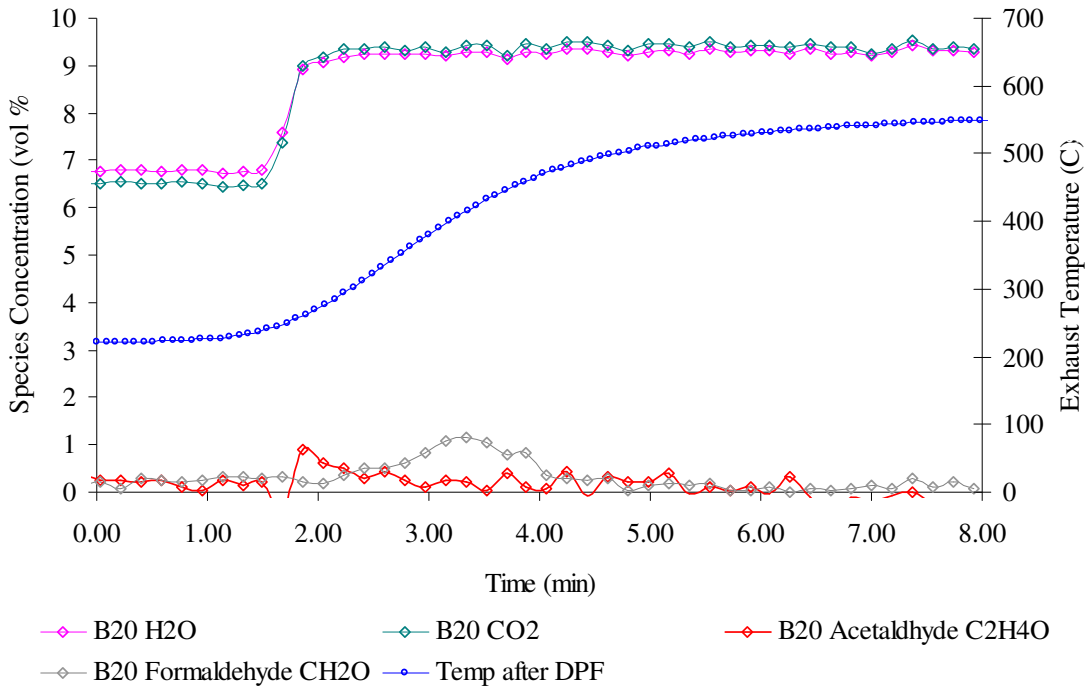

Figure 4.11. CO_2%, H_2O%, C_2H_4O, and CH_2O after the DPF during regeneration with ULSD

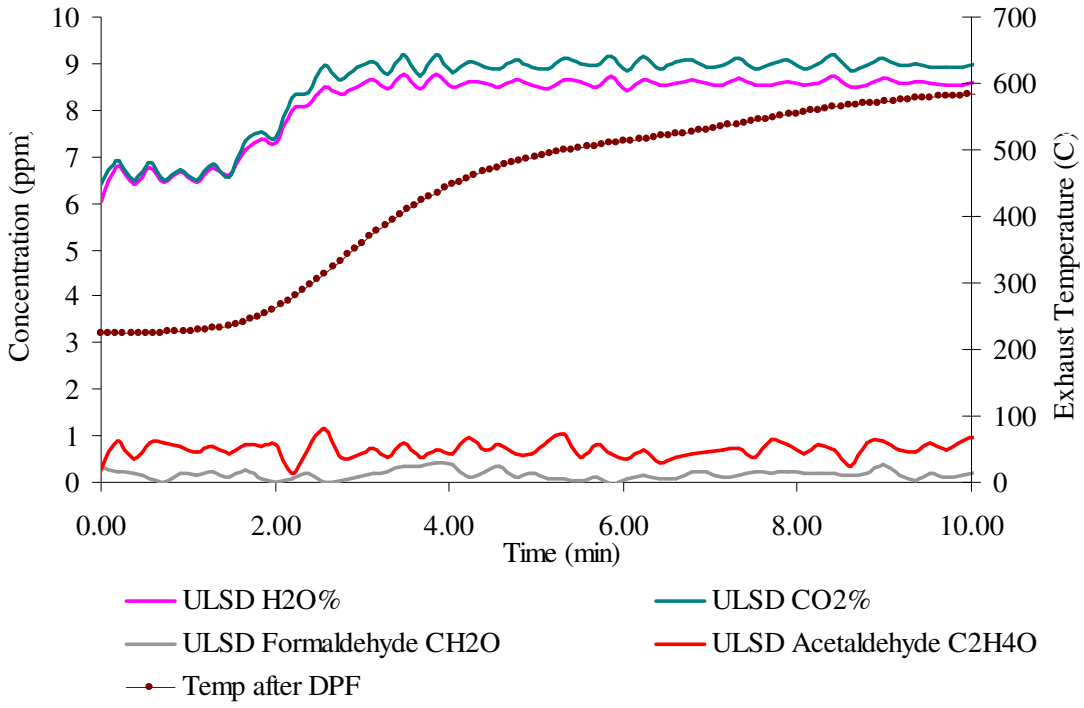

Figure 4.12. CO_2%, H_2O%, C_2H_4O, and CH_2O after the DPF during regeneration with B20

The potential of increased availability of NOx with the use of B20 fuel is of interest during regeneration of the cDPF. NO_2 is a very aggressive soot oxidant which could lead to faster regeneration rates with B20 compared to ULSD. Analysis of the NO/NO_2 ratio over the cDPF in figure 4.13 shows that after 8 minutes, B20 has an 88% ratio compared to 75% ratio NO/NO_2 with ULSD.

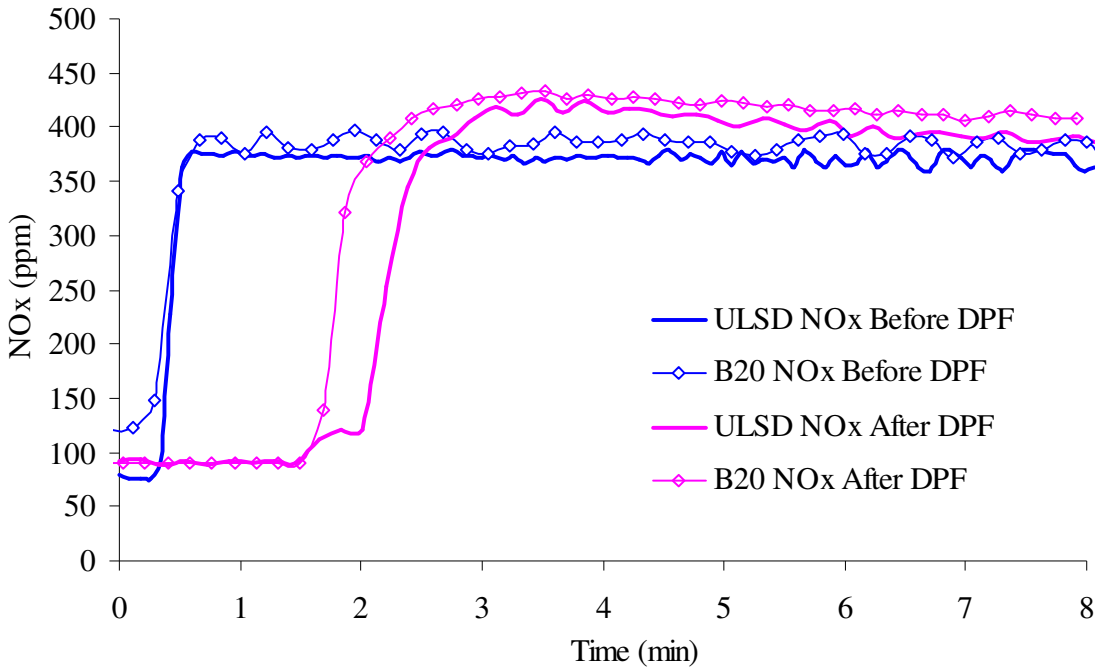

Figure 4.13. NO/NO_2 ratio over the DPF during regeneration for B20 and ULSD

Figure 4.14 shows the exhaust speciation after the DPF. As seen from the graph, the catalyzed DPF is very proficient at eliminating the ethane, ethylene, and formaldehyde to trace levels after 8 minutes of operation during regeneration. However, methane which shows the same trend for both ULSD and B20 is higher for the B20 fuel.

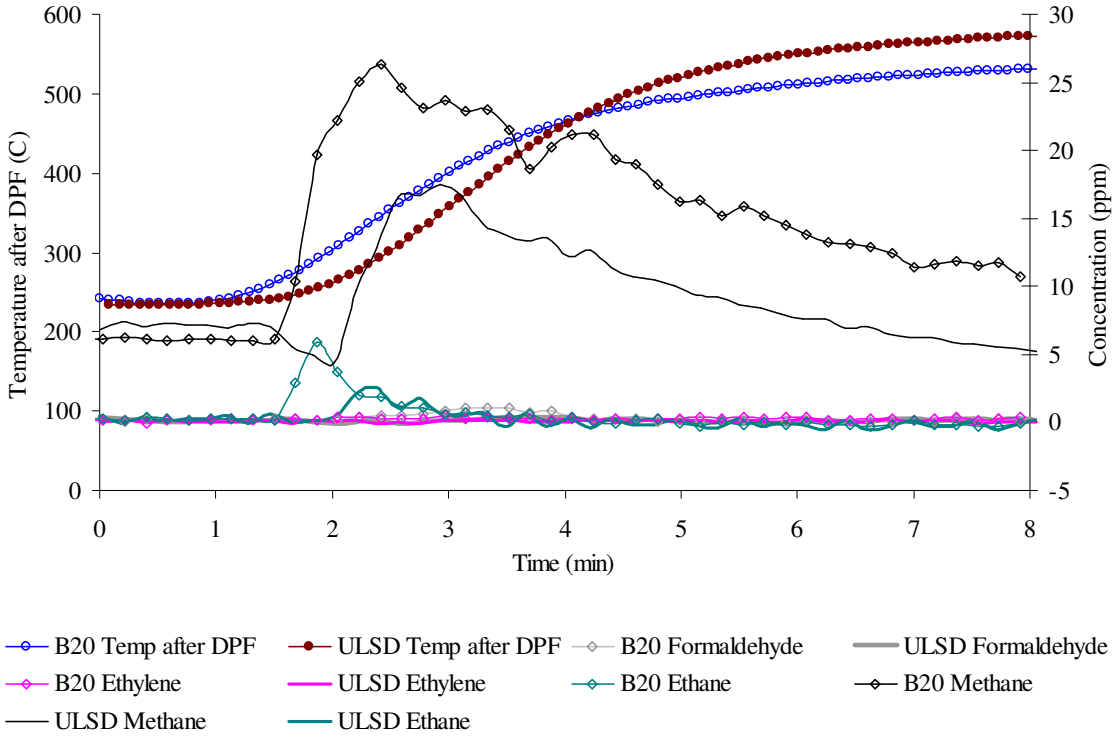

Figure 4.14. Speciation of exhaust after the cDPF for B20 and ULSD

4.2 Engine Oil Dilution

An engine equipped with an actively regenerated DPF can lead to fuel dilution of the engine oil. The dilution of the fuel in the engine oil is a function of the engine operating strategy and the properties of the fuel used [48, 49]. Biodiesel, in particular, is made of fatty methyl esters, which have different physical attributes compared to ULSD: higher surface tension, higher viscosity and lubricity, and lower volatility. Research by Andreae et al. found that the engine oil dilution due to post fuel injection was 40% higher by B20 than by ULSD [48].

The mechanism for oil dilution, regardless of fuel used, is driven by the low volatility components in the fuel. These low volatile components require longer vaporizing after injection, which may lead to deposition on the cylinder walls during combustion. As the piston moves down during the power stroke, these deposits can be pushed down into the crankcase. Fuel dilution of the motor oil can be detrimental to an engine and its components. Viscosity, in particular, is an important factor in the quality of the engine oil. As the viscosity decreases metal to metal contact can occur causing catastrophic failure of bearings and the wearing of the pistons and rings.

4.2.1 The Engine Oil Sensor

The engine oil viscosity is measured with an on-board prototype oil condition sensor provided by Delphi Corporation. The oil condition sensor is designed to measure both viscosity and soot of engine oil in situ. The engine oil pan has been modified to accommodate the sensor as shown in figure 4.15.

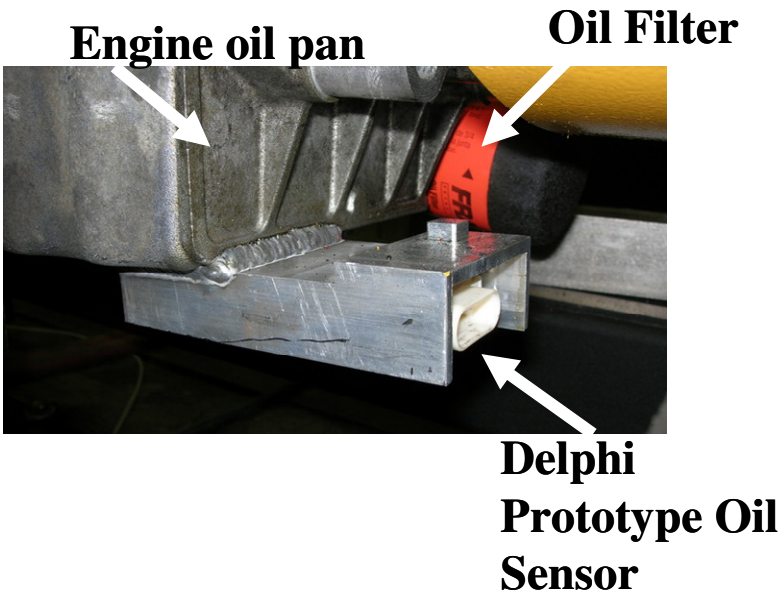

Figure 4.15. Delphi Oil Sensor mounting to the engine oil pan.

The sensor is engaged once the temperature of the engine oil reaches 77℃ and the viscosity measurement automatically begins. The sensor proceeds through the algorithm outputting the value of the viscosity registered at 70 ℃ and the percentage of soot in the engine oil.

Figure 4.16 shows an analysis of the viscosity of engine oil (0W40) diluted by B20 at various concentrations, which was measured using a bench viscometer. All concentration data above 10% is extrapolated.

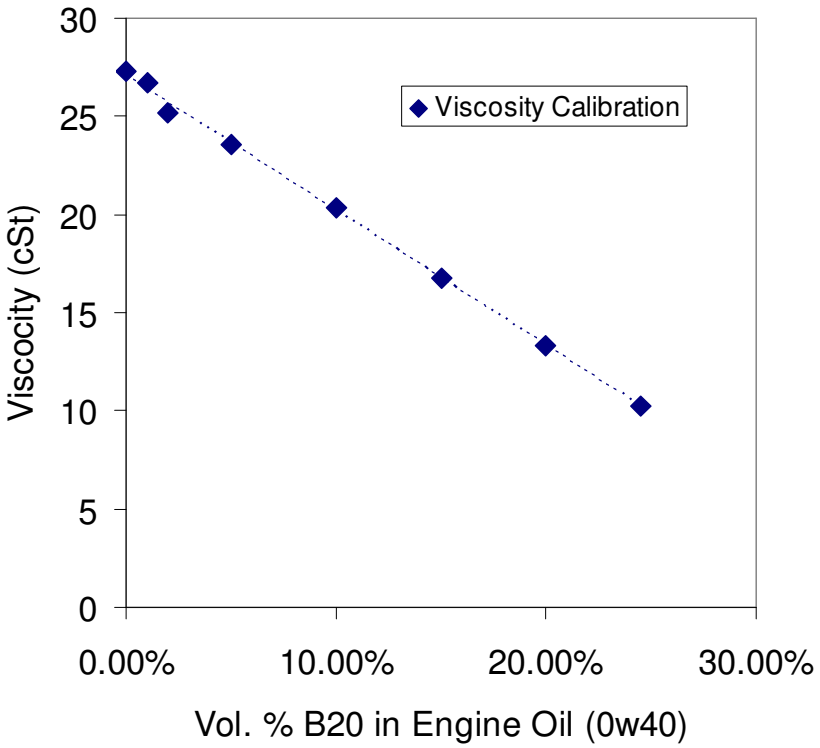

Figure 4.16. Viscosity of the engine oil with different concentrations of B20 using a bench viscometer

4.2.2 Experimental procedure

Initially, an oil change is done using Mobil One fully synthetic lube oil (SAE0W40). The engine is then run for 20 min without post injection and a control oil sample is then taken. Each oil sample is taken utilizing a syringe device shown below. The small tube is inserted into the oil dip stick location and approximately 35ML of engine oil is removed. This procedure is then repeated at a 20 minute interval for duration of 3 hours to ensure adequate dilution of the engine oil. No additional oil is added to the engine for the duration of the test.

The engine operating point used for the test is steady state at a speed of 1200 rpm and load at 80 ft-lb with post injection to simulate active regeneration. The post injection strategy is held constant at 40 degrees aTDC with a quantity of 10mm^3/inj. Test analysis is done with B20 fuel only. The samples are then analyzed using the Fourier Transform Infrared Spectroscopy (FTIR) method. All analysis is provided by National Biofuels Energy Laboratory at Next Energy.

4.2.3 Effect of active regeneration strategy on viscosity

Methyl ester in biodiesel gives rise to a signature peak in FTIR spectra, which is not present in engine oil consisting mainly of long-chain hydrocarbon molecules. To quantify the oil dilution by B20, 20 vol. % of biodiesel was first blended into the ultra low sulfur diesel to make a B20 fuel. Varying amounts of B20 were added to the engine oil to establish a calibration between the signature peak intensity in FTIR and the quantity of B20 in the engine oil.

The following figure shows the FTIR analysis results from the contaminated engine oil samples. Time zero indicates the fresh engine oil warmed up for 20 minutes with no post injection. The FTIR analysis indicates 1.9% dilution of B20 in the engine oil with no post injection strategy used. This is possibly due to any residue oil that may have remained inside the engine oil pan from prior work done utilizing DPF regeneration.

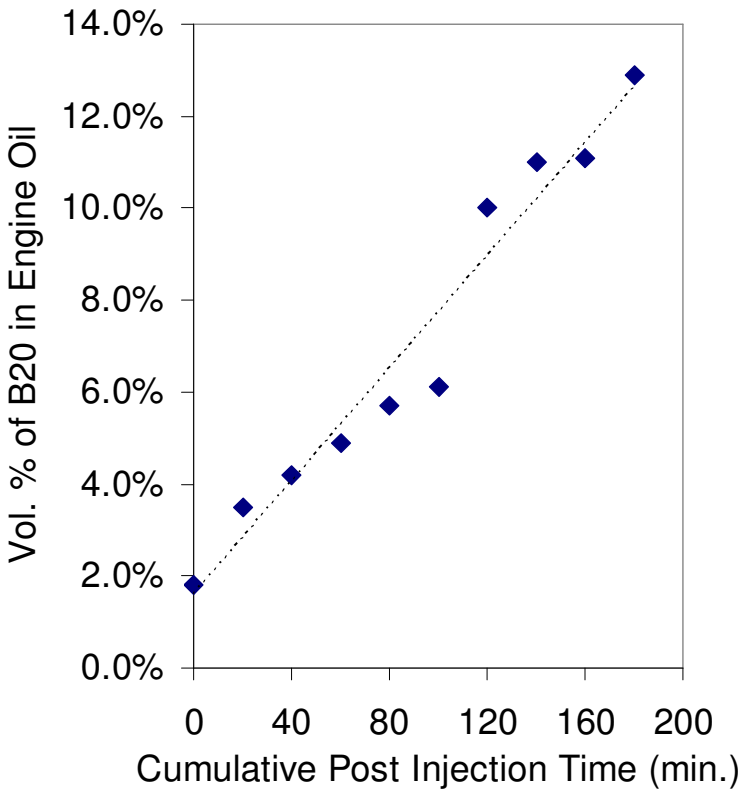

Figure 4.17. FTIR analysis of B20 percentage in engine oil during the regeneration mode

Comparing the FTIR analysis of the engine oil to the results obtained using the Delphi oil sensor produces reasonable results for an onboard sensor, about a 10% difference. FTIR analysis after 180 minutes of post injection indicates 12.9% biodiesel in the engine oil compared to 11.6% using the oil sensor with a viscosity measurement of 19.2 cSt

Figure 4.18 shows the viscosity measurement using the Delphi on-board oil sensor. Two tests runs are shown in the figure where each run indicates fresh engine oil at about 26.6 cSt. No soot was observed due to the short hours of engine operation.

The first test run shows the degradation of the engine oil under normal operating conditions. The post injection strategy is used on the second to last data point with the final viscosity measurement showing severe engine oil dilution: 10%-15% fuel dilution within 3-4 hours of post injection.

Further analysis at this point is shown in the FTIR (Fourier Transform Infrared) spectra in figure 4.19. The FTIR analysis is performed at The National Biofuels Laboratory on a FTIR spectrometer from Perkin Elmer. This technique provides information about the chemical bonding or molecular structure of the oil sample. During FTIR analysis, the sample is exposed to an infrared beam. The sample's transmittance and reflectance of the infrared rays at different frequencies is recorded into an IR absorption plot. The recorded frequency or wave number is recorded in the x-axis and absorption is recorded in the y-axis. The plot is then compared to known signatures of identified materials in the FTIR library to determine the molecules present in the sample.

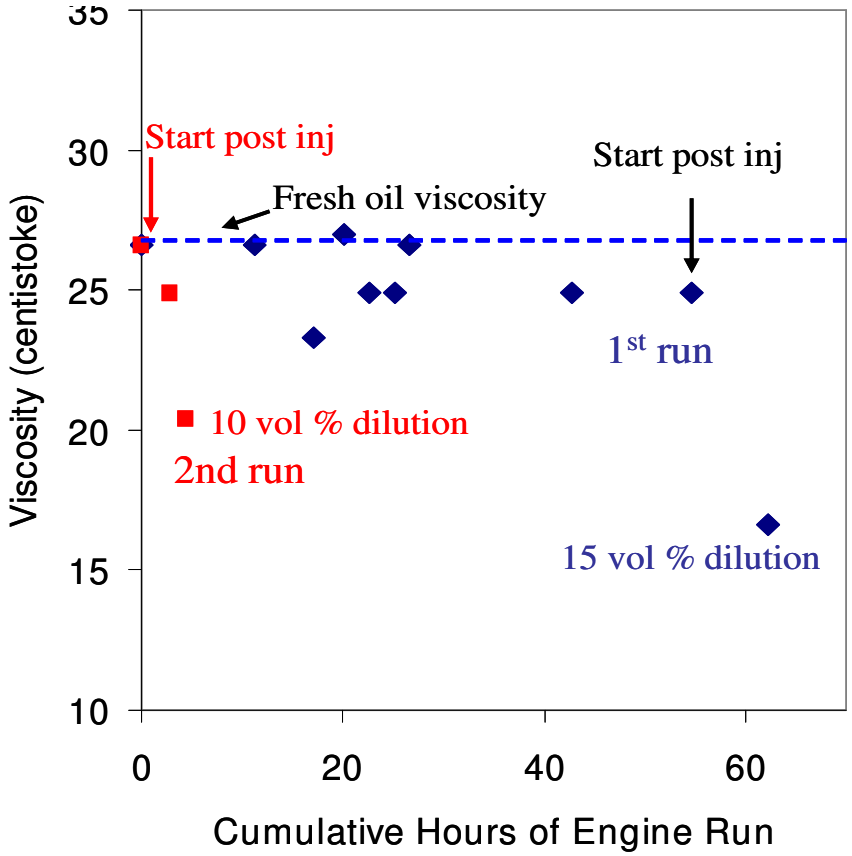

Figure 4.18. Delphi oil sensor measurement of engine oil viscosity during regeneration with B20

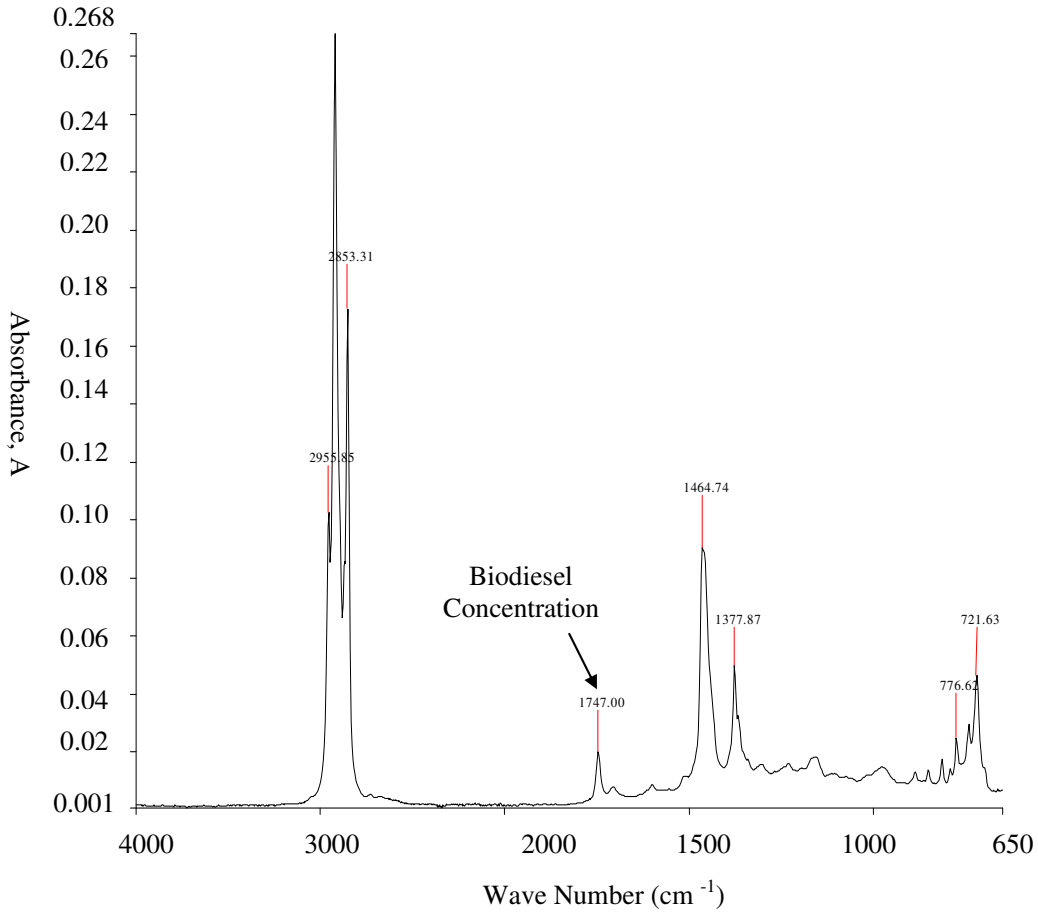

Figure 4.19. FTIR spectra of first run showing 15% fuel oil dilution

Figure 4.20 shows the viscosity measurement from the Delphi sensor using B20 with multiple post injection events. For this test, the engine oil is changed and a baseline viscosity measurement is taken. Multiple post injection events are done with the viscosity measured immediately following. The engine is then run at normal operating conditions with the viscosity measurement taken immediately following. The decrease in engine oil viscosity can be seen in figure 4.20 immediately following the post injection event. An increase in the engine oil viscosity is also seen after normal

engine operating conditions. This is attributed to the evaporation of B20 and flow back to the combustion chamber, a mechanism that is suggested in the literature as well [48].

Figure 4.21 highlights the comparison measuring the viscosity of ULSD and B20 with multiple post injection events. It appears that the viscosity of the oil diluted by ULSD is able to recover more readily than by B20 under normal engine operating conditions, as shown in the figure. The biodiesel component of B20 fuels tend to remain in the engine oil because of its lower volatility[48]. Overall, initiation of a post injection strategy shows severe engine oil dilution over time for both ULSD and B20.

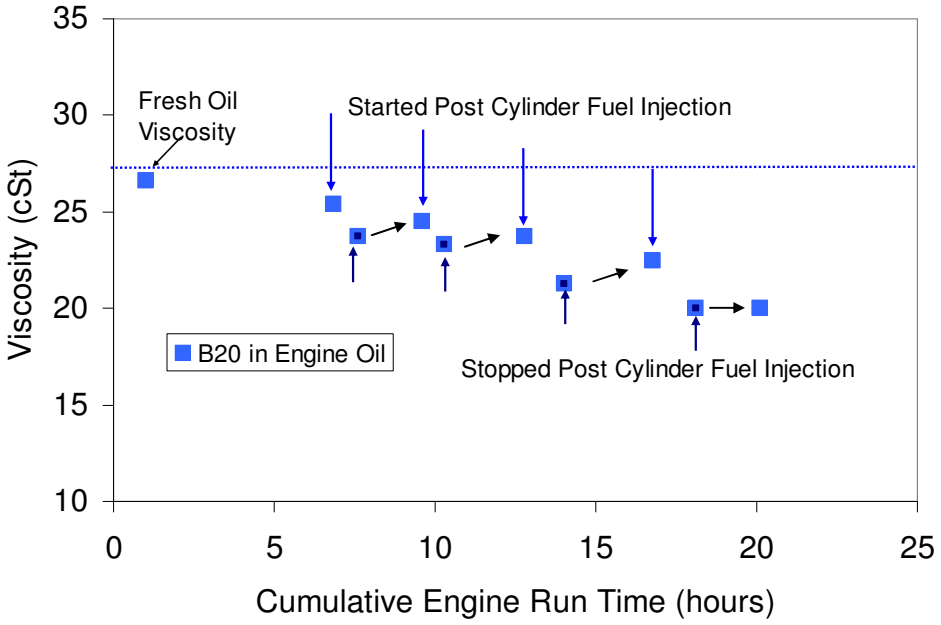

Figure 4.20. Measurement of the viscosity during multiple regeneration events with B20

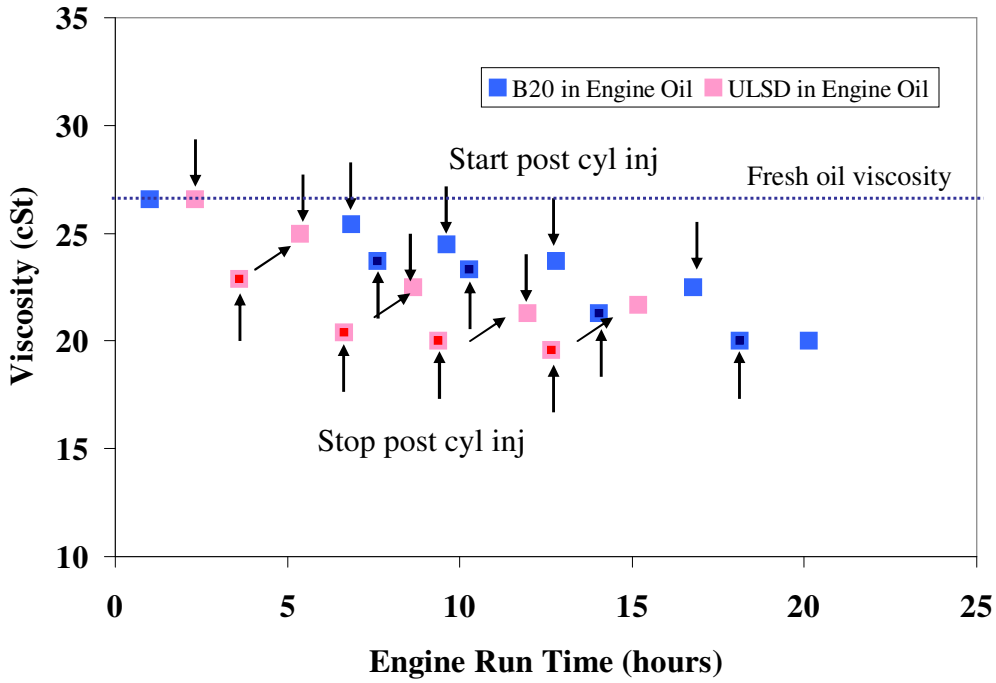

Figure 4.21. Comparison of ULSD and B20 effect on the viscosity during multiple regeneration events

Implementation of aftertreatment systems are significantly affected with the use of B20 fuel compared to ULSD. The conclusions with respect to DPF loading and regeneration are as follows:

- B20 has a reduction in engine out soot which correlated to an increased cDPF loading time by 21% to attain the target loading weight of 20 grams.

- The lower PM produced with B20 will increase the amount of time it takes to load the DPF, thereby reducing the number of regenerations required and increasing the overall life expectancy of a cDPF.

- The temperature at which regeneration occurred was reduced by 63℃ compared to the soot loaded with ULSD.

- Comparison of the speciation results showed that the oxygenated species, formaldehyde and acetaldehyde, were found to be higher for B20 than ULSD. This was attributed to the additional oxygen that is found in B20.

- Both water and carbon dioxide showed a sharp increase in concentration after the cDPF indicating that products produced after the DOC with B20 are more reactive than ULSD products.

- NOx data showed a minimal increase with the use of B20 fuel over the regeneration event.

- The speciation data confirmed that additional oxygenated species are present and/or more reactive with B20 possibly aiding in the faster regeneration rate of soot loaded with biodiesel.

The following conclusions focus on the engine oil dilution portion of the paper.

- Severe degradation of the engine oil was found after three hours of post injection measuring 12.9% biodiesel diluted in the engine oil and a 26% drop in engine oil viscosity.

- An onboard viscosity oil sensor provided by Delphi Corporation was tested. The sensor was in good agreement with the viscosity bench test analysis and provided oil viscosity measurement over the course of the project.

- Evaporation or flow back of the fuel to the combustion chamber from the engine oil was shown. B20 has less of a recovery during normal engine operation leaving more fuel in the engine oil compared to ULSD. This will lead to faster deterioration of the engine oil when B20 is used. This was attributed to the lower volatility components that are found in biodiesel.

- Operation with B20 shows significant fuel dilution and needs to be monitored to prevent engine deterioration.

CHAPTER 5

DATA ACQUISITION AND ANALYSIS OF COMBUSTION AND EMISSIONS

The following chapter analyzes the performance of combustion and emissions operating the engine in the Low NOx Combustion (LNOxC) regime. In addition, the performance and emission characteristics are investigated as a function of the ECU injection strategy. The addition of pilot injections is found to effectively reduce combustion noise and extends the injection retard window to reach LNOxC combustion regimes with acceptable noise level for LD diesel engines.

5.1 Low NOx Combustion

Modification of engine calibration is significant in effecting the quantity of emissions when fueled with B20 or ULSD. Therefore, a comparison of timing sweeps, speed sweeps, and multiple injection strategies are done to look at the effect of engine combustion on emissions, heat release, pressure trace, and fuel consumption when operating in the low NOx combustion regime.

As the injection timing is advanced, the combustion characteristics move from a conventional diesel mode of combustion to a more premixed, and low NOx combustion (LNOxC), with lower engine out NOx and soot but higher THC and CO emissions. Pilot injections effectively reduce combustion noise and extend the injection retard window to reach LNOxC combustion regimes with acceptable noise level for LD diesel engines.

5.1.1 The Experimental Configuration

The engine is coupled to a 112kW General Electric eddy current dynamometer used to load and motor the engine for steady state testing. Continuous measurement of emission products including NO, NOx, THC, CO_2 and CO is done using a Horiba-OBS 2200. The Horiba utilizes a non-dispersive infrared (NDIR) heated analyzers to measure the CO and CO_2. The H_2O concentration is monitored to compensate the H_2O interference on the other two components. The sample gas is heated up to 120℃ so that wet sample gases can be measured without water extraction. The measurement of total hydrocarbon (THC) is done using a flame ionization detector (FID) and a chemi-luminescence detector (CLD) is used to measure NOx. The sample was maintained at 191℃ through heated sample lines and passed through a heated filter for removal of particulates. PM quantities are measured with an AVL smoke meter and exhaust speciation is carried out using a MKS multi-gas FTIR analyzer.

The aftertreatment system consists of a DOC followed by a cDPF as described early in chapter 4. All data is taken before the aftertreatment systems and represents engine out emission data.

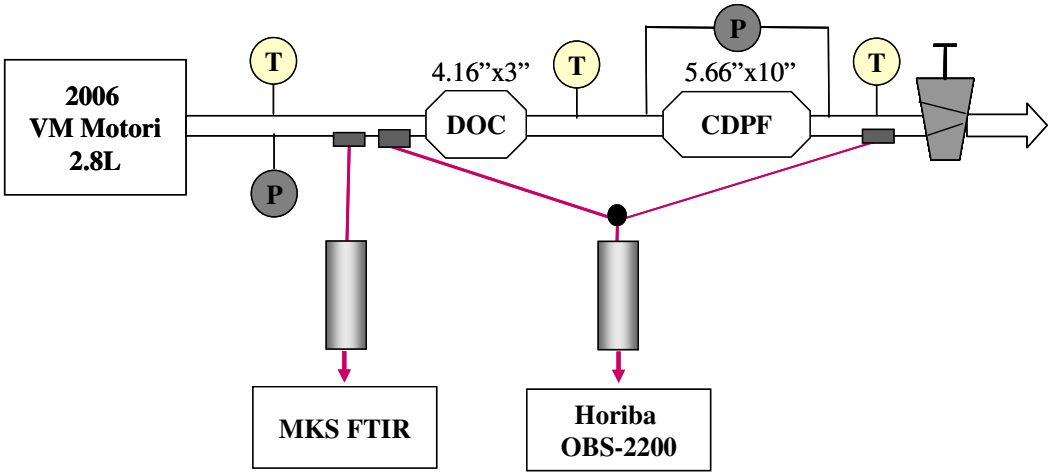

Figure 5.1. The engine setup schematic

The following speed sweep is conducted operating the engine in both a "reference" normal compression ignition direct injection (CIDI) mode which has two pilots and a main injection, and a low NOx combustion (LNOxC) mode utilizing only one injection. The speed sweep analysis employs the following test conditions. The main injection is fixed at 20 bTDC with a load of 3 bar BMEP. The engine speed is then varied from 1200 rpm to 2400 rpm. The reference CIDI was typical of the production calibration for this engine and ULSD fuel utilizing a dual-pilot main injection strategy. The engine operating conditions of the speed sweep are listed in table 5.1.

Engine Operating Condition	1200rpm 3bar BMEP		1800rpm 3bar BMEP		2100rpm 3bar BMEP		2400rpm 3bar BMEP	
Combustion Mode	Ref	LNOxC	Ref	LNOxC	Ref	LNOxC	Ref	LNOxC
EGR (%)	27	57	25	56	22	55	17	51
Pilot #1 SOI (CAD bTDC)	18.4	n/a	24.6	n/a	25.8	n/a	28.1	n/a
Pilot #2 SOI (CAD bTDC)	10.8	n/a	13.7	n/a	13.4	n/a	14	n/a
Main SOI (CAD aTDC)	5.1	-20	5.1	-20	3.4	-20	2.5	-20

Table 5.1. Speed sweep engine operating parameters

The EGR ratio indicated in the table above is the maximum rate attainable without an error from the ECU. The EGR valve is commanded fully open by the ECU and the backpressure valve was then manipulated to attain the same EGR ratios at different speeds while holding the BMEP constant for all cases. The LNOxC mode was achieved by advancing the main injection timing and increasing the EGR ratio. In addition, the preceding testing conditions were established by the research team to investigate the effect that injection strategy has on NOx. High loads were not investigated due to dynamometer limitations with the multi-cylinder engine in conjunction with high vibration and noise due to manipulation of the injection strategy. All the results shown in the following graphs are the average of 3 or more test runs.

5.1.2 Combustion performance of speed sweep

Figures 5.2 and 5.3 show the heat of release rate and cylinder pressure, as the speed is increased from 1200 rpm to 2400 rpm for both the B20 and ULSD experiments. Generally, the heat release analysis of B20 shows a slight advancement compared to the ULSD apparent heat release rate (AHRR). Similar findings by Senatore et al. show the heat release of biodiesel advanced 3-5 CAD with respect to TDC [61].

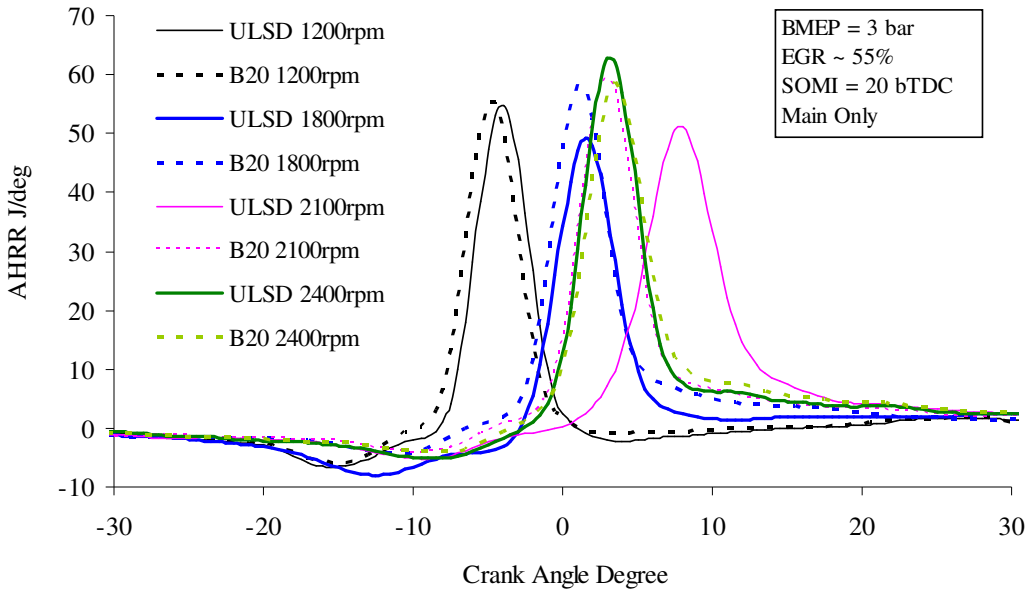

Figure 5.2. Effect on the heat release rate for ULSD and B20 main injection only strategy as a function of engine speed

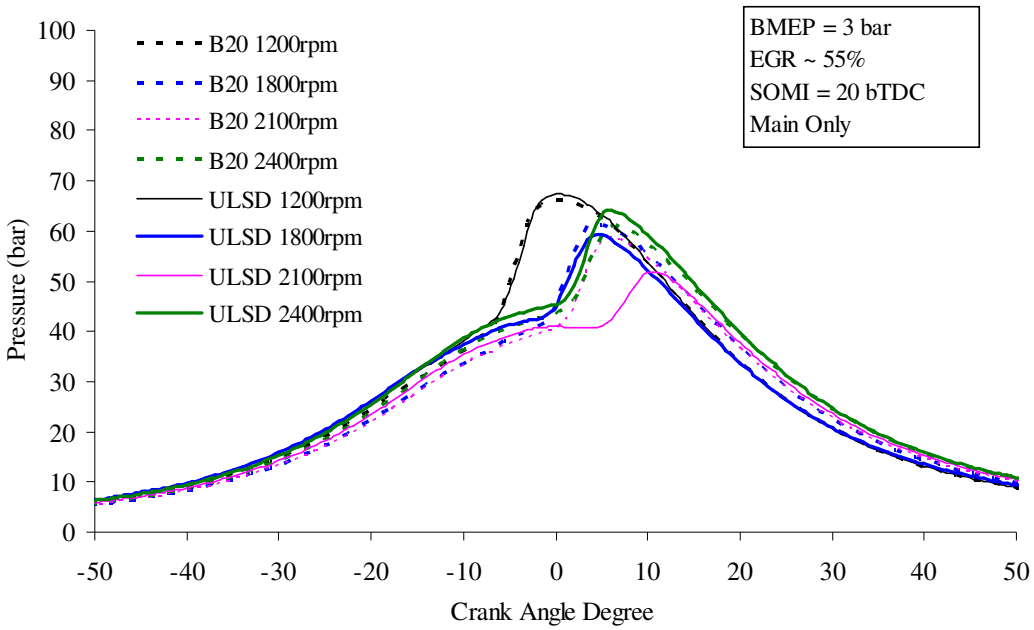

Figure 5.3. Effect on the pressure trace for ULSD and B20 main injection only strategy as a function of engine speed

Figure 5.4 shows the comparison of ignition delay for ULSD and B20 with a single fixed injection strategy and variable engine speed. The ignition delay is defined as the duration period between the start of injection (SOI) and the start of combustion (SOC). The SOC can be determined using the in-cylinder pressure trace or by the heat release rate. For this work, the SOC is defined as the change in slope from negative to positive of the heat release analysis [18]. The ignition delay is therefore defined as the period from the SOMI to the point of the combustion heat release trace crosses the motoring trace. Figure 5.5 shows the average heat release rate indicating the SOI and SOC for reference.

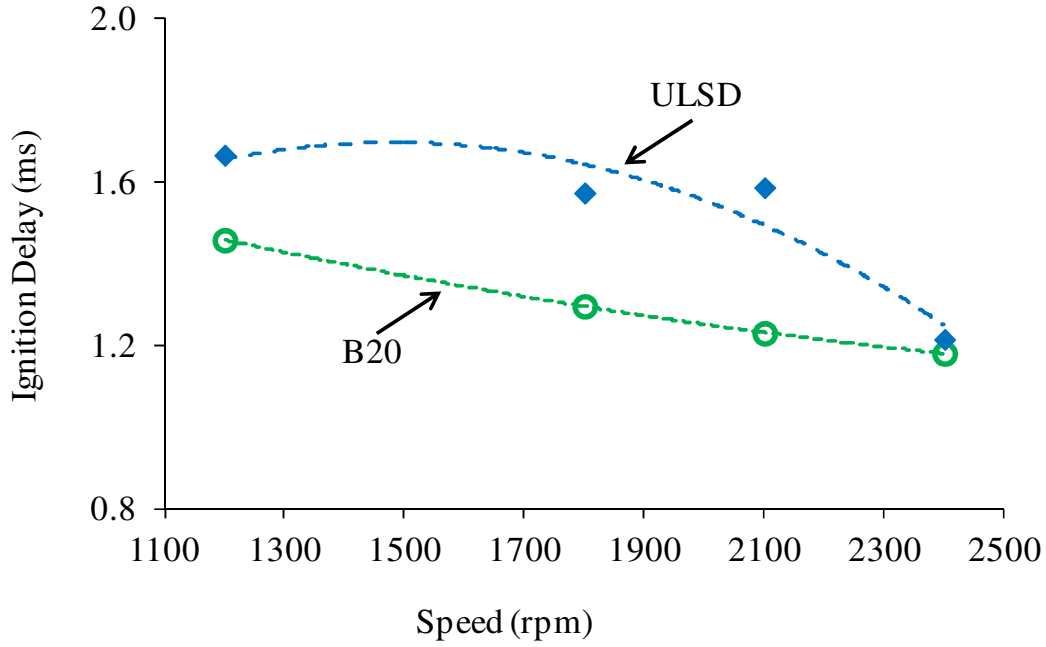

Figure 5.4. Effect on ignition delay for ULSD and B20 main injection only strategy as a function of engine speed

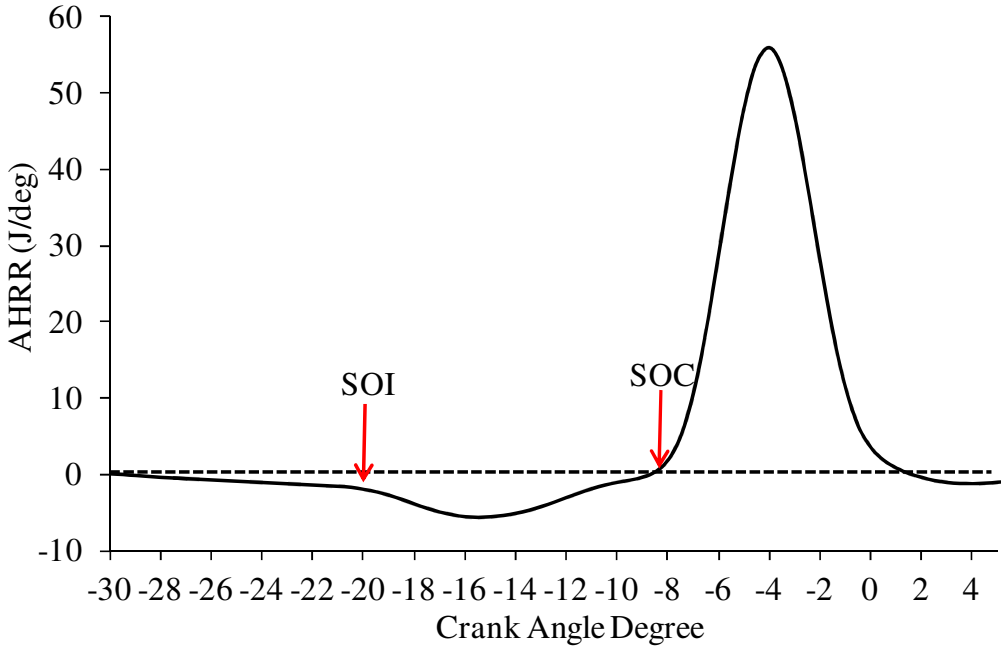

Figure 5.5. Graphical description of the ignition delay

5.1.3 Low NOx combustion effect on emissions

An effective diesel combustion strategy is to control the engine combustion to occur at lower temperatures. During conventional direct injection diesel combustion, the in-cylinder mixture is not homogeneous resulting in soot formation in the fuel-rich regions. Additionally, the high peak flame temperatures produce higher NOx emissions. Numerous approaches have been developed to lower the in-cylinder temperatures and encourage a more homogeneous mixture prior to combustion. Low NOx combustion strategies are achieved by increasing the EGR percentage, early and late SOI strategies, increased injection pressures, as well as multiple injection strategies.

Total Unburned Hydrocarbon Emissions

The unburned hydrocarbon emissions are shown in figure 5.6. The THC shows both a dependence on fuel and the combustion modes used especially at the higher speed points. The reference combustion mode shows an initial dip in THC and then a steady increase as the speed increases. Analysis of the AHRR plot in figure 5.7 shows a similar trend. After injection of the dual-pilot, there is a sharp drop in the HR due to the evaporation of the fuel

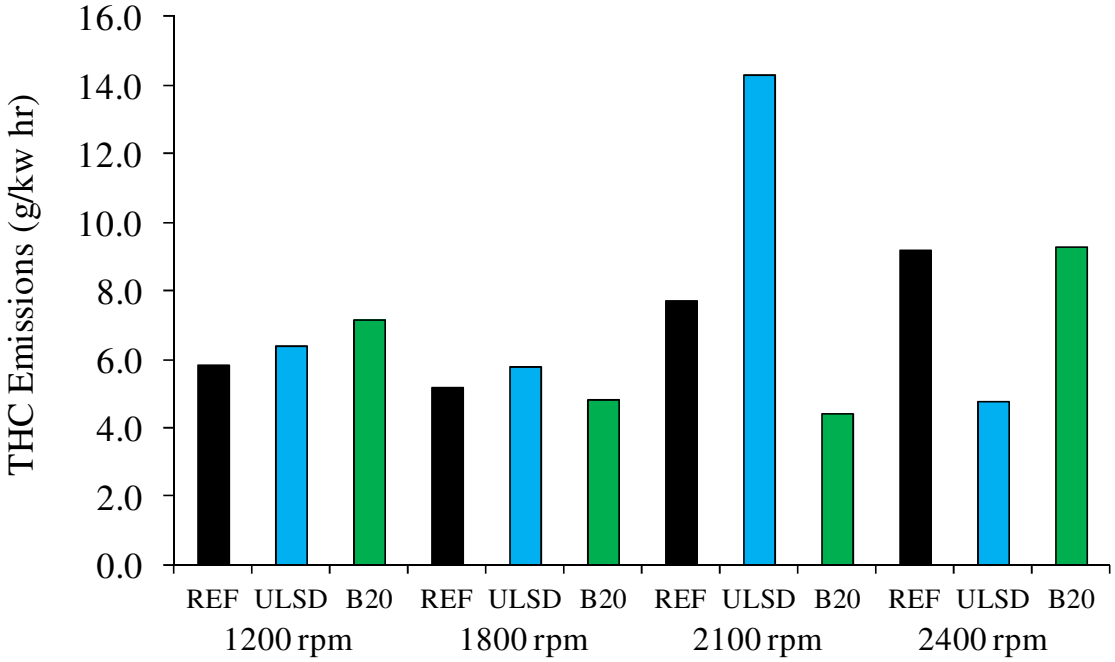

Figure 5.6. Total hydrocarbons emissions for the reference point in CIDI mode, ULSD and B20 in LNOxC mode

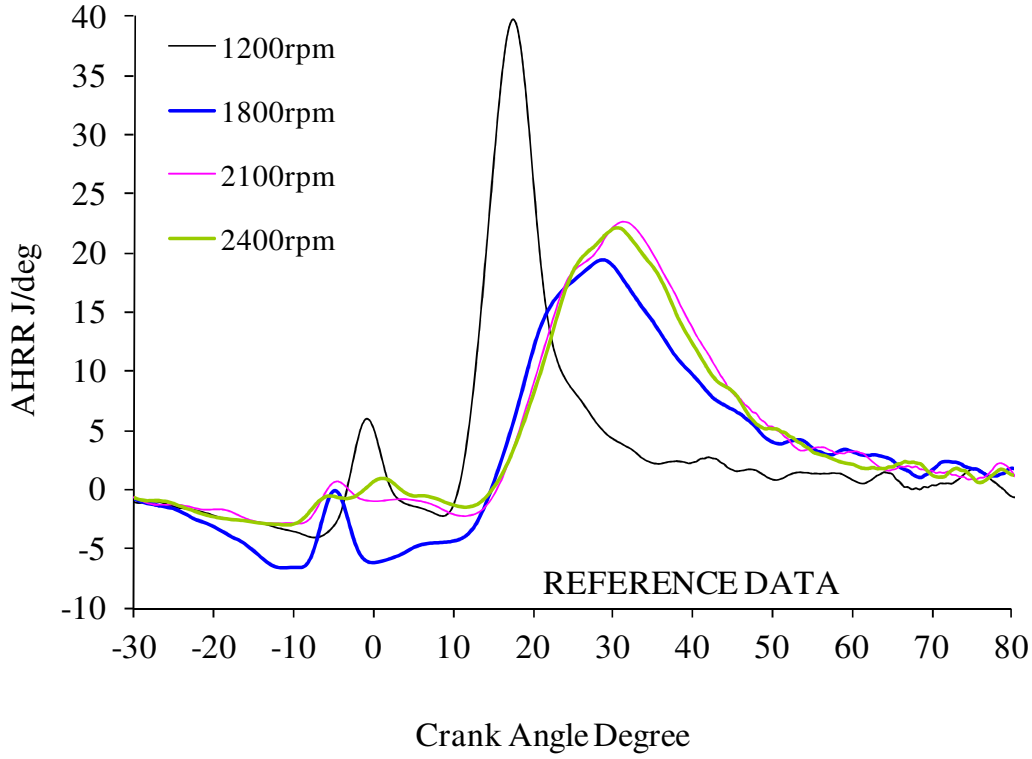

Figure 5.7. Apparent heat release rate for reference test point

NOx Emissions

The NOx emission data is shown in figure 5.8. Analysis of the reference mode data shows a spike in NOx at 1200rpm, then a drop and steady increase of NOx emissions at 1800rpm, 2100rpm, and 2400rpm, respectively. The reference combustion mode is the standard calibration of the multi-cylinder engine. As the engine increased in speed the EGR valve was not held constant. This was done in order to represent typical engine calibration of the multi-cylinder engine. The EGR % gradually decreases with increasing speed in the reference mode leading to higher temperatures in the cylinder and higher formation of NOx. A slight increase in NOx emissions is shown with B20 compared to ULSD for all operating points with an exception at 2400rpm where B20 has lower NOx values. However, the NOx reduction averages about 70% in the LNOxC mode, with 82% and 78% reduction at the 2400rpm point for ULSD and B20 respectively.

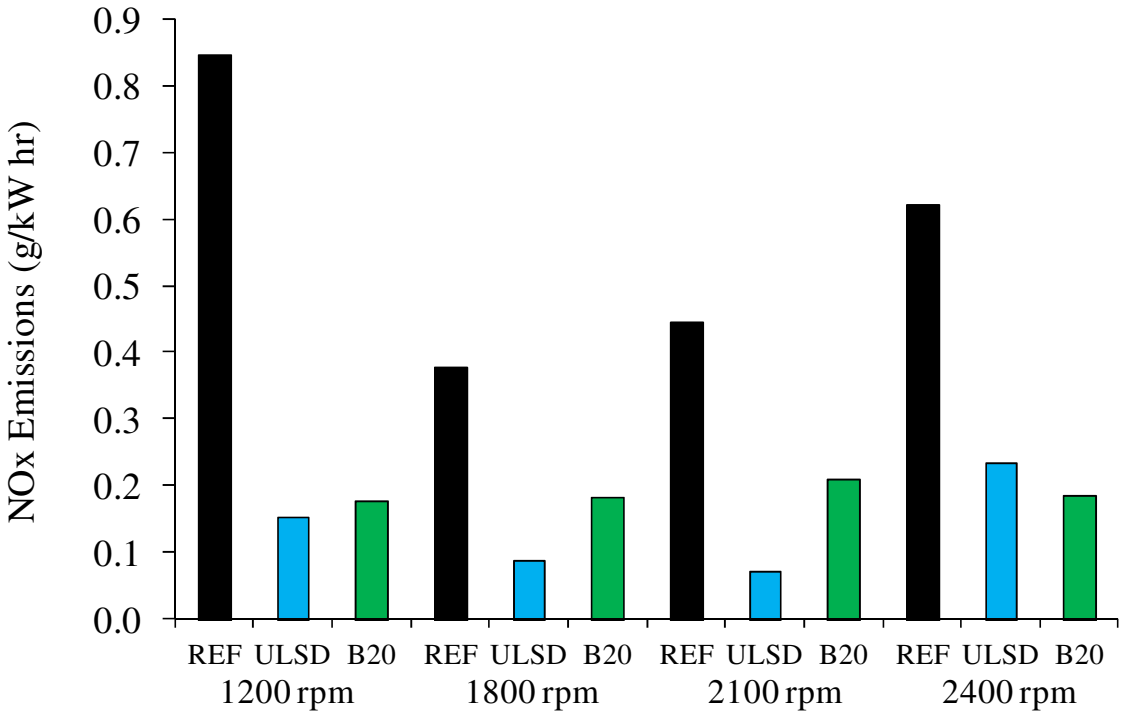

Figure 5.8. NOx emissions for the reference point in CIDI mode, ULSD and B20 in LNOxC mode

Carbon Monoxide Emissions

The carbon monoxide emissions are shown in figure 5.9. The CO emissions showed an increased in LNOxC mode compared to the reference point for ULSD but shows a reduction in CO when B20 is used with an exception at the higher speed point 2400rpm. Analysis of the heat release plot in figure 5.2 shows very little advancement of the AHRR compared to ULSD. This leads to later combustion in the cylinder increasing the CO as well as the THC emissions at this point. At lower speed, B20 shows a benefit in lowering CO emissions. This benefit is negated as the engine speed increases to 2400rpm. Carbon monoxide emissions are related to the temperature of the exhaust, where at higher temperature will decrease the amount of CO emissions.

The CO gradually increases for ULSD and B20 except at the speed point of 2100rpm for ULSD. Analysis of the AHRR shows the lowest HR peak and very late compared to the other speed point. This indicates a lower in-cylinder temperature which leads to an increase in CO emissions.

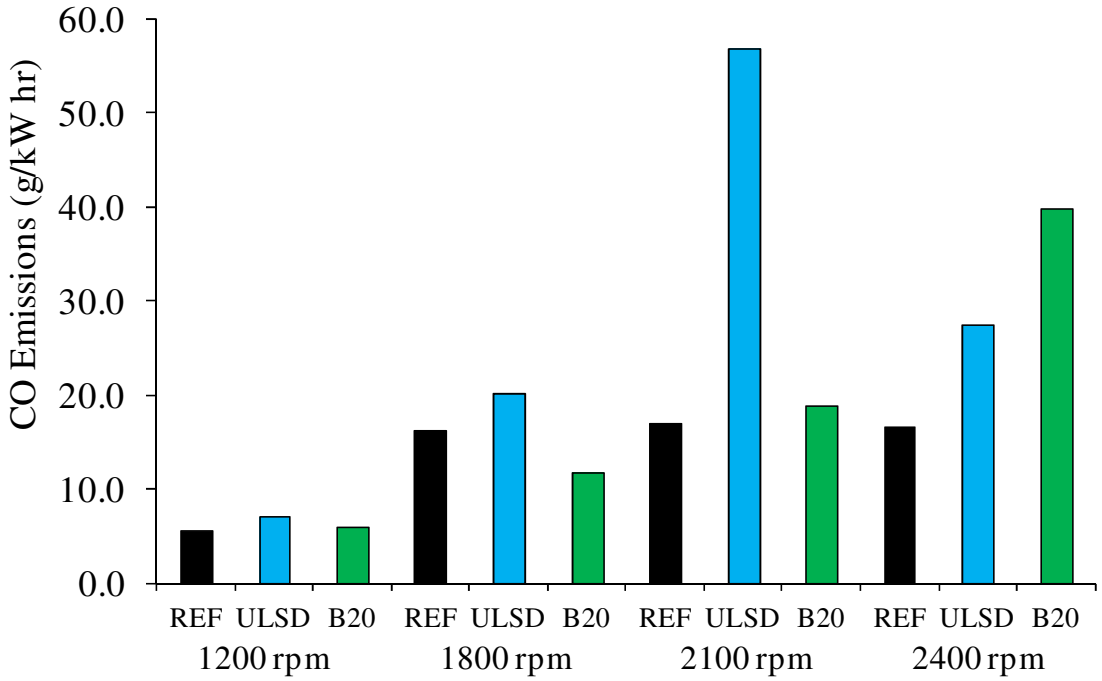

Figure 5.9. CO emissions for the reference point in CIDI mode, ULSD and B20 in LNOxC mode

5.1.4 Commanded SOI sweep

Figures 5.10 - 5.12 show the rate of pressure rise, cylinder pressure, and heat of release rate as the start of main injection (SOMI) is modified for the B20 experiments. All data is for the dual-pilot-main injection condition with the commanded main injection input from 9CAdeg to -9CA deg. Figure 5.13 shows the comparison of ignition delay for ULSD and B20 with a dual-pilot-main injection strategy and commanded SOMI.

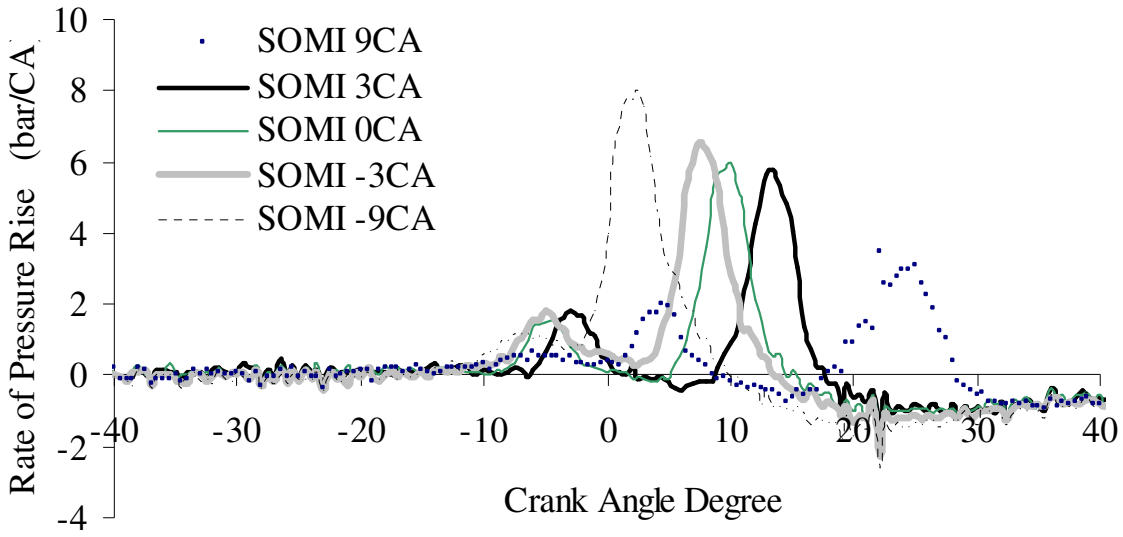

Figure 5.10. Rate of pressure rise for B20 experiments, dual-pilot-main injection sweep

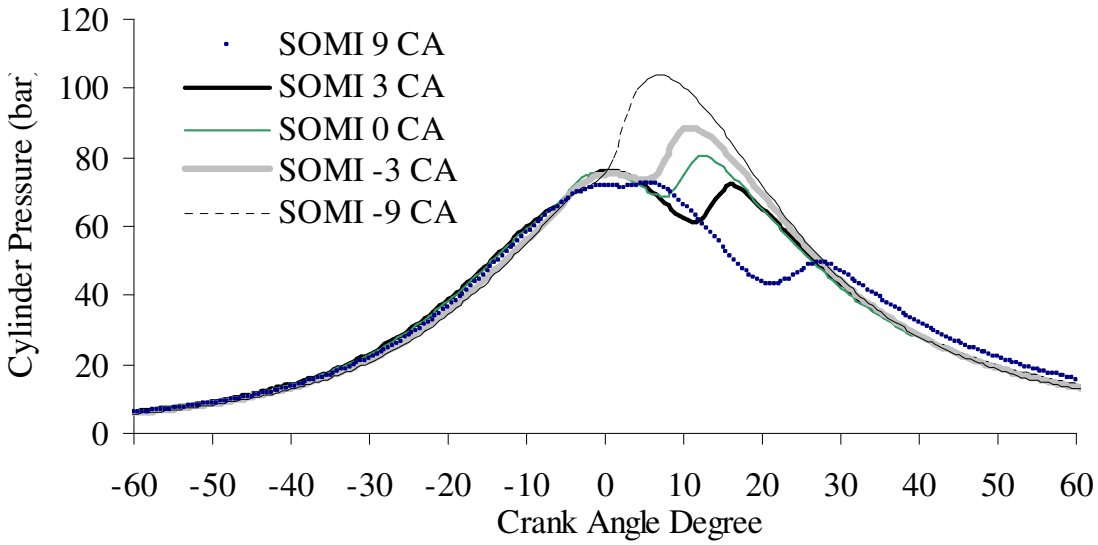

Figure 5.11. Cylinder pressure rise for B20 experiments, dual-pilot-main injection sweep

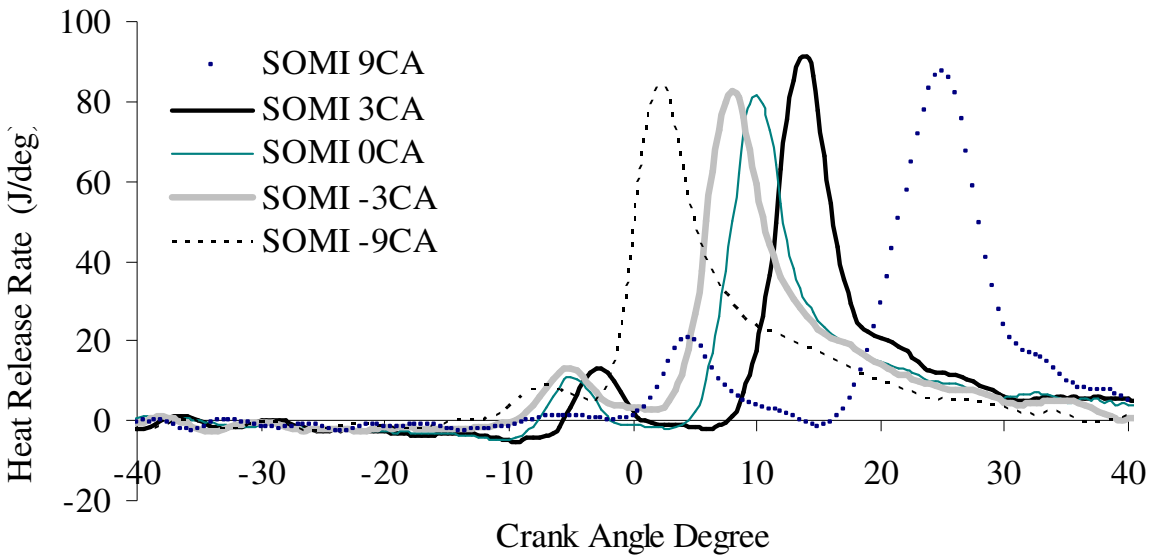

Figure 5.12. Heat release rate for B20 experiments, dual-pilot-main injection sweep

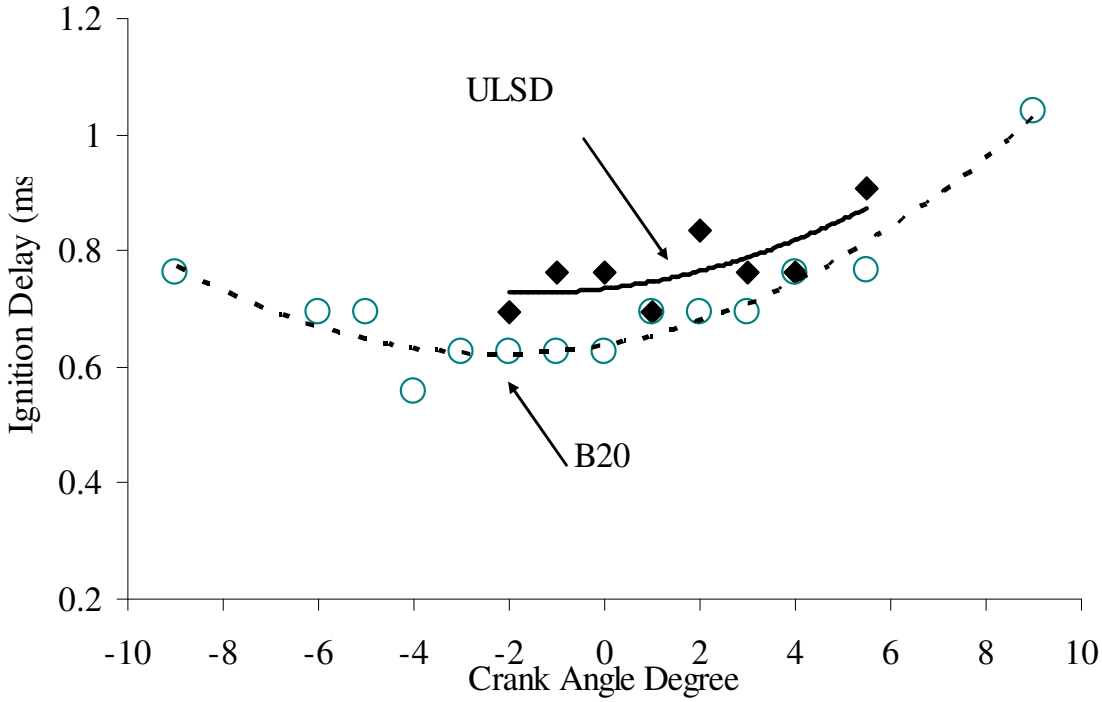

Figure 5.13. Ignition delay for B20 and ULSD experiments, dual-pilot-main injection sweep

5.1.5 Commanded SOI effect on emissions

Brake Specific Fuel Consumption

Analysis of the brake specific fuel consumption indicates an overall increase as the timing is retarded for all of the injection strategies used. Adding one pilot to the main injection develops a more premixed combustion, showing a decrease in overall fuel consumption.

On average, a 3% increase in fuel consumption was reported when using B20. This is consistent with the lower heating value of biodiesel. However, the injection strategy of one pilot and a main injection shows the best fuel economy, but dual-pilots have the best fuel economy and latest injection timing.

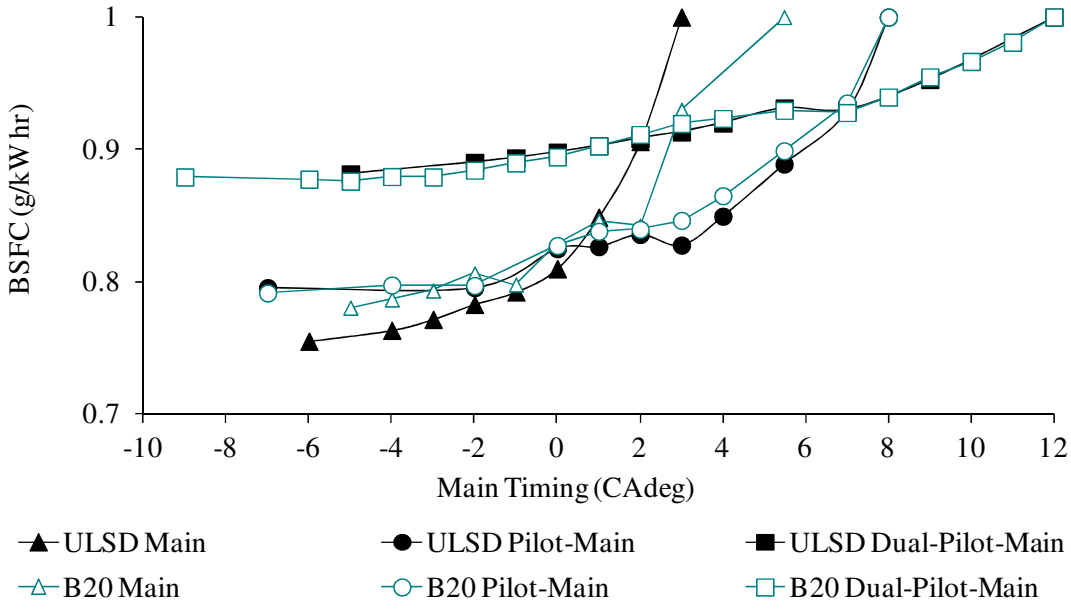

Figure 5.14. Comparison of the injection timing and strategy on BSFC

Total Unburned Hydrocarbon Emissions

The quantity of THC increases as the timing is retarded for both B20 and ULSD due to incomplete combustion and lower in-cylinder temperatures because of the late injection timing. However, comparing the different injection strategies, B20 produces 30% lower HC with one injection strategy as the timing is retarded, but the difference is negligible when one and two pilots are added. The less volatile components of biodiesel in the fuel accounts for the increase in THC for the main only injection; however, pilot injection effects, the ignition delay, and the premixed burn fraction along with the oxygen content of the biodiesel seem to even out the volatility effects of the biodiesel fuel components. Furthermore, comparison of THC quantity independent of fuel indicates that as the number of pilot injections are increased, less HC are produced due to combustion phasing, higher temperature and better mixing.

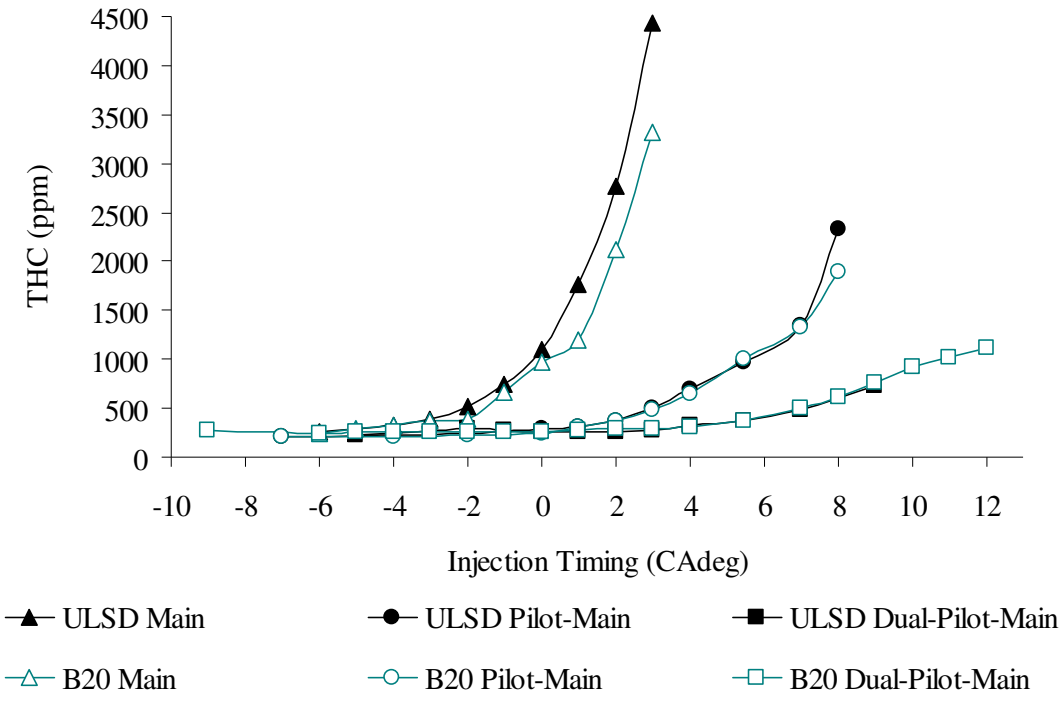

Figure 5.15. Comparison of the injection timing and strategy on THC

Carbon Monoxide Emissions

The trend of CO emissions is similar to that of the THC emissions. As the timing is retarded CO emissions increase independent of the injection strategy. However, increasing the number of pilots reduce up to 80% in CO emissions compared to a single injection event. The production of CO is very dependent on the injection timing. Severely retarding the timing with multiple injections for B20 produces slightly more CO than ULSD, but as the timing is advanced the differences are negligible.

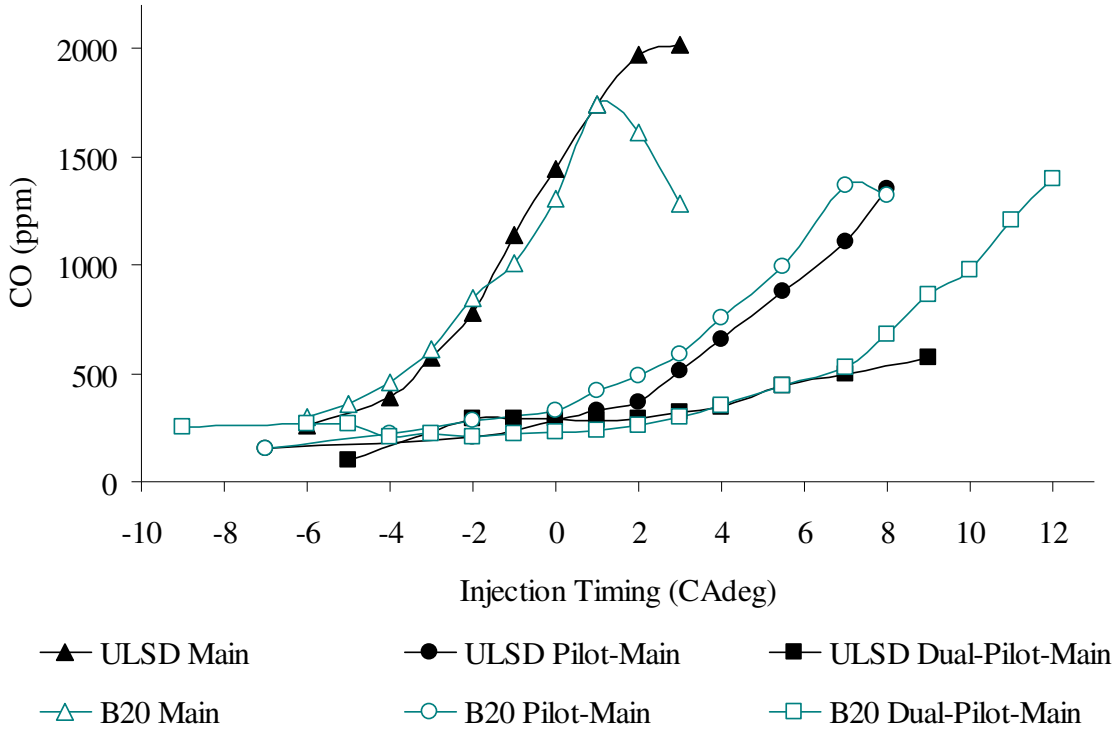

Figure 5.16. Comparison of the injection timing and strategy on CO

NOx Emissions

One strategy of operating in the LNOxC regime is that NOx production will reduce as the timing is retarded. This is seen uniformly in figure 5.16, independent of fuel. An interesting thing to note is that the addition of one pilot lowers the NOx values for both fuels. However the addition of a second pilot increases the NOx values. Comparing the fuel effects, the difference in NOx emissions produced with B20 are insignificant for both the main-only and pilot-main injection strategies. However the addition of a second pilot indicates a 17% increase in the NOx values possibly due to significant increase in premixed burn fraction.

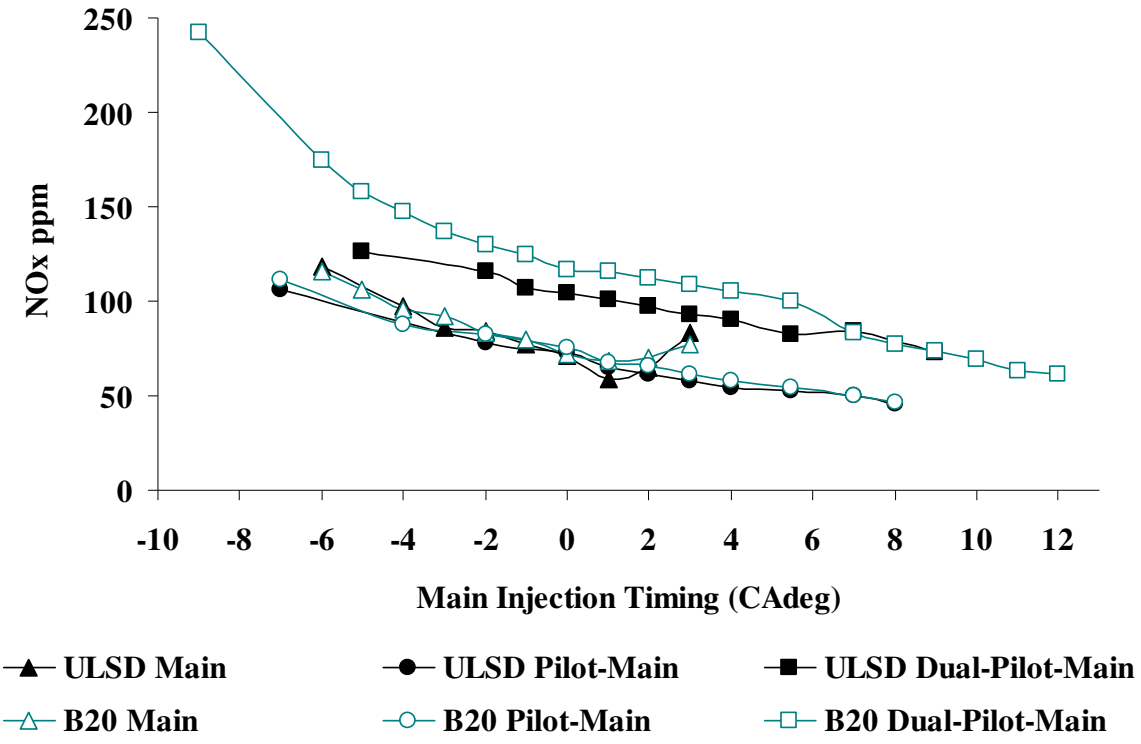

Figure 5.17. Comparison of the injection timing and strategy on NOx

Particulate Matter Emissions

An important characteristic of DPF loading and regeneration is the effect of PM production. Not only is the fuel type important to characterize, but also the combustion regime used. Tests were done to evaluate the amount of soot generated utilizing different injection strategies as well as the fuel effect on these strategies.

As shown in figure 5.18, comparing the effect of advancing and retarding the timing on FSN number shows a reduction in the FSN number as the timing is retarded, a strategy of the LNOxC regime. This trend is seen independent of the fuel used. However, as you compare the FSN numbers fueled with biodiesel, B20 produces a lower FSN number than ULSD for the pilot injection cases. The reduction in FSN is most significant for two pilot injections.

Comparing the different injection strategies, utilizing only a main injection gives the lowest overall FSN. However at engine operating point utilizing only one or two injections gives approximately the same quantity of soot.

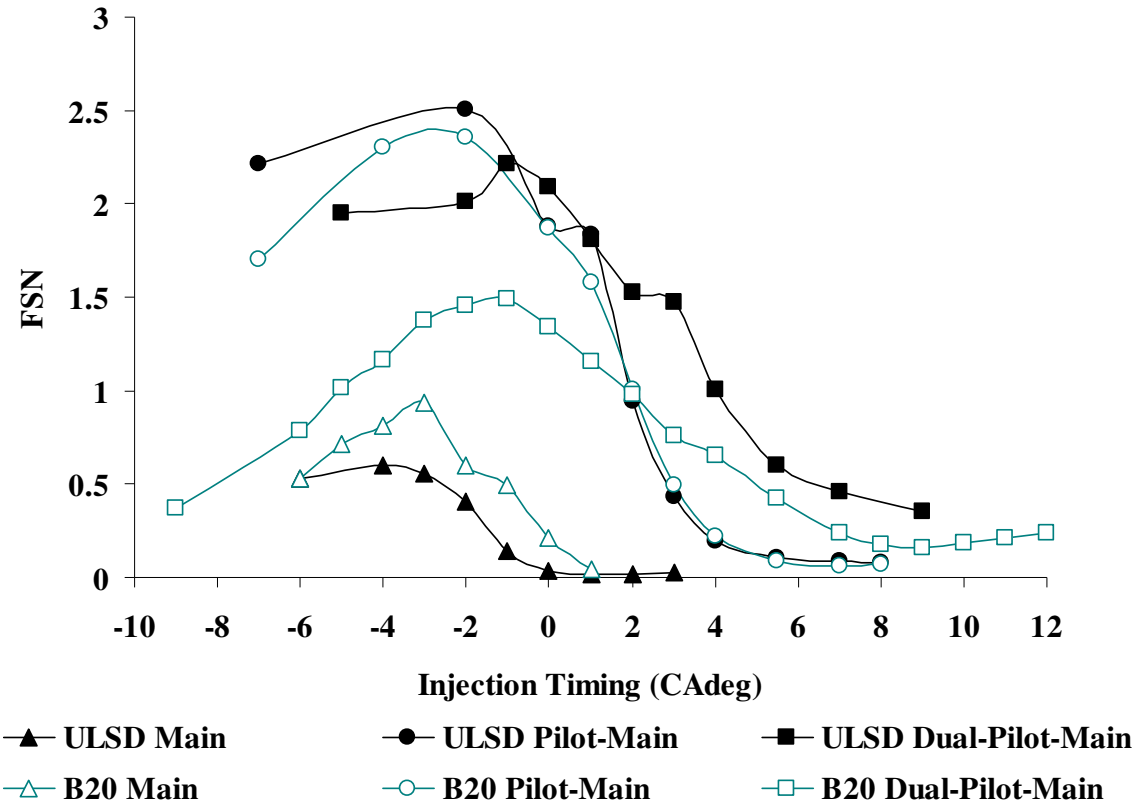

Figure 5.18. Comparison on the injection timing and strategy on PM

Peak Pressure Rise Rate

The engine combustion noise was not physically measured but experimentally the peak cylinder pressure rise rate (PPRR) was measured by the pressure transducers (Kistler) in each cylinder. The cylinder pressure was analyzed using a high speed data acquisition of 25 consecutive cycles averaged over all four cylinders was used to calculate the ARHR (Apparent Rate of Heat Release). Unfortunately data was not taken at all test points due to the peak pressure in-cylinder exceeding manufacturer cylinder design limitations. As expected, calculation of the peak pressure rise indicates that at

the conventional diesel combustion regime the addition of injection events decreases the peak combustion noise in-cylinder. However, the highest combustion noise is noted by advancing the timing. As the timing is retarded the combustion noise is reduced all within acceptable levels regardless of injection strategy. The same work was repeated using B20, however the results did not show a significant difference with the fuel used.

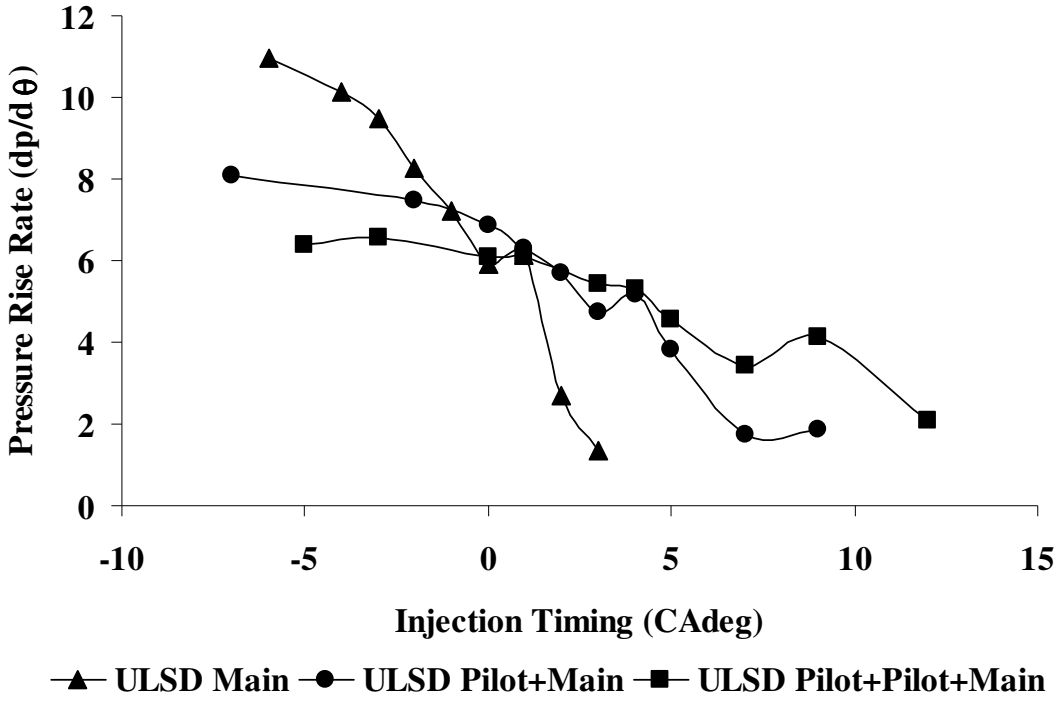

Figure 5.19. Comparison of the pressure rise rate as a function of injection strategy for ULSD

Combustion strategies are extremely important when discussing engine performance and emission characteristics. The following is a summary of findings for the experimental data that has been described above.

- Operating the engine in the LNOxC regime lowers PM and NOx as expected for both ULSD and B20 with a penalty seen for both THC and CO but lower for B20 [53].

- However, it is important to note that replacing B20 without modification to the engine calibration with two pilots will give higher NOx emissions, BSFC, but lower PM.

- Optimizing the engine calibration strategy when fueled with B20 will give lower NOx values with negligible effects to CO and THC as compared to ULSD emissions.

- Results show that operating the engine in the LNOxC regime will produce lower PM and NOx with a slight penalty in fuel consumption.

- Timing sweep data indicates the effect of replacing ULSD with B20 on emissions.

- Due to the low volatile components of B20, optimization of injection timing is critical in engine out emissions reduction.

CHAPTER 6

RESULTS AND DISCUSSION OF UREA-SCR

The following chapter describes the aftertreatment configuration of a Urea-SCR system as well as the testing procedure that is followed. The effect of utilizing long and short divergent sections before the SCR catalyst is explored as well as the effect of B20 fuel on the aftertreatment system.

6.1 Introduction

For NOX reduction, selective catalytic reduction (SCR) has been widely used since 1970s [62]. Several studies have proposed results for plasma type catalyst [63, 64], lean NOX trap (LNT) [65], and urea-SCR [62, 66-69]. A combination of DPF and SCR in one catalyst is also a type of SCRs, although the NOX conversion is only 70 to 85%, as described in [70, 71].

Urea-SCR needs to be used with a urea dosing system. The present study uses a dosing system described in [72]. The system injects a urea solution, named AdBlue, comprising 67.5 wt% water and 32.5 wt% urea into the exhaust pipe. Due to the temperature in the pipe, the spray droplets would experience hydrolysis and thermolysis to work with the SCR and reduce the amount of NOX. A detailed process is mentioned below as well as in [62] and [73].

NOX conversion efficiency through a SCR is typically called deNOX efficiency. The process of NOX reduction starts from the injection of AdBlue into the exhaust pipe.

Once the solution is in the pipe and the exhaust temperature is high enough, the evaporation of the solution will occur and therefore equation (1) presents,

$$CO(NH_2)_2 \text{ (liquid)} \rightarrow CO(NH_2)_2 \text{ (solid)} + x\ H_2O \text{ (gas)} \quad (1)$$

The thermolysis of the solution then occurs into ammonia and isocyanic acid, as in equation (2),

$$CO(NH_2)_2 \rightarrow NH_3 + HNCO \quad (2)$$

Along with the hydrolysis of isocyanic acid shown in equation (3),

$$HNCO + H_2O \rightarrow NH_3 + CO_2 \quad (3)$$

Therefore, the overall AdBlue decomposition could be written as equation (4),

$$CO(NH_2)_2 + H_2O \rightarrow 2NH_3 + CO_2 \quad (4)$$

The ammonia (NH_3) produced from (4) will react with NOX from the exhaust gas inside the SCR catalyst. Several reactions have been proposed as urea-SCR reactions, as shown in equations below.

$$4NH_3 + 4NO + O_2 \rightarrow 4N_2 + H_2O \quad (5)$$

$$4NH_3 + 2NO_2 + 2NO \rightarrow 4N_2 + 6H_2O \quad (6)$$

$$8NH_3 + 6NO_2 \rightarrow 7N_2 + 12H_2O \quad (7)$$

Equation (5), (6), and (7) are known as standard, fast, and slow reactions, respectively. These are also desired reactions that NOX could be converted to N_2.

Nonetheless, some undesired reactions would occur as well. Reference [73] proposes that nitrous oxide might form during the process, as in equation (8),

$$2NH3 + 2O2 \rightarrow N2O + 3H2O \quad (8)$$

This is due to the two stages of thermolysis described in [62]. The second stage is not preferred and causes undesired reactions. The products from those reactions would block the active sites on the catalysts and therefore reduce the deNOX efficiency. Another related study can be seen in [74].

The deNOX process is temperature-dependent and involves the interactions of nitric oxide (NO), nitrogen dioxide (NO_2), and NH_3 mentioned in [66, 67, 75-77]. For urea-SCR, the best working temperature window is from 300 to 400°C along with NO/NO_2 ratio equals to 1. The deNOX efficiency could achieve higher than 90% in this condition. Furthermore, urea-SCR is usually applied with the usage of a diesel oxidation catalyst (DOC) and DPF, which have effects on NO/NOX ratio as described in [73, 78].

In spite of its high efficiency, urea-SCR system also has some disadvantages that many researchers are studying. NH_3 slip is the main focus when urea-SCR is used. In [69, 79, 80] and other literature the NH_3 slip has been studied. Generally, NH_3 slip is due to overdosing of AdBlue and a poor designed SCR entrance shape. The former leads to excess NH_3 for deNOX reactions while the latter causes larger recirculation area in the pipe and therefore poorly distributed spray droplets. Some studies have modeled the in-pipe simulation to demonstrate the recirculation issue [80-82]. In order to improve the distribution and atomization of AdBlue spray, reference [83] studies

different types of mixers placed in front of the SCR entrance and [84] studies the effect of entrance length before the SCR.

6.2 Experimental Setup

A 2.8 liter, 4-cylinder, direct injection diesel engine by VM Motori is used in this research. A common rail fueling system, cooled exhaust gas recirculation (EGR) system, and variable geometry turbocharger (VGT) are also assembled on the engine. The engine set up can be seen below.

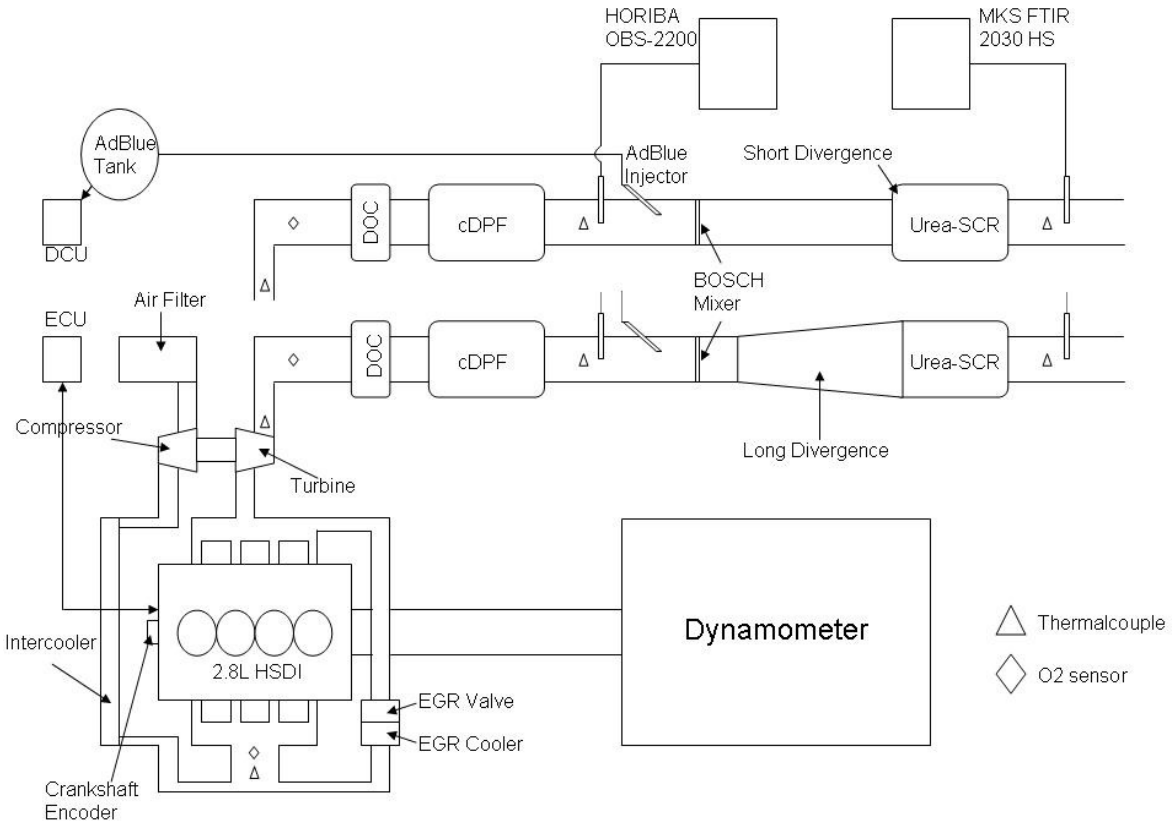

Figure 6.1. The Engine Setup Schematic

As shown in the above figure, a DOC and a catalyzed DPF are placed in front of the urea-SCR. The AdBlue dosing system is positioned after the DPF with a mixer placed between the injector and the SCR. Two types of SCR entrances are also shown in the figure. The specifications of the DOC and DPF are described in [85-87]. The mixer is similar with the one in [83] referred to as a bend wave mixer. This type of mixer has a homogeneous stress distribution which prevents damage of the mixer. A photograph of the mixer used in the current experiment is shown below.

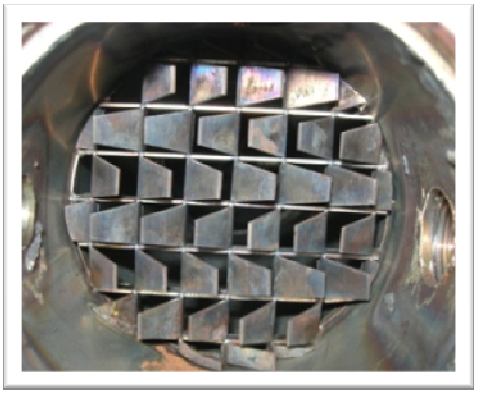

Figure 6.2. Bosch Flap Mixer

The AdBlue dosing system is provided by Bosch. The injector has three holes on it and is fixed at a 30 degree angle on the exhaust pipe wall. This system is the same one used in [72]. Figure 6.3 and 6.4 show the injector nozzle and connection on the pipe respectively.

Figure 6.3. Injector

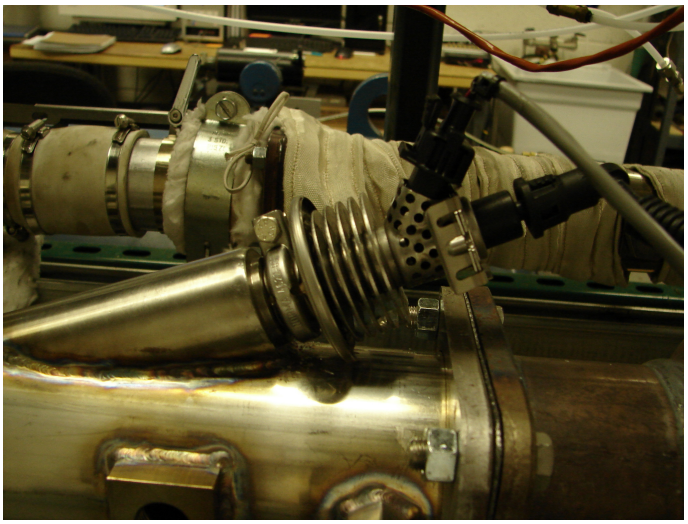

Figure 6.4. Injector Mounted on Exhaust

6.3 Engine Test Points

Four different testing points fueled with ULSD have been chosen in terms of engine speed, power output, exhaust gas temperature, and the amount of NOx

measured after the DPF, as shown in table 6.1. The test points used represent low speed/low load, medium speed/low load, medium speed/medium load, and medium speed/high load as test A, B, C, and D, respectively.

TEST	A	B	C	D
SPEED	1200	1600	1600	1600
BMEP (bar)	3.58	1.97	3.62	8.29
Raw Exhaust T (°C)	264	240	326	450
Before Urea Injector (°C)	230	261	312	408
After SCR T (°C)	212	241	289	384
M_{air} (kg/hr)	61.73	70.85	79.46	123.7
BSFC (g/kW hr)	239.3	347.82	243.91	180.98
A/F Ratio	25.99	27.87	24.33	22.28
Horiba BSNOX x1000 (g/kW hr)	949.4	781.1	586.70	1072.77

Table 6.1. Engine Test Points

Different SCR temperatures are also considered while the testing points are selected. As in table 2, temperatures before and after the urea-SCR have been measured so that in-SCR temperatures are approximately 220, 250, 300, and 400°C for each testing points, respectively. In order to study the temperature effect on the

performance of the SCR, the present study holds the temperature constant, regardless of other engine parameters. This explains some of the discrepancies in the results discussed in the following sections.

Testing Procedure

The current experiment is run under a steady-state condition with each test point repeated three times Two different types of fuels are tested as well as two kinds of urea-SCR divergent sections. The detail of the testing procedures is described below.

1. Regenerating the DPF to burn off all the deposits or particulates (e.g. PM, ammonium nitrate, and etc.) that might affect the testing results. This is done for thirty minutes.

2. Running the engine at first test point. It requires twenty minutes to reach the steady-state condition, namely, the exhaust temperatures before and after the SCR remain fairly constant.

3. Start of emission testing. With the HORIBA OBS-2200 and MKS FTIR HS-2030 on both sides of SCR as shown in figure 6.1, the measurement is taken for another twenty minutes. This could be divided into two steps as:

    a. The first ten minutes is for the stabilization of emission test benches. During this period, the engine combustion and emission data is taken and averaged in order to calculate how much AdBlue is needed for dosing. The detailed calculation is shown in next section, UREA DOSING CALCULATION.

b. The AdBlue dosing is manually controlled and started in the first minute after the first ten-minute period. The designated amount for AdBlue dosing is injected into the exhaust pipe while the measurement is still being taken continuously.

4. Stop testing and repeat from 1 to next testing point.

The period of emission measurement after the start of AdBlue injection depends on the decreasing pace of the amount of NOx. In the present study, the actual time is only ten minutes since the slope of NOx decreasing curve is close to zero in this interval.

Urea Dosing Calculation

The calculation for AdBlue dosing is critical since excess dosing could cause ammonia to slip from the exhaust pipe or ammonium nitrate to deposit on the inner pipe wall. Robert Bosch has proposed two methods to assess the required amount of AdBlue dosing. Both of them are described below:

Standard calculation:

Calculate the exhaust flow rate as equation (9),

$$\dot{m}_{exhaust}\left(\frac{kg}{hr}\right) = \dot{m}_{air}\left(\frac{kg}{hr}\right) + \dot{m}_{fuel}\left(\frac{kg}{hr}\right) \quad (9)$$

Calculate the NOX flow rate as equation (10),

$$\dot{m}_{NO_x}\left(\frac{mg}{\sec}\right) = NO_x(ppm)\times 10^{-6}\left(\frac{\%}{ppm}\right)\times\frac{46}{28.8}\left(\frac{MW_{NO_2}}{MW_{exhaust}}\right)\times\dot{m}_{exhaust}\left(\frac{kg}{hr}\right)\times 10^{6}\left(\frac{mg}{kg}\right)\times\frac{1}{3600}\left(\frac{\sec}{hr}\right) \quad (10)$$

Calculate the AdBlue flow rate as equation (11),

$$\dot{m}_{AdBlue}\left(\frac{mg}{\sec}\right)=\dot{m}_{NO_x}\left(\frac{mg}{\sec}\right)\times\frac{17}{46}\left(\frac{MW_{NH_3}}{MW_{NO_2}}\right)\times\frac{60}{34}\left(\frac{MW_{urea}}{MW_{NH_3}}\right)\times\frac{1}{0.325}\left(\frac{mass_{urea}}{mass_{AdBlue}}\right)$$

(11)

The amount of NO_2 present in the exhaust is functioning as a correction for AdBlue dosing. Due to different chemical reactions for urea-SCR (equation (5) to (7)), the correction factor is necessary for the calculation. As shown in figure (7), the percentage of NO_2 in the amount of NOX measured before the urea-SCR will give different factor numbers.

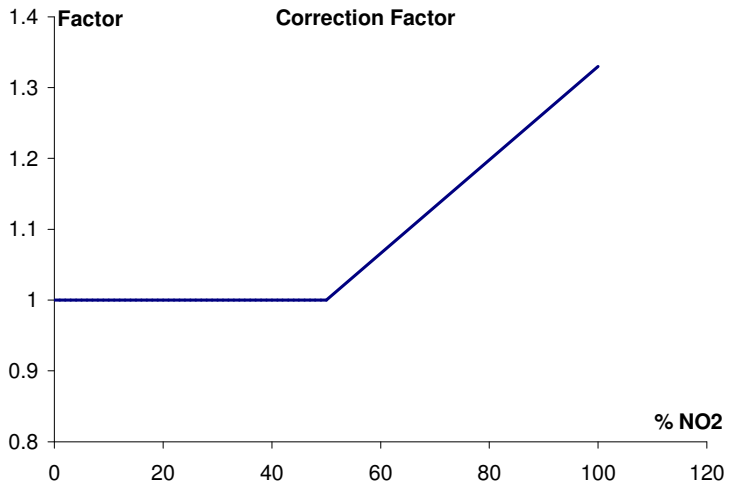

Figure 6.5. Correction Factor Corresponds to NO2%

From equation 4, if the percentage of NO_2 is less than 50%, the factor is equal to 1. The desired amount of AdBlue dosing is the result from equation 3. The calculation requires one further step which is shown in equation 12.

$$\dot{m}_{AdBlue,corrected}\left(\frac{mg}{\sec}\right)=\dot{m}_{AdBlue}\left(\frac{mg}{\sec}\right)\times Factor \quad (12)$$

Fast calculation:

Fast calculation is used to estimate the amount of AdBlue in a simplified manner. From the Standard Calculation step 3, the AdBlue mass flow rate is calculated in equation 13, shown below.

$$\dot{m}_{AdBlue}\left(\frac{mg}{\sec}\right)=\dot{m}_{NO_x}\left(\frac{mg}{\sec}\right)\times 2 \quad (13)$$

For a NO_2 percentage greater than 50%, the correction equation becomes

$$\dot{m}_{AdBlue,corrected}\left(\frac{mg}{\sec}\right)=\left(\dot{m}_{AdBlue}\left(\frac{mg}{\sec}\right)\times\left(\frac{NO_2\%-50\%}{50\%}\right)\times 0.33\right)+\dot{m}_{AdBlue}\left(\frac{mg}{\sec}\right) \quad (14)$$

The present study adopts the fast calculation due to simplicity.

6.4 Results and Discussion

The MKS FTIR HS-2030 measures the exhaust gas from the end of urea-SCR system. The sampling line probe is positioned after the convergent section of the urea-SCR catalyst. Owing to the capability of FTIR test bench, more detailed exhaust gas species are taken and analyzed compared to the HORIBA emission measurement. In the following comments, the results and discussion are primarily focused on NOX-related emission data.

Post-SCR BSNOX

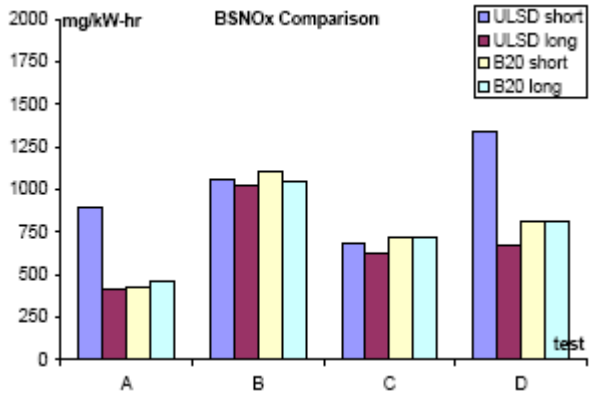

Figure 6.6. NOX Results For All Tests

The NOx results are shown in figure 6.6. Tests with B20 are shown to produce more NOx than those with ULSD, with some of the highest values with ULSD fuel and the short entrance section. However, the present study focuses on maintaining the engine exhaust temperature constant which could explain the discrepancies.

The NOX conversion rate in the following figures shows the results versus in-SCR temperature along with different fuels and divergence sections.

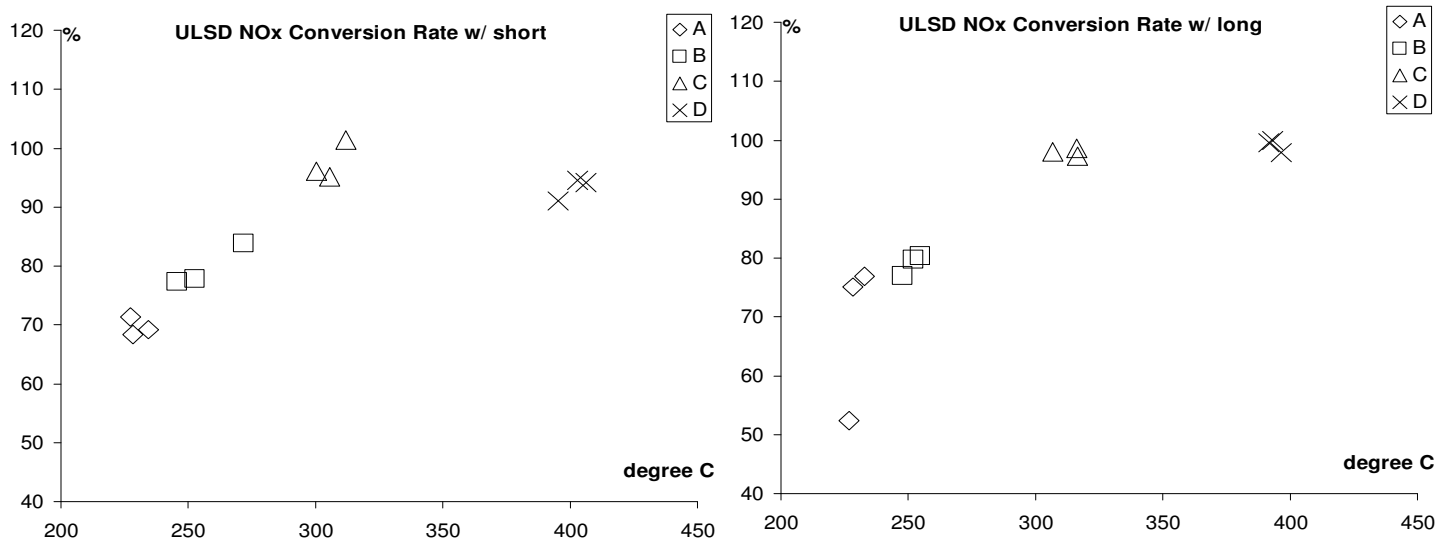

Figure 6.7 NOX Conversion Rate vs temperature with ULSD and short (a: left) and long (b: right) divergence

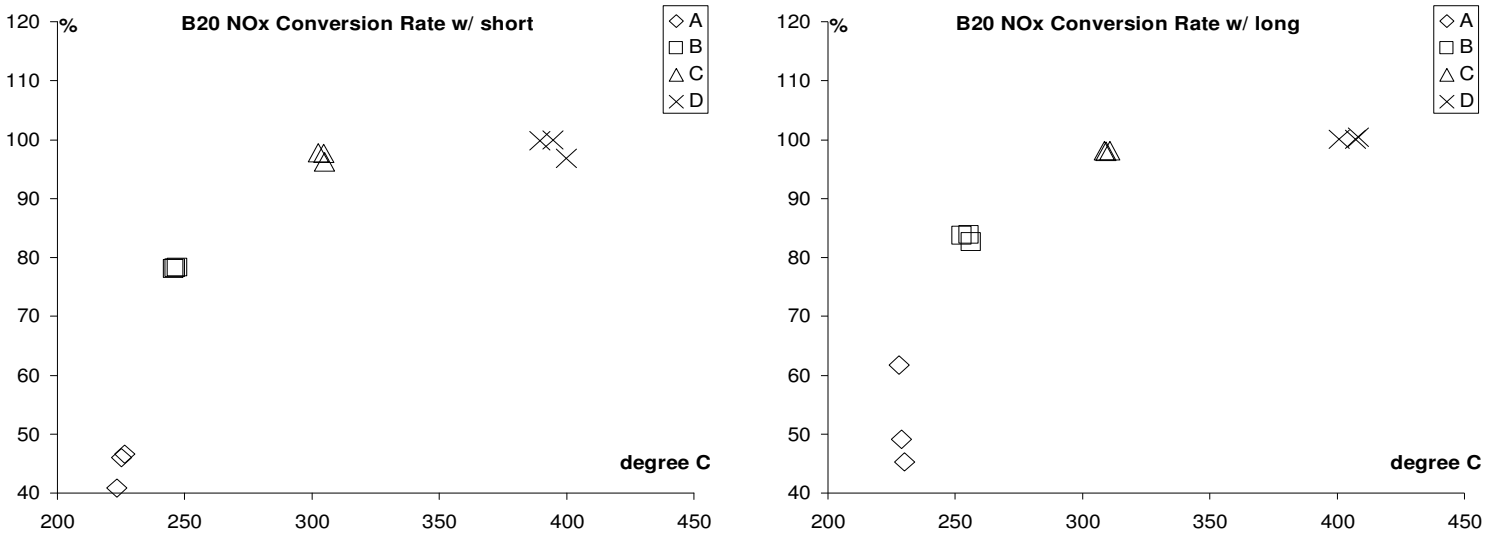

Figure 6.8 NOX Conversion Rate v.s. temperature with B20 and short (a: left) and long (b: right) divergence

It is clear in the above figures that the NOX conversion rate is temperature-dependent. For temperatures from 220 to 300°C, the rate is as low as <50%, as shown

in figure 6.8, to about 100%. The present study does not perform any experiments at 350°C, but it could be assumed that it is 100% at this point, as the trend shows here.

Different kinds of fuels affect the NOX conversion rate specifically at low temperatures. Comparing figure 6.7a with 6.8a, the conversion rate is about 70-75% with ULSD while it is only about 50% with B20. At higher temperatures, the rate is approaching 100%.

The addition of the divergence sections also affects the NOX conversion rate. Figure 6.7b and 6.8b indicate that the longer divergence could improve the conversion rate at low temperatures, comparing figure 6.7a and 6.8a. This could be explained by the smaller recirculation area in longer divergence section, which therefore enhances the AdBlue spray distribution, as discussed in reference [80-82].

Regarding the NO/NO_2 ratio in NOX as the results, figure 6.9 and 6.10 present the stacked column histogram to show the NOX composition with respect to brake specific NO and NO_2. The value has been multiplied by 1000 for legibility.

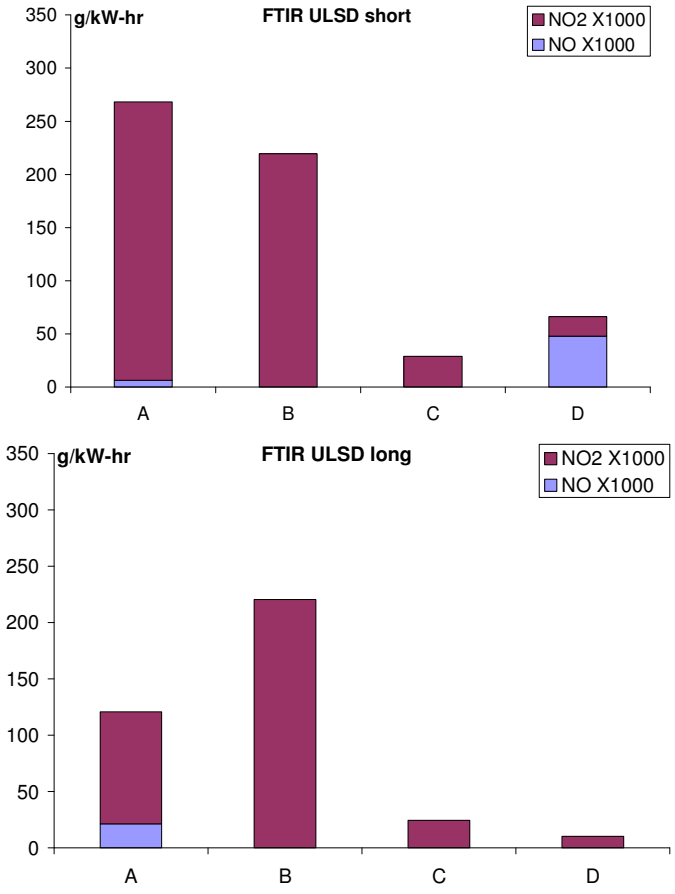

Figure 6.9 NOX composition with ULSD and short (a: top) and long (b: bottom) divergence

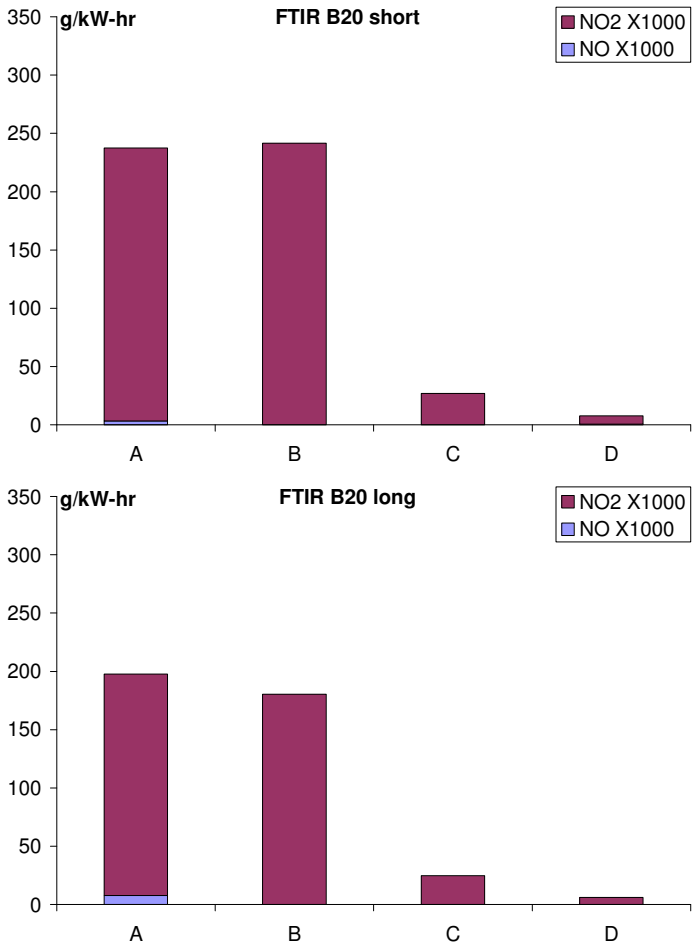

Figure 6.10 NOX composition with B20 and short (a: top) and long (b: bottom) divergence

Considering test D in figure 6.9a as an exception, the data indicates that the amount of NO has greater proportion at low temperature than at high temperature, although it is only a very small fraction of NOX. From figure 6.9 and 6.10, it is apparent that NO_2 is more difficult to eliminate than NO, regardless of the testing temperature.

Post-SCR NH3 Slip

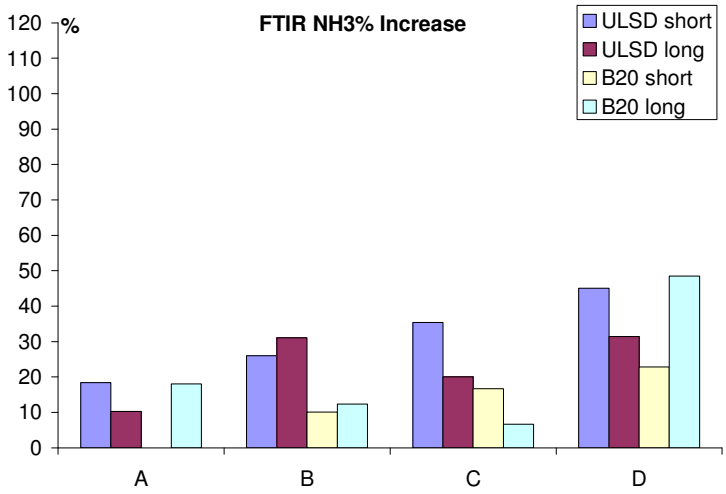

Figure 6.11 NH_3 increase rate

Ammonia (NH_3) slip is a significant concern when urea-SCR system is addressed. The averaged NH_3 increase rate after the urea-SCR is displayed in figure 6.11. As can be seen, NH_3 tends to increase with the temperature at the same engine speed, namely, test B to D. It should be noticed that this is the percentage of how much NH_3 increases, which means that the actual amount of NH_3 could be the same even though the increase rate is different in each tests. Besides test A and D, B20 seems to give less NH_3 slip than ULSD does, although further study is needed.

Post-SCR HNCO Increase Rate

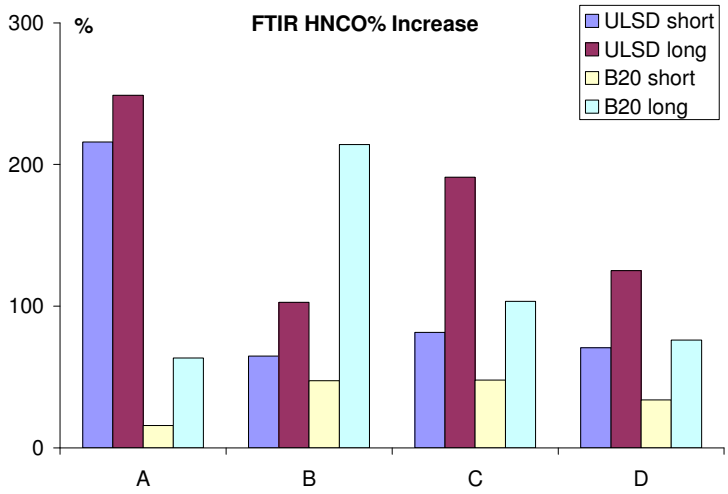

Figure 6.12 HNCO increase rate

HNCO has also been an interest for urea-SCR-related researches, and the averaged HNCO increase rate is shown in figure 6.12. Except for test B, ULSD tends to produce more HNCO than B20, and a longer divergence section has a higher increase rate than the short section. This result could be the advantage of using B20; nevertheless, the longer divergence section presents more HNCO production while better NOX conversion begins to occur.

Post-SCR N2O Increase Rate

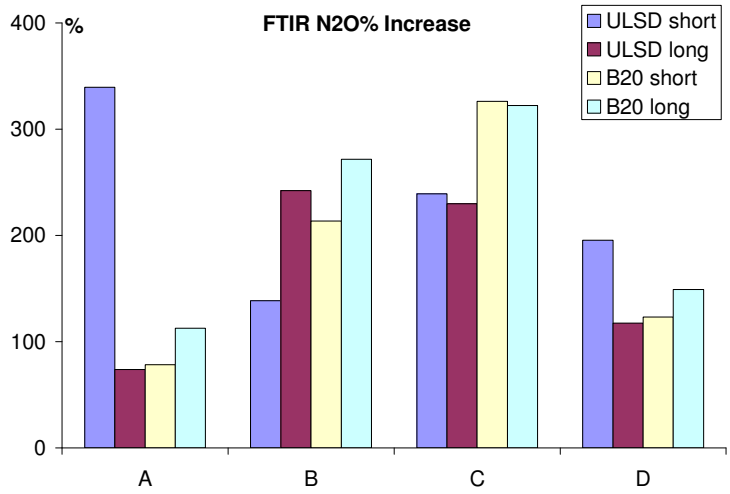

Figure 6.13 N_2O increase rate

Nitrous Oxides are an additional concern of the urea-SCR study. Shown in figure 6.13 is the N_2O increase rate after the urea-SCR catalyst. The N_2O increases throughout all testing points. Detailed real-time data would be shown and discussed in the following section.

NH_3 Mass Conservation

The present study calculates the total NH_3 mass conservation as equation 15,

Total NH_3 injected = NH_3 used for equation 5 + NH_3 used for equation 6 + NH_3 used for equation 7 + NH_3 used for equation 8 + NH_3 slip from the SCR + NH_3 stored inside the SCR 15

Figure 6.14 shows two examples as the results of test A (ULSD, short divergence) and D (B20, long divergence). Under each line is the amount of NH_3

consumed in each reaction, e.g. between the top line and the second one from the top is the amount of NH_3 consumed with fast reaction. The bottom area in each test is the NH_3 storage quantity.

It is clear that the amount of NH_3 adsorbed inside the SCR is greater than that reacted with the NOX. The NH_3 storage quantity is also temperature-dependent in the current experiment, namely, the increase of temperature would decrease the amount of NH_3 stored in the SCR. The involved reactions are different between these two tests, i.e. test A does not have the standard reaction while test D does not contain the slow reaction. Besides, N_2O reaction consumes much more NH_3 than the NH_3 slip, which means the engine in the current experiment emits more N_2O than NH_3 from the exhaust pipe and indicates that N_2O should be considered more than the NH_3 slip while the urea-SCR system is activated.

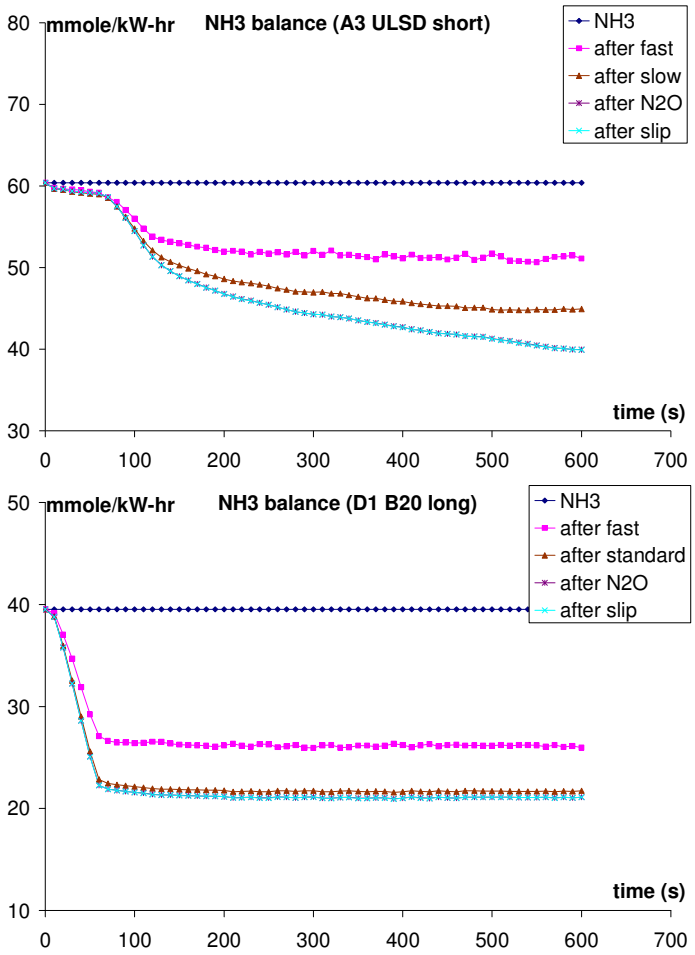

Figure 6.14 NH3 mass conservation with test A (a: top) and D (b: bottom).

The SCR system has been tested for both ULSD and B20 utilizing both a short and long divergent SCR entrance length. The following is a summary of the findings for the experimental data that has been described above.

- At low exhaust temperatures, B20 has lower deNOx efficiency than ULSD while longer SCR entrance lengths may compensate for the low efficiency.
- DOC and catalyzed DPF upstream of SCR affect the NO/NO_2 ratios significantly.

- N_2O emitted from the SCR is more than the NH_3 slip, indicating possible more concern is required for N_2O than the NH_3 slip.
- NO_2 does not convert as easily with NH_3 (convert to N_2) than NO. This is regardless of the exhaust temperature.

CHAPTER 7

SIMULATION ANALYSIS USING GT-POWER

In this chapter, analysis of experimental work is presented using the commercial software GT-Power. The first section is devoted to understanding the software with respect to an explanation of the equations used and assumptions that are made. The remaining sections will provide an analysis of the experimental data for loading and regeneration of a diesel particulate filter using GT-Power.

7.1 Introduction

The commercial code GT-Suite contains pre-processing, simulation (solver) and post-processing applications. Specifically for engine and aftertreatment modeling, GT-Power is used. This solves the 1-dimensional equations to predict the flow rates for both intake and exhaust systems. GT-Power is also able to do in-cylinder modeling of combustion, pressure, heat transfer to cylinders, and work. Basic models are also available to analyze aftertreatment systems i.e. DOC light off and DPF loading and regeneration applications. The whole system is designed in GT-Power and then discretized into many small sub-volumes, connected by boundaries. The flow solution is calculated by simultaneously solving the continuity, energy, and momentum equation at each time step. The mass and energy equations are solved in sub-volumes and the momentum equation is solved at the boundaries. The solution is not an iterative numerical process, as in a CFD simulation, but is based on the state of the system at time zero and calculated for new time one.

7.2 GT-Power DPF Modeling Overview

The function of a diesel particulate filter is to “catch” the small particles that are created during combustion in the exhaust gas and deposit them on the pores of the clean filter. The larger particles will land on the outer surface of the particulate filter. As the filter continues to load, the pore size will shrink (fill with small particles of soot) because of the embedded soot. As the pore size shrinks, the filtration of the particulate filter changes from deep bed filtration to cake build up. Furthermore, the permeability of the soot cake depends on the soot morphology. For example, a wet soot cake will have a higher back pressure than a dry loose layer of soot; therefore affecting the loading time of the filter and regeneration time. The following figure is a schematic of the pressure drop through the diesel particulate filter.

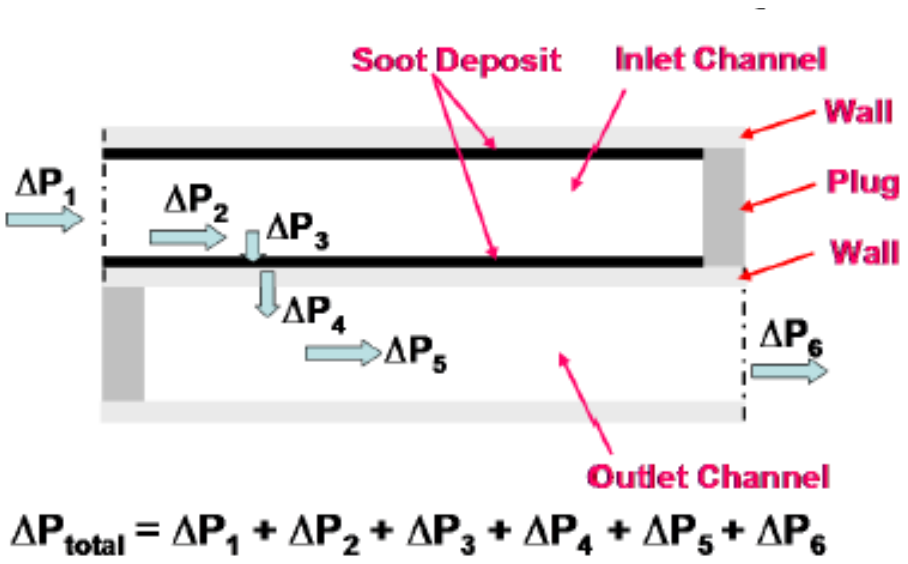

Figure 7.1 Schematic of pressure drop[88]

Where,

ΔP1 = Pressure drop due to contraction

ΔP2 = Pressure drop due to friction in the inlet channel

ΔP3 = Pressure drop due to through soot cake layer

ΔP4 = Pressure drop due to through filter wall

ΔP5 = Pressure drop due to friction in the outlet channel

ΔP6 = Pressure drop due to expansion

The schematic shown in figure 7.2 depicts the measurements of the cell wall thickness as well as the soot layer thickness needed to calculate the total pressure drop through the particulate filter.

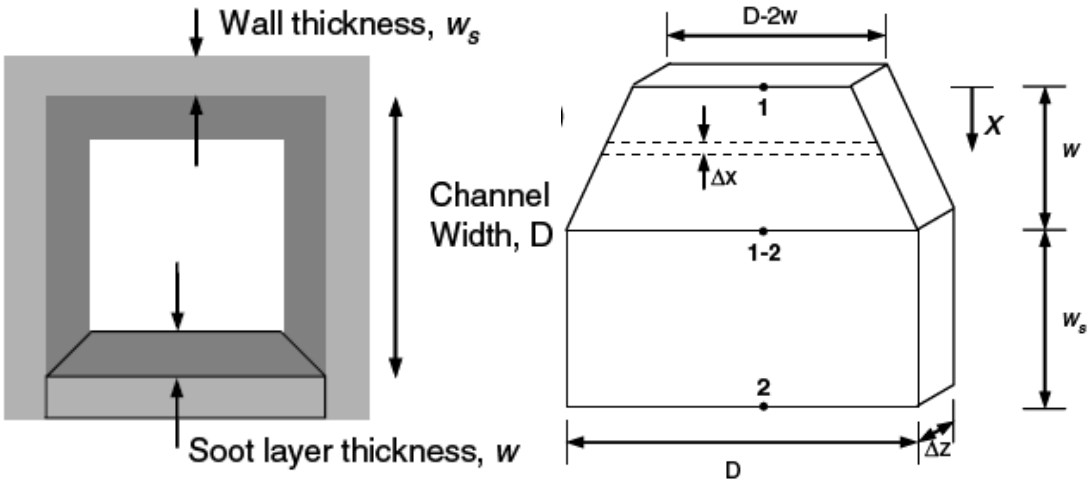

Figure 7.2 Schematic of catalyst individual cell geometry[88]

The pressure drop calculation for the contraction and outlet cell is shown below.

$$\Delta P_2 + \Delta P_5 = \frac{\mu Q}{2V_{trap}}(D + w)\left\{\frac{4FL^2}{3} ln\left(\frac{w}{(D - 2w_s)^4} + \frac{1}{D^4}\right)\right\}$$

[1]

Where,

F = Channel pressure drop correlation for laminar flow

μ = viscosity of wall flow

V_{trap} = total DPF volume

w = soot layer thickness

L = channel length

Q = volumetric flow rate

D = outlet channel width

w_s = substrate wall layer thickness

The pressure drop through the soot layer and wall layer are shown in the following equations.

Soot Layer:

$$\Delta P_3 = \mu\, u_{w1}(D - 2w)\frac{1}{2k_p}\ln\left(\frac{D}{D - 2w}\right) + \beta\rho\, {u_{w1}}^2 w$$

[2]

Wall Layer:

$$\Delta P_4 = \mu \, u_{w2} \sum \frac{w_s(i)}{k_s(i)} + \beta_s \rho {u_{w2}}^2 w_s$$

[3]

Where,

u_{w1} = soot layer inlet velocity

K_p = soot layer permeability

β= soot layer Forchheimer Constant

β_s = substrate wall Forchheimer Constant

u_{w2} = substrate wall velocity

k_s = substrate wall permeability

7.2.1 Calibration of the Model

The GT-Power model is developed using attributes obtained from the catalyzed diesel particulate filter (cDPF) provided by Delphi Corporation. The DPF is a catalyzed silicon carbide (SiC) wall flow type diesel particulate filter. The filter is sized at four liters with a diameter of 5.66 inches and length of 10 inches. The cDPF has a cell density of 200 cells/in^2. Additional properties are shown in the following table.

Attribute	cDPF
Trap Diameter (mm)	152.4
Channel Length (mm)	203.2
Channel Width (mm)	0.7396
Wall Thickness (mm)	0.31
Number of Inlet Channels	4212
Filter Porosity	0.54
Pore Diameter (mm)	0.0125
*Bulk Density (kg/m^3)	760
*Specific Heat (J/kg K)	1000
*Conductivity (W/m K)	2.0

Table 7.1 DPF specifications for simulations

Calibration of the model is required to develop accurate simulation results. To develop the model, the Forchheimer Constant, $\beta s,w$ which models the quadratic effects and the wall permeability, Ks which models the linear effects of the measured pressure drop are determined. The following values were used for the simulation: $\beta s,w = 3E9\ m^{-1}$ and $Ks = 3.958E\text{-}7\ mm^2$. This establishes the "clean" pressure drop through the cDPF. Once these values were obtained, the filter loading is then calibrated against the

experimental data. Filter loading is used to calibrate the total amount of soot accumulated on the DPF, specifically, the soot cake layer and the deep bed filtration. The following figure depicts a typical deep bed filtration and development of the soot cake layer.

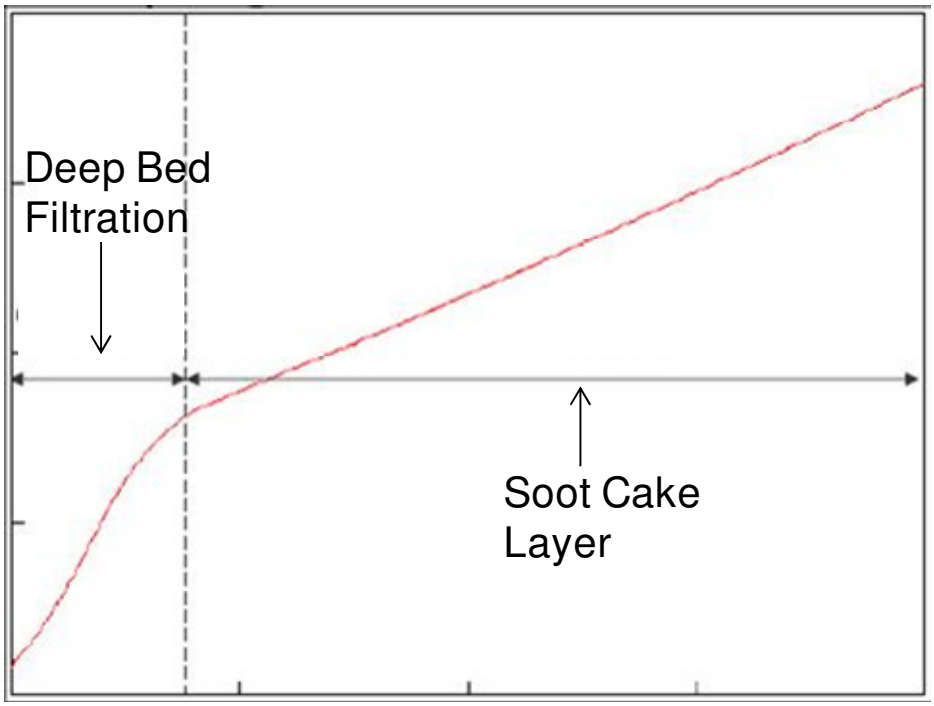

Figure 7.3 Typical schematic of filter loading

As the exhaust gas passes through the filter, soot will deposit on the pores of the filter. The larger particles will land on the surface of the filter, with the smaller particles filling in the pores. As the filter continues to load, the pore size will shrink due to the embedded soot. As the pore size shrinks, the filtration changes from deep bed filtration to cake build up, which is depicted in the following figure.

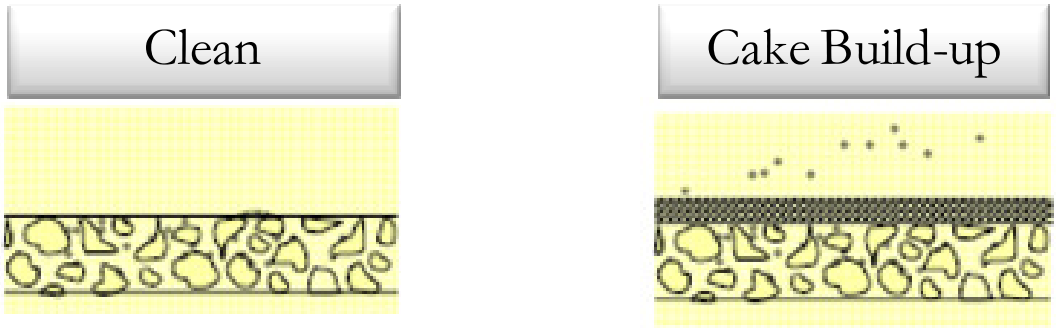

Figure 7.4 Schematic of clean and cake built-up soot

The permeability of the soot cake layer depends on the soot morphology. For example, a wet soot cake will have higher back pressure in the DPF as compared to a dry loose layer of soot. To calibrate the DPF soot filter loading, the percolation constant, ψ and the partition coefficient, ϕ need to be determined. The percolation constant is a dimensionless constant used to calculate the partition coefficient which is shown in the following equation. The partition coefficient determines the amount of particulate matter that will be deposited on top of the filter wall, thereby forming the soot cake layer.

$$\Phi = \frac{d_{c,1}^2 - d_{c,0}^2}{(\psi b)^2 - d_{c,0}^2} \qquad [4]$$

The partition coefficient of the filter loading is modeled by the spherical unit collector concept described below.

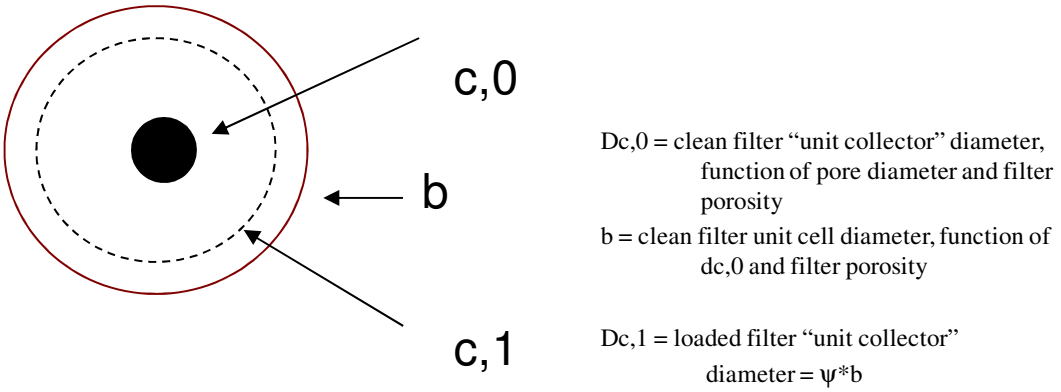

Figure 7.5 Schematic of spherical unit collector concept

Where the percolation constant $\psi = 0.918$ is obtained from literature.

7.3 Results and Discussion

The following figure shows the graphical interface of the GT-Power simulation used to calculate the loading and regeneration of the diesel particulate filter. The simulation is used to verify the experimental results that were found in chapter 4 for loading and regeneration for both ULSD and B20 fuels. All physical data of the experimental system is used to define the GT-Power simulation.

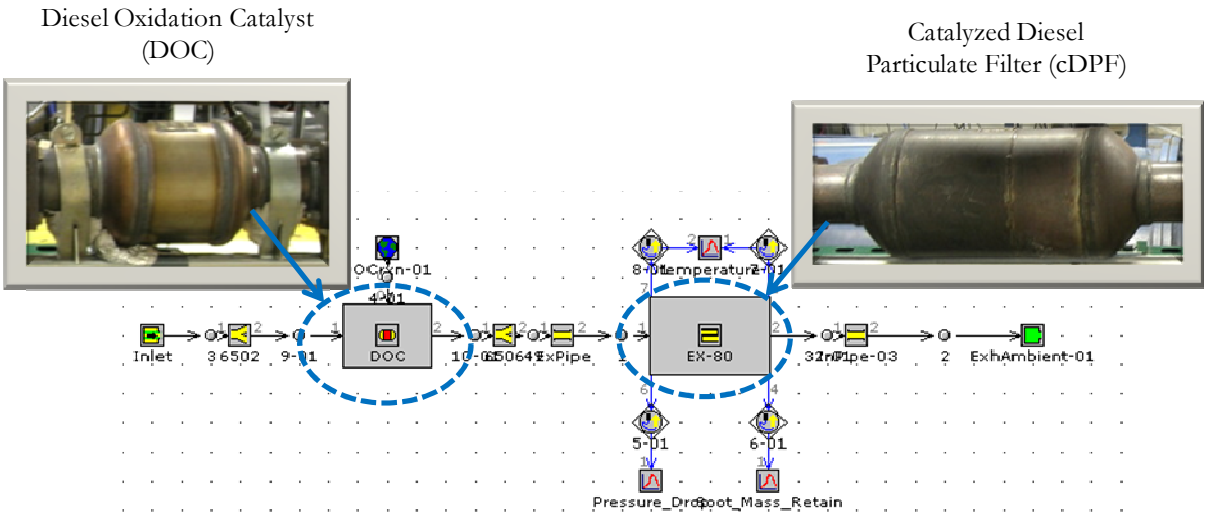

Figure 7.6 GT-Power simulation schematic

The following figure shows the results of the GT-Power simulation in the form of the pressure drop. All physical data of the experimental system is used to define the GT-Power simulation which can be referenced in chapter 4. Experiments were conducted to understand how to repeatedly load the cDPF with the same amount of particulate, and how to quantify that amount. For this experiment, the 4L cDPF is loaded to approximately 5g/L or 60% of typical engine use loading levels. Due to B20 accumulating soot at a lower rate than ULSD, an experimental loading curve was developed to attain 20g of soot. This was then simulated using GT-power and can be seen in figure 7.6. Very good agreement can be seen between the simulation and experimental data. Figure 7.8 shows the actual soot in grams that is retained during the loading period of the cDPF. The experimental soot loading time with B20 gives a 26% increase in time compared to ULSD. For the simulation results, the soot loading time for B20 indicates an increase in soot loading time of 29% compared to the ULSD loading time.

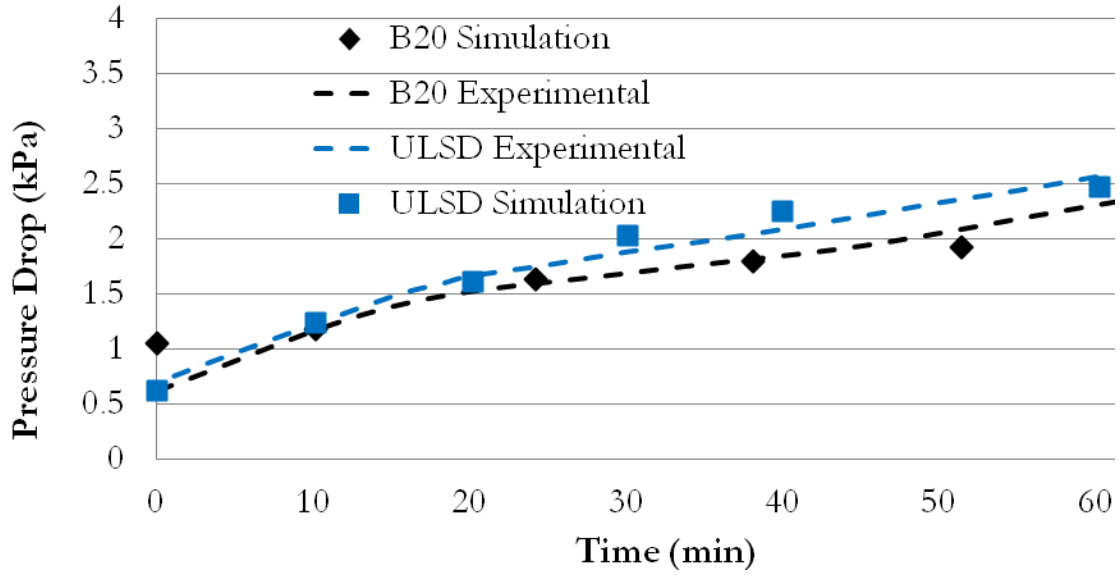

Figure 7.7 Comparison of the pressure drop through the cDPF

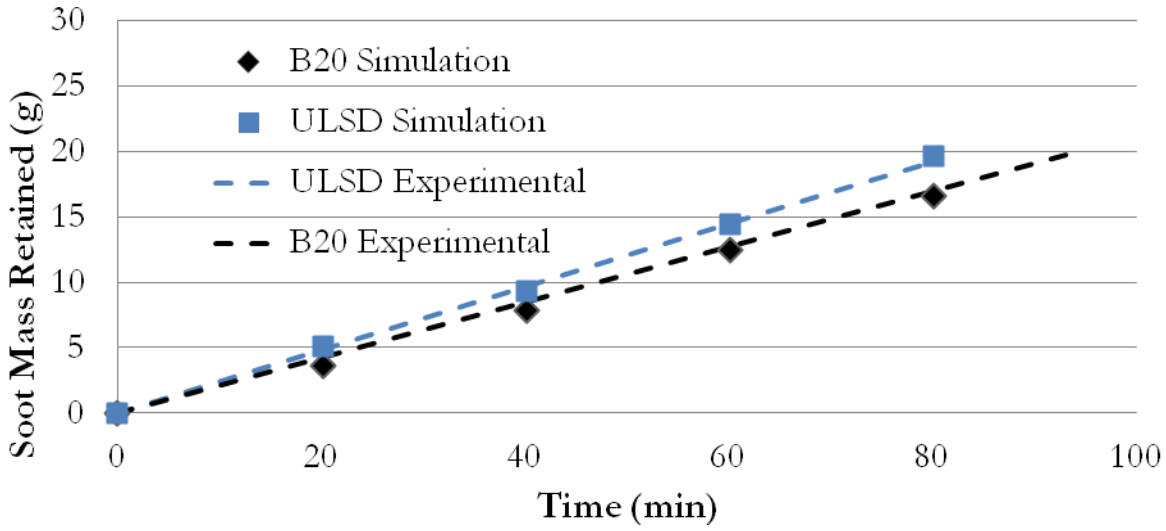

Figure 7.8 Comparison of the soot mass retained during loading of the cDPF

To further analyze the experimental results, a simulation of the regeneration of the cDPF is done. The experimental testing procedure is described in detail in chapter 4

to determine the brake-even temperature. This is defined as the cDPF inlet temperature at which the rate of soot particle oxidation approximately equals the soot particle collection. This temperature is of interest due to soot loaded with B20 and ULSD would have different brake-even temperatures and would therefore start regeneration of the cDPF at different temperatures. The following testing point was used to evaluate the pressure drop and temperature at which regeneration begins.

Test	Speed (rpm)	Load (ft lb)	Post injection Quantity (mm3/cyc)
LSR	1200	80	2

Table 7.2 Low speed regeneration for brake-even temperature testing

For the regeneration simulation, the cDPF was preloaded with 5 gram/liter of soot as shown in figure 7.8 above. The regeneration model was employed within the cDPF or EX-80 simulation object. The simulation results for the pressure drop and brake-even temperature are shown in the following figures for ULSD and B20 regeneration.

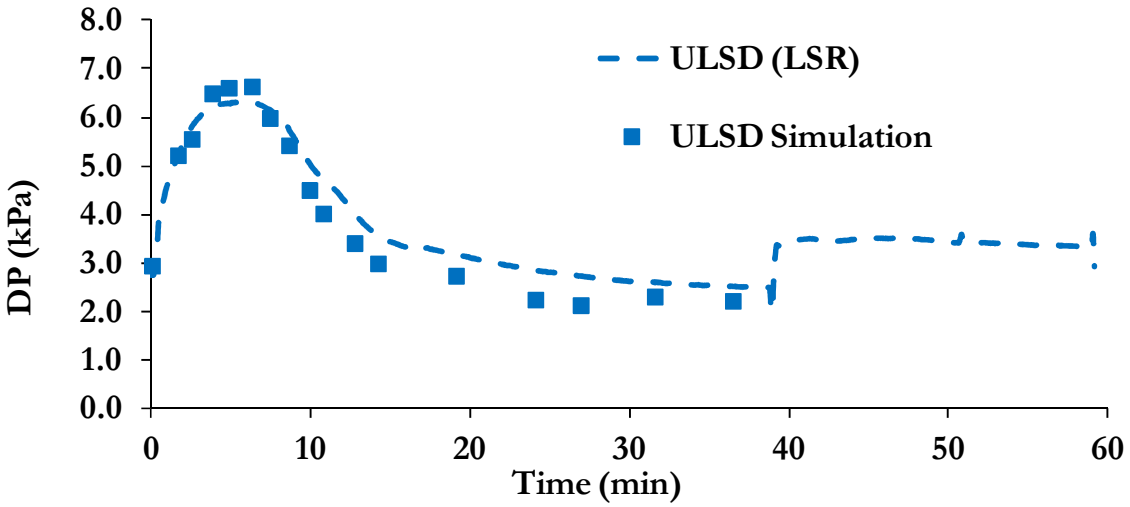

Figure 7.9 Simulation regeneration results for ULSD

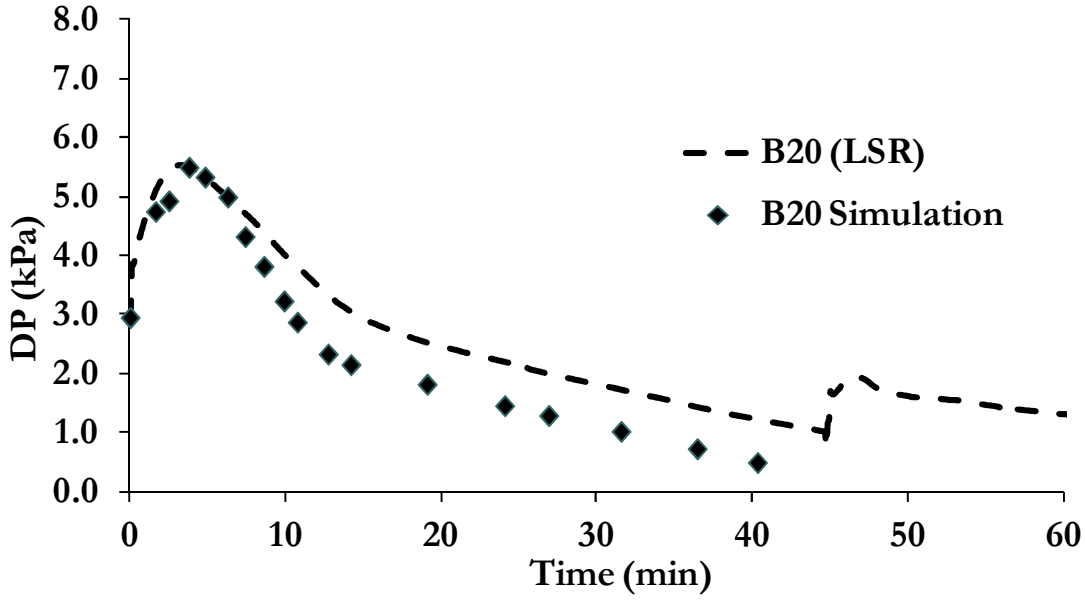

Figure 7.10 Simulation regeneration results for B20

Very good agreement can be seen between the experimental and simulation results. However, the pressure drop for the simulation shows a slightly quicker regeneration than the experimental results. This is due to the calculation of the pressure drop in GT-Power. This could be improved by increasing the loss coefficients within the catalyst. It can also be noted that the regeneration for B20 is slightly faster for the simulation than the experimental results. This is due to the soot model for B20. Exact measurement of the oxygen available in the soot was not done with B20, therefore the availability of oxygen is determined through literature. Furthermore, the break-even temperature for B20 and ULSD is found to be consistently higher compared to the experimental data. The simulation results indicate a break-even temperature for B20 about 81°C lower than soot loaded with ULSD which began to regenerate at about 579°C. This result was higher than the experimental data and could be refined with a more accurate experimental soot analysis.

7.3.1 GT-Power Model and Validation

In order to validate the model, a comparison of the pressure drop versus the soot loaded was compared. Research by Young focused on the experimental data of SiC DPF's. The data was collected on 150mm filters with different cell density and wall thicknesses. The following table contains further details on the DPF's tested.

Property	A1-SiC	A2-SiC	A3-SiC	B-SiC	C-SiC
CTE ($x10^{-7}/^{o}C$)	45	45	45	45	43
Porosity (volume %)	43	42	42	41	56
Mean Pore Size (μ)	29	12	12	8	9
Permeability (10^{-12} m^2)	2.1	1.4	1.3	0.3	0.8
Thermal Conductivity (W/m K)	> 15	> 15	> 15	>15	>10

Table 7.3 Properties of a SiC diesel particulate filter

Clean and loaded pressure drops were measured on four different samples with geometry 5.66”x6”. Both structured and monolith ceramic filters were tested which are shown in figure 7.11.

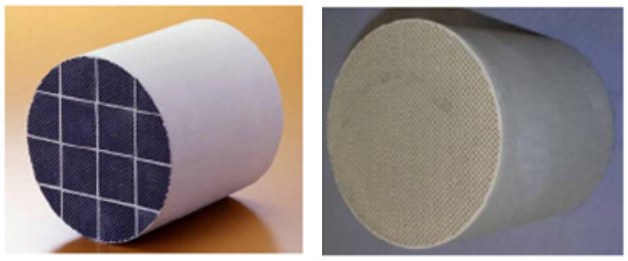

Figure 7.11 Image of structured and monolith DPF

The filters were then loaded with artificial soot. This was done by aerating the fine powder into an airstream of 76 m^3/hr. The soot was loaded to a specific amount each

time, weighed and then the pressure drop across the DPF was measured. The following figure shows the results of their work including the validation of the simulation model. The figure shows the dependence of the pressure drop on the cell density as well as the effect of segmentation of the catalyst filter. Furthermore, the GT-Power model is verified showing the pressure drop of loading ULSD soot onto the DPF. The model is a segmented filter with 200cpsi and is shown to have very good agreement with Young's experimental work.

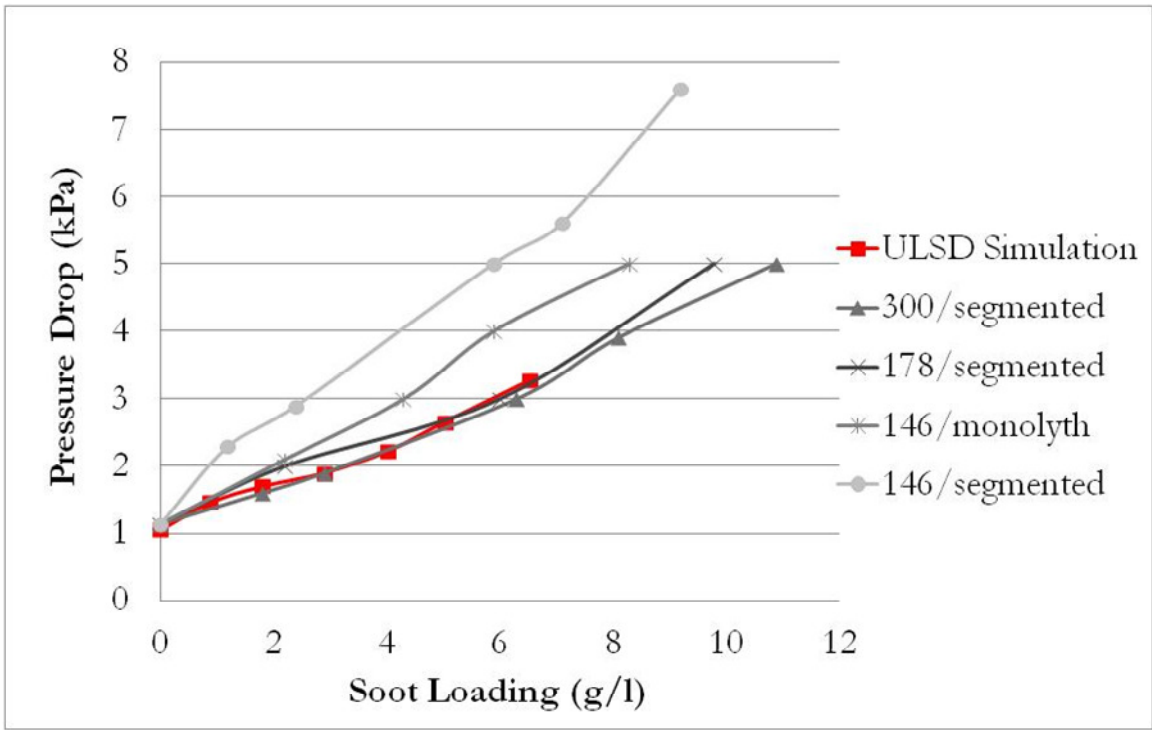

Figure 7.12 Comparison of pressure drop for soot loading [89]

7.4 Engine Combustion

The GT-Power simulation schematic of the 2.8L four-cylinder diesel engine utilized in the experimental results is shown in figure 7.13. All components are analyzed including the EGR, EGR cooler and turbocharger. The simulation results will focus on emissions data, in-cylinder temperatures and ARHRR. The results will then be compared against the experimental data from chapter 5. Table 7.4 shows the test condition used to validate the engine combustion simulation for the 2.8L four cylinder diesel engine. Using the complete engine simulation in GT-Power, emissions data will be collected and compared to experimental engine testing. The purpose of the complete engine testing is done to obtain the emissions data at different testing points to utilize in the aftertreatment simulation. Table 7.5 shows the experimental data obtained during engine testing.

Test	Speed (rpm)	BMEP (bar)	EGR (%)	SOMI (deg)	TbDPF (C)	Mass Flow Rate (kg/hr)
1	1200	3	32	1 bTDC	290	3.726

Table 7.4 Testing procedure

Emissions	Quantity
CO (vol%)	0.0009133
CO2 (vol%)	8.657
THC (ppm)	27.38
NOx (ppm)	75.68
NO (ppm)	55.11
H2O (vol%)	9.059
CH4 (ppm)	4.14
C3H6 (ppm)	0
Diesel (ppm)	15

Table 7.5 Experimental emissions before the cDPF

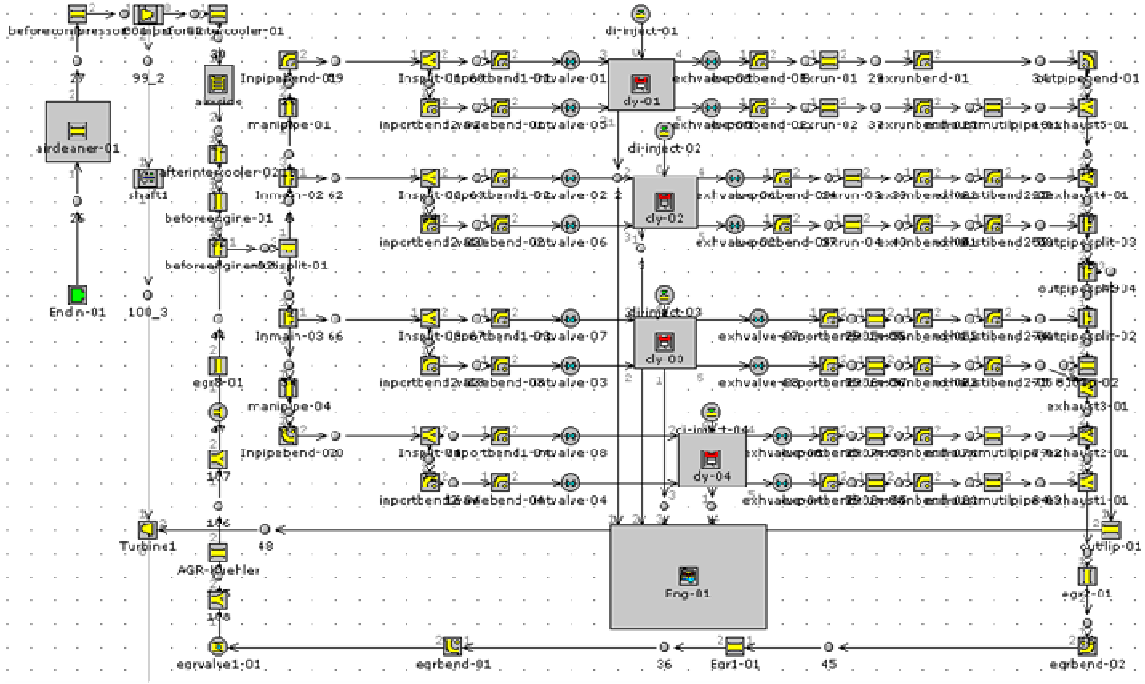

Figure 7.13 Schematic of complete engine simulation using GT-Power

The following schematic is an example of the default GT-Power exhaust products that are calculated during the engine simulation. NOx and CO are calculated by equilibrium with the option of using the kinetic extended Zeldovich mechanism for NO. THC is a function of combustion efficiency and PM or soot is a qualitative prediction using the DI model.

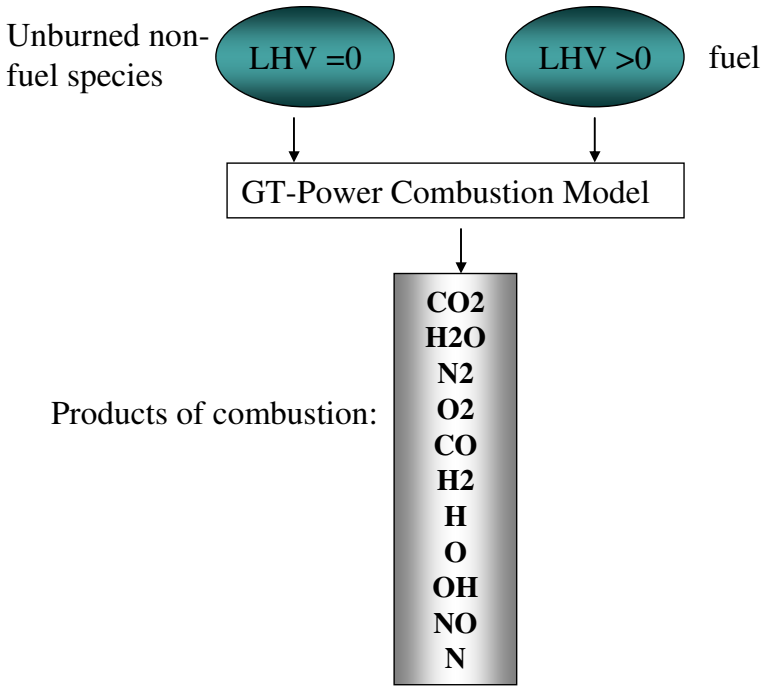

Figure 7.14 Schematic of GT-Power calculation of emissions data

Furthermore, imposed measured exhaust products can be manually entered to account for the emissions that are not calculated. GT-Power calculation of emissions is done using a SPECIESSAMPLER control component and is shown in the following figure. The component senses the outlet species and creates an output file that records species concentration, temperature, pressure, and mass flow rate.

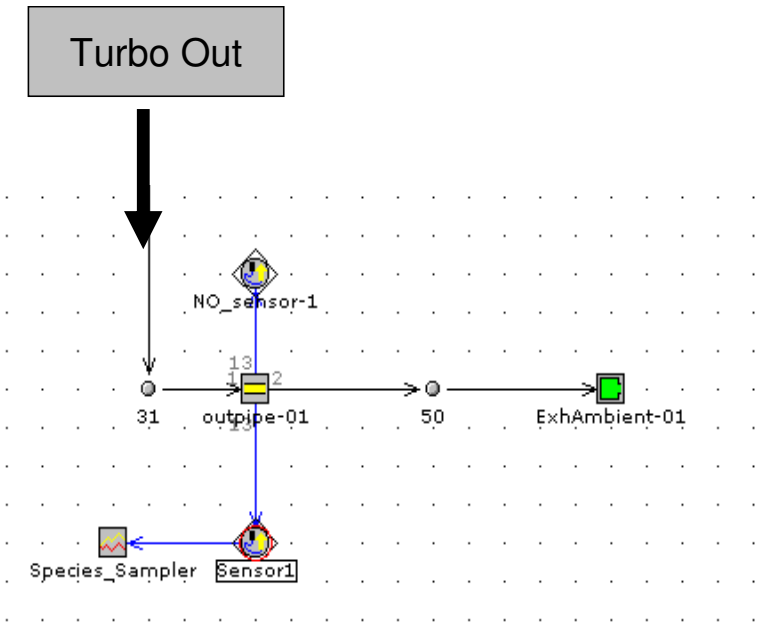

Figure 7.15 Schematic of species sampler in GT-Power

Figure 7.15 shows the engine out exhaust pipe which is open to the atmosphere. The species sampler is connected directly to the exhaust pipe to measure the emission concentrations after the turbocharger. The following figure shows the experimental emissions for both ULSD and B20 before the cDPF. These results were used to validate the complete engine combustion model described above. However, results obtained from GT-Power were not conclusive. Tremendous knowledge of each piece in the engine is needed which is difficult to obtain. This led to numerous errors and inclusive results from the simulation model of the engine combustion. Further study is needed to finalize and obtain useful results of the engine combustion model.

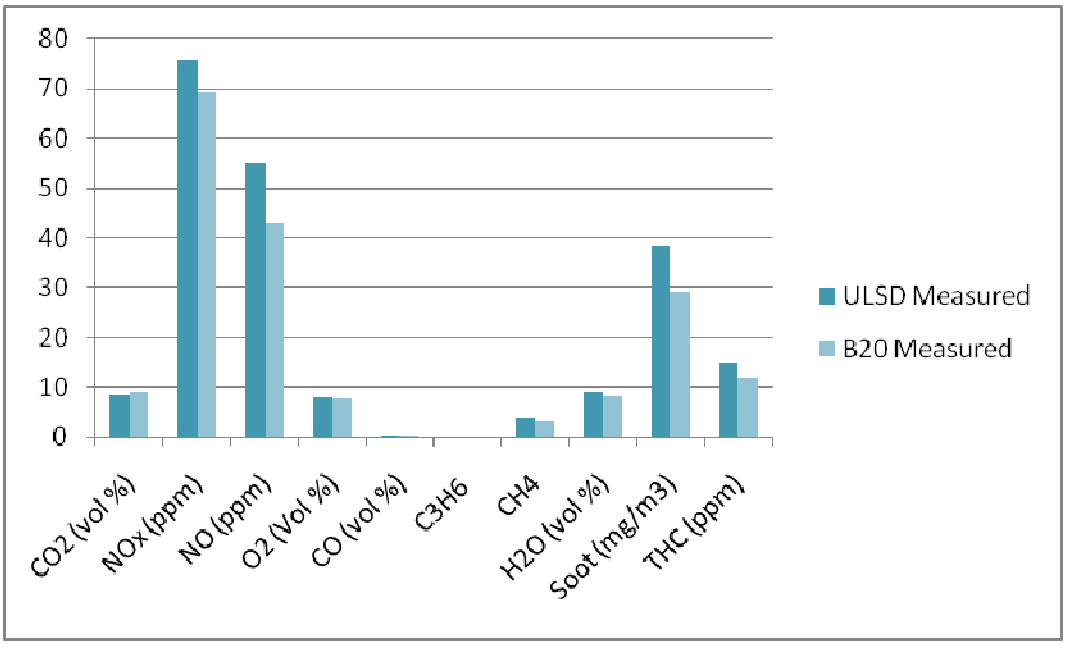

Figure 7.16 Experimental emissions for ULSD and B20 before the cDPF

The following is a summary of findings for the simulation work that has been described above.

- The simulation shows very good agreement compared to the experimental soot loading data. The simulation results show an increase in soot loading time for B20 of 29% compared to a 25% increase experimentally.

- A simulation has been done to model the DPF regeneration rate. The simulation pressure drop shows a slightly quicker regeneration than the experimental results. This is due to the calculation of the pressure drop in GT-Power. An increase in the loss coefficients within the catalyst could improve the result.

- Regeneration for B20 is slightly faster for the simulation than the experimental results. This is due to the soot model for B20, a complete soot analysis would provide more accurate simulation results.

- The break-even temperature for B20 and ULSD is found to be consistently higher compared to the experimental data. The simulation results indicate a break-even temperature for B20 about 81°C lower than soot loaded with ULSD which began to regenerate at about 579°C. The model could be further refined with a detailed experimental soot analysis of all the species present in the soot.

- A complete engine simulation was completed to evaluate the exhaust emissions. The results were inconclusive. Further analysis and study is required to develop a working model.

CHAPTER 8

CONCLUSIONS AND RECOMMENDATIONS

The purpose of this work was to investigate the implementation of biodiesel fuel (B20) in a multi-cylinder light duty diesel engine. The engine is equipped with a range of emission aftertreatment systems including a diesel oxidation catalyst, a catalyzed diesel particulate filter, and a Urea-Selective catalytic reductant catalyst. In addition, the engine is heavily instrumented to analyze and modify engine combustion and the effect that these modifications have on emissions and combustion when fueled with B20. The following chapter will discuss conclusions as well as recommendations based on testing with aftertreatment systems, engine combustion, and computer simulation.

8.1 The Emissions Aftertreatment Systems and Simulation

1. B20 has a reduction in engine out soot which correlated to an increased cDPF loading time by 21% to attain the target loading weight of 20 grams.

2. The lower PM produced with B20 will increase the amount of time it takes to load the DPF, thereby reducing the number of regenerations required and increasing the overall life expectancy of a cDPF.

3. The temperature at which regeneration occurred was reduced by 63℃ compared to the soot loaded with ULSD.

4. Comparison of the speciation results showed that the oxygenated species, formaldehyde and acetaldehyde, were found to be higher for B20 than ULSD. This was attributed to the additional oxygen that is found in B20.

5. Both water and carbon dioxide showed a sharp increase in concentration after the cDPF indicating that products produced after the DOC with B20 are more reactive than ULSD products.

6. NOx data showed a minimal increase with the use of B20 fuel over the regeneration event.

7. The speciation data confirmed that additional oxygenated species are present and/or more reactive with B20 possibly aiding in the faster regeneration rate of soot loaded with biodiesel.

8. Severe degradation of the engine oil was found after three hours of post injection measuring 12.9% biodiesel diluted in the engine oil and a 26% drop in engine oil viscosity.

9. An onboard viscosity oil sensor provided by Delphi Corporation was tested. The sensor was in good agreement with the viscosity bench test analysis and provided oil viscosity measurement over the course of the project.

10. Evaporation or flow back of the fuel to the combustion chamber from the engine oil was shown. B20 has less of a recovery during normal engine operation leaving more fuel in the engine oil compared to ULSD. This will lead to faster deterioration of the engine oil when B20 is used. This was attributed to the lower volatility components that are found in biodiesel.

11. Operation with B20 shows significant fuel dilution and needs to be monitored to prevent engine deterioration.

8.2 Engine Combustion

1. Operating the engine in the LNOxC regime lowers PM and NOx as expected for both ULSD and B20 with a penalty seen for both THC and CO but lower for B20 [53].

2. However, it is important to note that replacing B20 without modification to the engine calibration with two pilots will give higher NOx emissions, BSFC, but lower PM.

3. Optimizing the engine calibration strategy when fueled with B20 will give lower NOx values with negligible effects to CO and THC as compared to ULSD emissions.

4. Results show that operating the engine in the LNOxC regime will produce lower PM and NOx with a slight penalty in fuel consumption.

5. Timing sweep data indicates the effect of replacing ULSD with B20 on emissions.

6. Due to the low volatile components of B20, optimization of injection timing is critical in engine out emissions reduction.

8.3 Urea-SCR Analysis

A urea-SCR system has been tested along with two types of fuels and SCR entrance. The results have been mentioned and discussed in previous sections. The conclusions will be presented below.

1. Soybean-based biodiesel does not show an increase pre-SCR in NOX emission.
2. DOC and catalyzed DPF affect the NO/NO_2 ratio in the present experiment significantly.
3. DeNOX efficiency could reach as close as 100% at temperature range from 300 to 400°C.
4. B20 has less deNOX efficiency at low temperature than ULSD does.
5. Longer divergence section tends to improve deNOX efficiency at low temperature for both fuels.
6. The temperature dependency has greater influence on SCR performance than NO/NO_2 ratio does.
7. Emitted N_2O from the exhaust pipe is more than the NH_3 slip. Therefore, the measurement of N_2O may be of more importance than the NH_3 slip.

8.4 Recommendations

To further enhance our understanding of using biodiesel fuel in a multi-cylinder engine, the following recommendations would be useful to augment the work that has been completed.

1. Tests should be conducted to further analyze the soot produced during the loading of the DPF. The addition of a dilution tunnel as well as a particle analyzer would add significant data to current tests.

2. Due to the severe fuel oil dilution shown during the active regeneration of a DPF with biodiesel, an increase in oil changes is required.

3. The addition of spray simulation would advance the application of Urea-SCR testing and aid in the increase of NOx reduction. Especially during lower temperature and lower engine load test points.

4. Testing should be conducted using B100, as well as multiple biodiesel feedstocks.

5. Additional modification and fine tuning of the complete engine model in GT-Power would model emissions with more accuracy.

APPENDIX A: FUEL REFORMER AND UREA-SCR

The experimental data are carried out with a light duty 2.8L diesel engine coupled with a DOC, cDPF and Urea-SCR emission control devices. The following work will correlate these results with numerical data to establish a more descriptive and complete analysis of the effect of using B20 and ULSD fuel on these systems. The following chapter will discuss the utilization of the multi-dimensional commercial code FLUENT to analyze the injection of urea before the catalyst with different entrance geometries and correlate previous work involving a swirler venturi mixer.

Introduction

Fluent is a powerful commercial code which has the ability to model fluid flow, spray injection, and heat transfer in complex geometries. The creation of the geometry and meshing is done within the software Gambit. The grid is then read into Fluent, with all remaining operations performed within the solver. These include setting the boundary conditions, defining the fluid properties, executing the solver and viewing and post-processing the results.

The Swirler Venturi Mixer

The following work discusses the swirler venturi mixer (SVM) and comparison of the Urea-SCR system. The SVM has been used successfully to generate lean, premixed and vaporized liquid fuel/air mixtures for low NOx combustor applications [90-93]. The

venturi serves to maximize the air velocity at the point of injection to better utilize aerodynamic breakup of liquid sprays to minimize the pressure loss. The swirler is used to shorten the venture length by preventing flow separation inside the venturi. Combination of the swirler and venturi serves to enhance and control the radial mixing without a recirculation zone for hot spots or flashback. The SVM, followed by a catalyst, is an excellent candidate in the liquid fuel reformer and urea-SCR applications.

The compactness of the fuel reformer total volume is usually very desirable, especially in aeronautical applications, and therefore requires special attention. The total length and consequently, the length of the diffuser and the compactness of the inlet manifold in which steam and air comes in, are important parameters to be optimized. The following figure shows the four geometries studied: (a) an ideal coaxial premixed inlet on the top of the SVM with minimal pressure loss, (b) a premixed traverse inlet, (c) a tangential injection of steam and air similar to a cyclonic mixer [94] and (d) impinging inlets of air and steam [95, 96]. Figure A1 shows the four swirlers that were used in the parametric study as well. Experimental results were also conducted with the tangential injection geometry; further description of this work is found in the AIAA paper 2005-0551 [97].

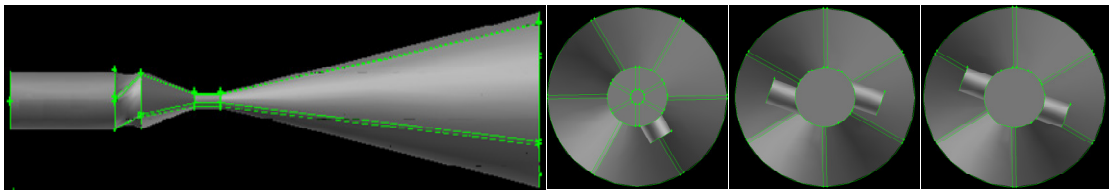

(a) (b) (c) (d)

Figure A1. (a) Ideal coaxial premixed (side view), (b) Premixed traverse injection (top view), (c) Tangential injection, (d) Impinging injection

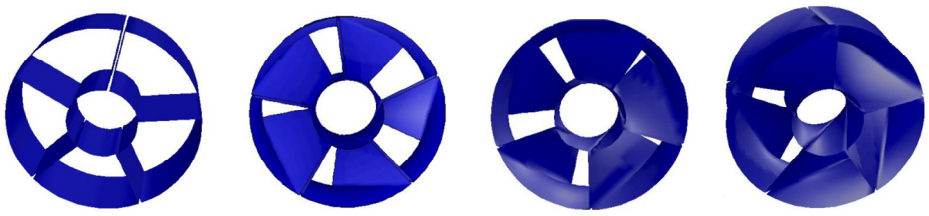

(a) (b) (c) (d)

Figure A2. Geometry of four swirlers (a) blank, (b) 30 deg, (c) 45 deg, (d) 60 deg

In order to examine the evolution of the momentum transfer within the SVM, the following axial, radial and swirl (angular) momentum fluxes, and the Swirl Number (SN) are defined, similar to previous study at various cross-sections along the SCM axis [94, 98].

Axial Momentum Flux: $G_z = \int_A \rho |V_n| U_z dA$

Radial Momentum Flux: $G_r = \int_A \rho |V_n| U_r dA$

Angular Momentum Flux: $G_\theta = \int_A \rho |V_n| U_\theta . r dA$

Swirl Number (or Ratio): $S_N = \frac{G_\theta}{rG_z}$

The simulated swirl number evolution and the turbulence kinetic energy at the centerline are shown in figure A3 for a premixed coaxial SVM without consideration of the presence of catalytic reactor to better correlate with laboratory visualization tests. The swirl number reaches a maximum at the beginning and drop inside the contraction section due to increased viscous dissipation. Higher swirl number was generated by larger swirl vane angle, as expected. The turbulence intensity at the centerline drops slightly at the convergence section due to vortex stretching, but increases dramatically at the throat section, and reaches a maximal value later at the early part of the divergence section. This indicates the critical function of the throat is not only to help break up the spray but also enhance the fuel-air mixing in SVM. The turbulence variation, however, does not seem to be sensitive to the swirl angle change.

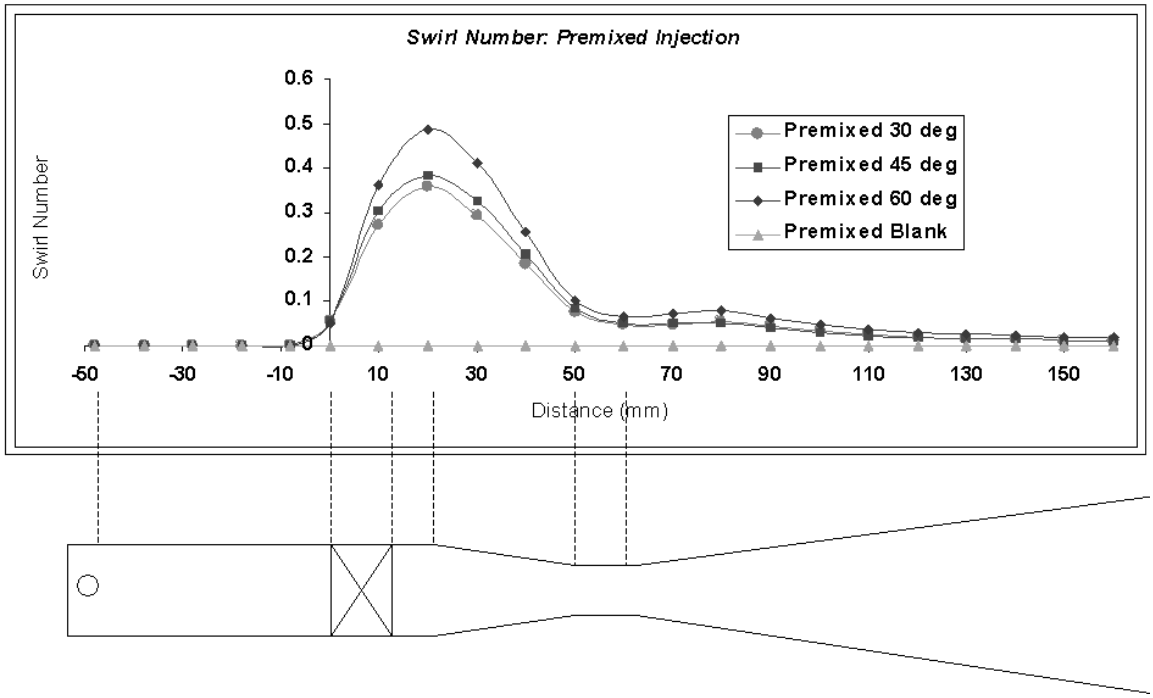

(a)

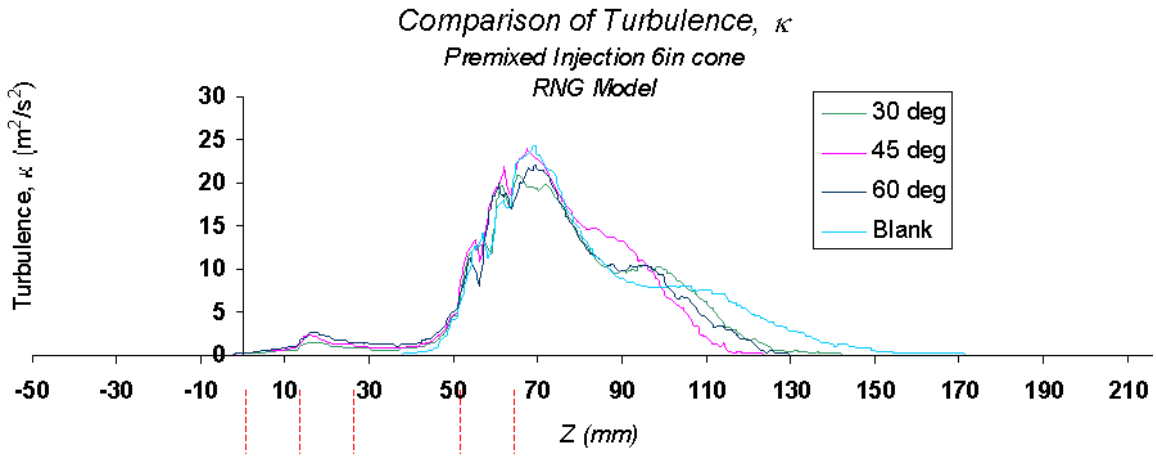

(b)

Figure A3. (a) Swirl number and (b) centerline turbulence kinetic energy distributions in a SVM.

The swirl number profile for the four inlet geometries is shown in the following figure for the 30 degree swirler case. The swirl number of the tangential injection is much larger than the others in the beginning, as expected. Although the swirl number is much larger than desired, it is shown to be reduced or rectified by the 30° swirler. The impinging injection which has zero offset distance shows similar swirl number behavior as the premixed cases. Too strong a swirl not only creates unnecessary wall wetting of spray inside the SVM, but also increases the pressure drop as shown in figure A4.

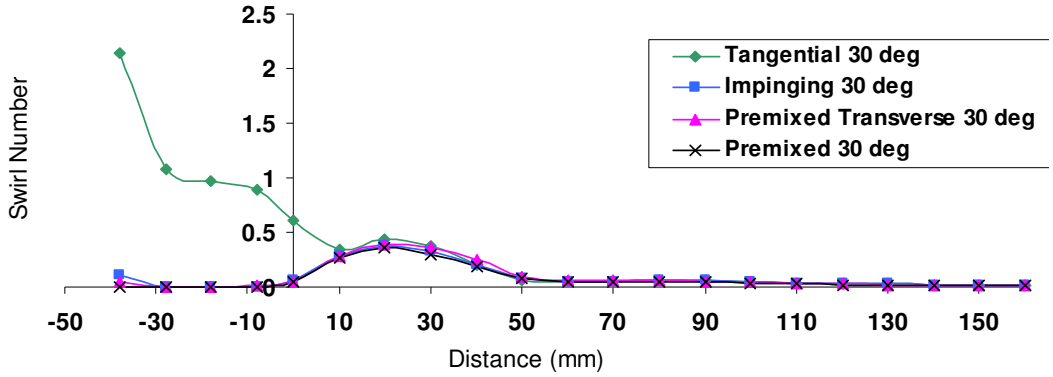

Figure A4. Swirl number distribution inside the SVM for different geometries

Figure A5 shows the pressure distributions of different inlet geometries. The figure shows that the non-premixed cases (tangential and impinging injection) have much higher pressure drops compared to the premixed cases. In this figure, the premixed cases with single inlets were computed with the mass-averaged properties of the air and steam, while the non-premixed inlet cases use the cold flow properties. The tangential injection wasted pressure head to set up stronger swirling flow than needed. The impinging injection also lost pressure head in viscous dissipation. The axial swirlers

are more efficient and have lower pressure-loss in generating the swirl for the Venturi tube.

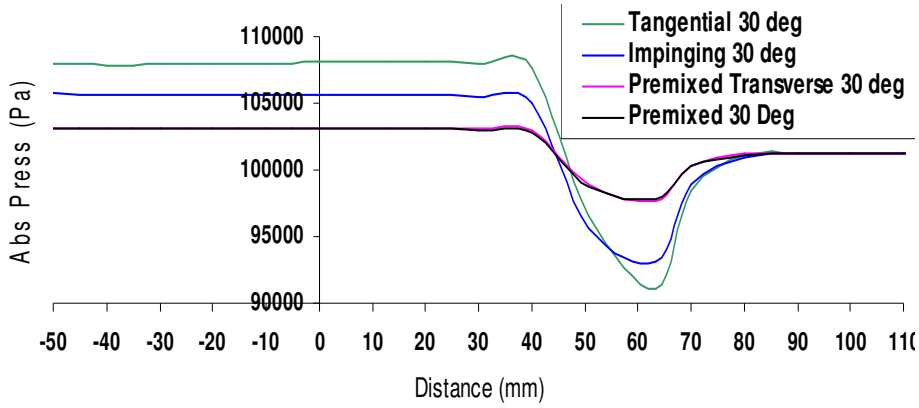

Figure A5. Axial pressure distribution along the centerline of SVM with different inlet geometry

The uniformity of the flow distribution at the exit of SVM exit without the catalytic reactor section is shown in the following figure for a tangential injection geometry. It is obvious that the velocity is not uniform due to the strong tangential flow of the air jets which persist past the swirler and is still visible as a helical pattern at the SVM downstream. The 60 degree swirler case manages to produce a more uniform flow which is away from the wall.

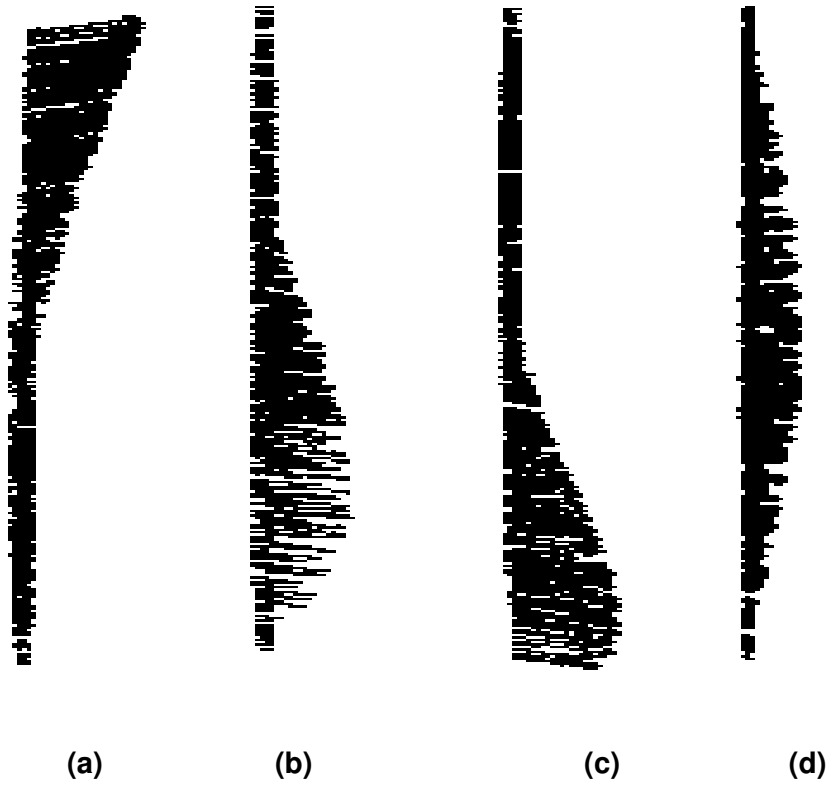

Figure A6. Simulated velocity vector plots at the exit of SVM for tangential injection inlet:

(a) blank or no swirler, (b) 30^{o} swirler, (c) 45^{o} swirler, (d) 60^{o} swirler.

The SVM geometry, although simple in construction, is not easily optimized. Previous simulation was successful in predicting the drop sizes using the simple aerodynamic breakup model without the coalescence model [92]. A detailed CFD and experimental study carried out on the diffuser-monolith flow showed that the SIMPLE-based scheme with standard k-e turbulence model cannot predict the separation and pressure recovery of the simple conical diffuser flow. However, improved turbulent

models such as renormalized group model (RNG), improve the accuracy of the prediction [98].

Spray Visualization of Swirler Venturi Mixer

In order to see the effect of tangential injection inlet on SVM, a cold flow spray visualization experiments is carried out similar to previous studies [92, 93, 99]. The flow rate of the gas is controlled by a pressure regulator and is monitored by an Omega flow computer. Water at room temperature is continuously injected into the high-speed airstreams at the Venturi throat through a capillary tube having a 0.3-mm inner diameter. The flow rate of the water is controlled by a Dynamax SD-200 precision liquid pump system and is displayed on a monitor. A pulse Copper laser operated at 3 kHz with light sheet forming cylindrical lens is used as the light source. A 35-mm still camera (Nikon FM2) was used to record the image, with a fixed exposure time of 8ms. A two-channel PDPA (Aerometrics) was used to measure droplet size, velocity, and volume flux of the water spray.

The spray structure characterized by the multiple exposure laser light-sheet illumination is shown in figure A7. The spray visualization shows significant wall wetting and asymmetric spray for the helical swirling flow, which originated from tangential injection inlet. Without a swirler to reduce the swirl intensity, figure A7(d) shows more significant wall wetting and a core void of spray droplet compared to the cases with a swirler. The Sauter mean diameter (SMD) distributions of the droplet size measured by PDPA measurements at 20 mm from exit of diffuser are also shown in figure A8. The longer 6-inch Venturi causes more wall wetting and produces slightly larger drop size

than the shorter 4-inch one, except for the case without a swirler which produced smaller droplets at the center, although at a significant lower number density. The tangential injection inlet has a compact design, but with the penalty of higher pressure drop and the potential of inferior flow uniformity. Therefore, for the reformer mixing simulation only the ideal premixed coaxial inlet is presented for the parametric study.

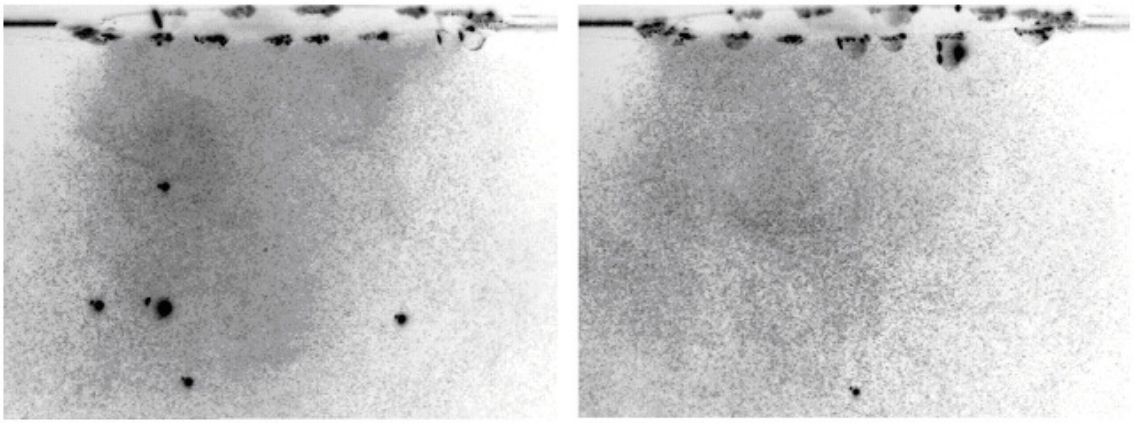

(a) (b)

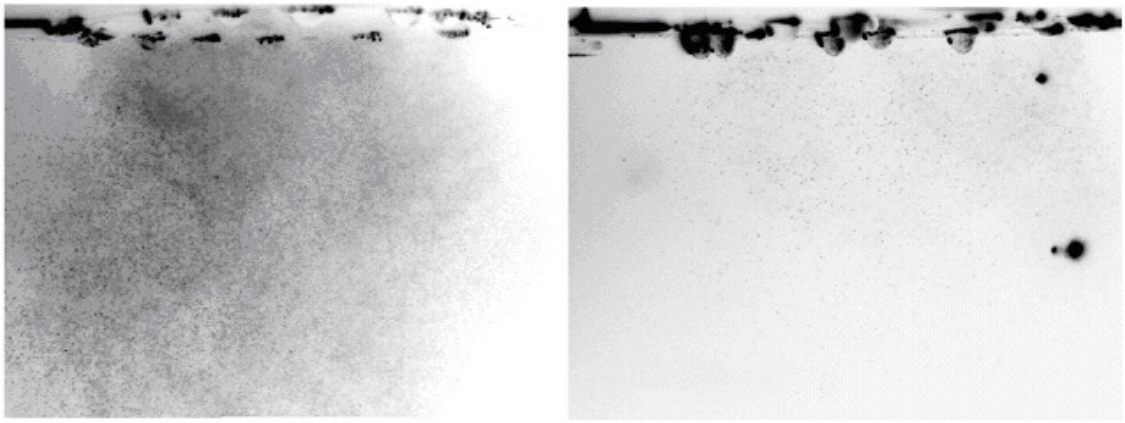

(b) (d)

Figure A7. Spray structure for 4" diffuser with (a) 30, (b) 45, (c) 60, and (d) blank swirler.

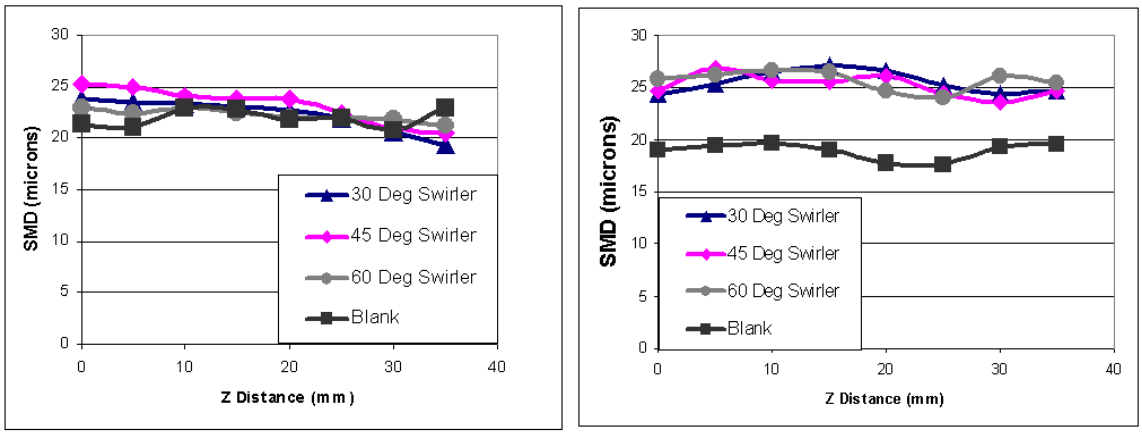

(a) (b)

Figure A8. Radial SMD distribution for (a) 4-inch (b) 6-inch diffuser

The Urea-SCR System: Test Conditions and Geometry

The following work involves the simulation of the urea injection and SCR system. Figure A9 and A10 shows the geometry that will be studied, short and long conical sections as well as the flap mixer provided by Bosch Corporation. The Urea-SCR system has processes similar to the reformer fuel/air mixer where the issues of flow distribution (atomization, vaporization, mixing) and pressure drop are critical factors. A combination of CFD & Laser Diagnostics in conjunction with experimental data will help guide design to improve the flow distribution and Pressure Drop in Urea-SCR and DPF aftertreatment systems.

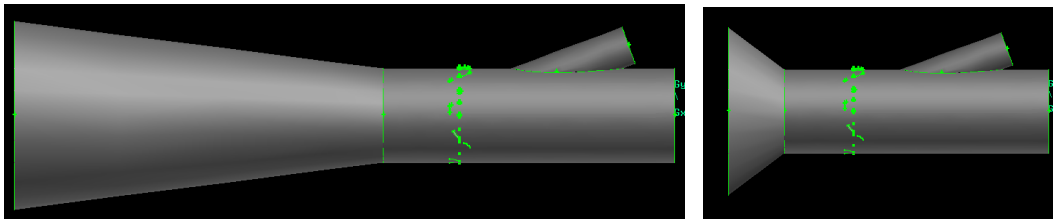

(a) (b)

Figure A9. Geometry with (a) long conical inlet and (b) short conical inlet before catalyst

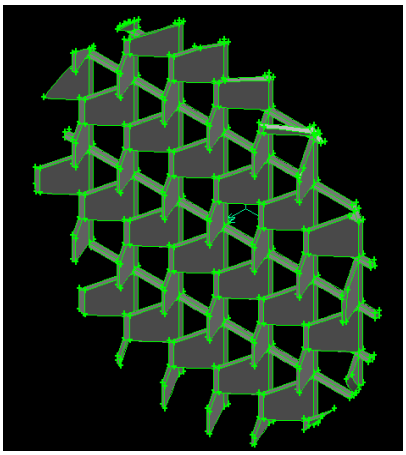

Figure A10. Geometry of the flap mixer (isometric view)

The simulation will use experimental data from the light duty 2.8L diesel engine [59], and optimize the urea injection and SCR system. Simulation test conditions are shown in the following table.

Test	Long/short Conical Section	Speed (rpm)	BMEP (bar)	Exhaust Temperature (C)	Exhaust Flow Rate (kg/s)
AS AL	Short Long	1200	3.58	230	61.73
BS BL	Short Long	1600	1.97	261	70.85
CS CL	Short Long	1600	3.62	312	79.46
DS DL	Short Long	1600	8.29	408	123.73

Table A1. Simulation Test Conditions of Urea-SCR System

Simulation results will focus on the effect of urea injection droplet size and distribution before the catalyst as well as pressure drop and velocity profiles within the urea reductant pipe before the SCR catalyst.

APPENDIX B: NOMENCLATURE AND ABBREVIATIONS

ARHR	Apparent Rate of Heat Release
aTDC	After Top Dead Center
B20	20% Biodiesel Blend with 80% Ultra Low Sulfur Diesel Fuel
BDC	Bottom Dead Center
BSFC	Brake Specific Fuel Consumption
BSN	Bosch Smoke Number
bTDC	Before Top Dead Center
CAD	Crank Angle Degree
CO	Carbon Monoxide
CO2	Carbon Dioxide
COV	Coefficient of Variance
ECM	Engine Control Module
ECU	Engine Control Unit
EGR	Exhaust Gas Recirculation
FA	Fatty Acids
FAME	Fatty Acids Methyle Ester

HC	Hydrocarbon
ID	Ignition Delay
IMEP	Indicated Mean Effective Pressure
ISFC	Indicated Specific Fuel Consumption
LHV	Lower Heating Value
LPPC	Location of Peak of Premixed Combustion
LTC	Low Temperature Combustion
LNOxC	Low NOx Combustion
NO	Nitric Oxide
NOx	Oxides of Nitrogen
PM	Particulate Matter
RPM	Revolution Per Minute
SME	Soy Methyl Ester
SOI	Start of Injection
TDC	Top Dead Center
THC	Total Unburned Hydrocarbon
ULSD	Ultra Low Sulfur Diesel Fuel

VOF Volatile Organic Fractions

REFERENCES

1. Amann, C.A.a.S., D. C. , *Diesel Particulates - What They Are and Why.* Aerosol Sci Technol., 1982. **1**: p. 73-101.
2. Knothe, G., Van Gerpen J., and Jurgen Krahl, *The Biodiesel Handbook*. 2005, Champaign, IL: AOCS Press.
3. Freedman, B., E.H. Pryde, *Fatty Esters from Vegetable Oils for Use as a Diesel Fuel*, in *Vegetable Oil Fuels: Proc. International Conference on Plant and Vegetable Oil as Fuels*. 1982, ASAE: Fargo, ND. p. p. 117-122.
4. Kusy, P.F., *Transesterification of Vegetable Oils for Fuels*, in *Vegetable Oil Fuels: Proc. International Conference on Plant and Vegetable Oils as Fuels*. 1982, ASAE: Fargo, ND. p. p. 127-130.
5. Hassett, D.J., R.A. Hasan, *Sunflower Oil Methyl Ester as Diesel Fuel*, in *Vegetable Oil Fuels: Proc. International Conference on Plant and Vegetable Oils as Fuels*. 1982, ASAE: Fargo, ND. p. p. 123-12.
6. Fort, E.F., Blumberg, P.N., Staph, H.E., and J.J. Staudt, *Evaluation of Cottonseed Oils as Diesel Fuel.* SAE, 1982(820317).
7. Hawkins, C.S., Fuls, J., and F.J.C. Hugo, *Sunflower oil esters: an alternative fuel for direct injction diesel engines.* SAE, 1983(831356).
8. Van Gerpen, J., Shanks, B., Pruszko,R., Clements, D., Knothe, G. , *Biodiesel Production Technology*. 2004, National Renewable Energy Laboratory.

9. Allinger, N., Cava,M., De Jongh,D., Johnson,C., Lebel,N., Stevens,C., *Organic Chemistry*. 2 ed. 1976, Boston: McGraw Hill.

10. Bruice, P.Y., *Organic Chemistry*. 3 ed. 2001, New Jersey: Prentice Hall.

11. Carey, F., *Organic Chemistry*. 4 ed. 2000, Boston: McGraw Hill.

12. NBB. 2008 [cited; Available from: www.biodiesel.org.

13. Anastopoulos, G., Lois, E., Karonis, D., Kalligeros, S., and F. Zannikos, *Impact of Oxygen and Nitrogen Compounds on the Lubrication Properties of Low Sulfur Diesel Fuels.* Energy 2005. **30**: p. 415-426.

14. Barbour, R.H., Rickeard, D.J., and N.G. Elliott, *Understanding Diesel Lubricity.* SAE, 2000(2000-01-1918).

15. Wadumesthrige, K., Ara, M., O. Salley, S., and Ng, K.Y.S., *Investigation of Lubricity Characteristics of Biodiesel in Petroleum and Synthetic Fuel.* Energy & Fuels, 2009. **23**: p. 2229-2234.

16. Kinast, J.A., *Production of Biodiesels from Multiple Feedstocks and Properties of Biodiesels and Biodiesel/Diesel Blends*. 2003, National Renewable Energy Laboratory.

17. Tang, H., Salley, S., Ng, S.K.Y., *Fuel Properties and precipitate formation at low temperature in soy-, cottonseed-, and poultry fat-based biodiesel blends.* Fuel, 2008. **87**.

18. Heywood, J.B., *Internal Combustion Engine Fundamentals*. 1988, New York: McGraw-Hill, Inc.

19. Tat, M., and J. Van Gerpen, *Physical Properties and Compostion Detection of Biodiesel-Diesel Fuel Blends*, in *2002 ASAE Annual International Meeting/CIGR XV World Congress*. 2002.

20. McCormick, R., Tennant, C., Hayes, R., Black, S., Ireland, J., McDaniel, T., Williams, A., Frailey, M., and Sharp, C., *Regulated Emissions from Biodiesel Tested in Heavy-Duty Engines Meeting 200 Emission Standards.* SAE, 2005. **2005-01-2200**.

21. McCormick, R., M.S. Graboski, T. Alleman, A. Herring, and K. Tyson, *Impact of Biodiesel Source Material and Chemical Structure on Emissions of Criteria Pollutants from a Heavy-Duty Engine.* Journal of Environ. Sci. Technol., 2001. **35**: p. 1742-1747.

22. EPA, *A Comprehensive Analysis of Biodiesel Impacts on Exhaust Emissions*. 2002.

23. Graboski, M.S., and R.L. McCormick, *Combustion of Fat and Vegetable Oil Derived Fuels in Diesel Engines.* Prog. Energy Combust. Sci., 1998. **24**: p. 125-164.

24. Sheehan, J., and V. Camobreco, J. Duffield, M. Graboski, H. Shapouri, *An Overview of Biodiesel and Petroleum Derived Diesel Life Cycles*. 1998, NREL.

25. Graboski, M., R. McCormick, T. Alleman, and A. Herring, *The Effect of Biodiesel Compostition on Engine Emissions from a DDC Series 60 Diesel Engine*. 2003, NREL/SR-510-31461.

26. Szybist, J.P., Alam, M., Boehman, A., *Biodiesel combustion, emissions and emission control.* Fuel Processing Technology, 2007. **88**: p. 679-691.

27. Cheng, A., Upanieks, A., and C. Mueller, *Investigation of the Impact of Biodiesel Fueling on NOx Emissions using an Optical Direct Injection Diesel Engine.* International Journal of Engine Research, 2006. **7**: p. 297-318.

28. Canakci, M., and J. Van Gerpen. *Yellow Grease Biodiesel, and Soybean Oil Biodiesel*. in *2001 ASAE Annual International Meeting*. 2001. Sacramento, CA: Paper No. 016050.

29. McCormick, R., Williams, A., Ireland, J., Brimhall, M., and Hayes, R., *Effects of Biodiesel Blends on Vehicle Emissions*, in *NREL/MP-540-40554*. 2006.

30. Zhang, Y.a.B., A., *Impact of Biodiesel on NOx Emissions in a Common Rail Direct Injection Diesel Engine.* Energy & Fuels, 2007. **21**: p. 2003-2012.

31. Nagaraju, V., Henein, N., Quader, A., Lai, M-C, Wu., M-C, and Bryzik, W., *Effect of Biodiesel (B-20) on Performance and Emissions in a Single Cylinder HSDI Diesel Engine.* SAE, 2008. **2008-01-1401**.

32. Peterson, A., Lee, P-I., Lai, M-C, Wu, M-C, and C. Dimaggio, *Effects of B20 on Combustion, Emissions and Performance of a Light-Duty Diesel Engine*, in *ASME ICE Spring Technical Conference*. 2009: Milwaukee, WI.

33. Acharya, K., Dahhodwala, M., Bryzik, W., Henein, and Sova, N., *The Effect of Different Biodiesel Percent Blends on Autoignition, Combustion, Performance and Engine-out Emissions from a Single Cylinder HSDI Diesel Engine.* SAE, 2009. **2009-01-0489**.

34. Sharp, C.A., Howell, S.A., Jobe, J., *The Effect of Biodiesel Fuels on Transient Emissions from Modern Diesel Engines, Part I Regulated Emissions and Performance.* SAE, 2000(2000-01-1967).

35. Boehman, A.L., Song, J., and Mahabubul Alam, *Impact of Biodiesel Blending on Diesel Soot and the Regeneration of Particulate Filters.* Energy & Fuels, 2005. **19**: p. 1857-1864.

36. Wal, R.V., Yezerets, A., Currier, N., Kim, D.H., Wang, C.M, *HRTEM Study of diesel soot collected from diesel particulate filters.* Carbon, 2007. **45**: p. 70-77.

37. Jung, H., Kittelson, D., Zachariah, M., *Characteristics of SME Biodiesel-fueled Diesel Particle Emissions and the Kinetics of Oxidation.* Enviornmental Science and Technology, 2006. **40**: p. 4949-4955.

38. Song, J., Alam, M., Boehman, A., Kim, U., *Examination of the Oxidation Behavior of Biodiesel Soot.* Combustion and Flame, 2006. **146**: p. 589-604.

39. Williams, A., McCormick, R.L., Hayes, R.R., Ireland, J., and Howard Fang, *Effect of Biodiesel Blends on Diesel Particulate Filter Performance.* SAE, 2006(2006-01-3280).

40. Ladommatos N., A., S., Zhao, H., Hu, Z., *Effects of EGR on Heat Release in Diesel Combustion.* SAE, 1998(980184).

41. Kim Y.M., K.Y.D., Kim H.J., Kim S.W., *Numerical Study on Ignition and Combustion Process of a Diesel Spray in EGR Enviornment.* SAE, 1996. **960874**.

42. Desantes, J., Arregle, J., Molina, S., and Lejeune, M, *Influence of the EGR Rate, Oxygen Concentration and Equivalent Fuel/Air Ratio on the Combustion*

Behavior and Pollutant Emissions of a Heavy-Duty Diesel Engine. SAE, 2000. **2000-01-1813**.

43. Baik, D.S., *Combined Effects of BD20, Low Sulfur Diesel Fuel and Diesel Oxidation Catalyst in a HD Diesel Engine.* International Journal of Automotive Technology, 2006. **7**(6): p. 635-658.

44. Masoudi, M., *Pressure Drop of Segmented Diesel Particulate Filters.* SAE, 2005. **2005-01-0971**(2005-01-0971).

45. Fang, H.L., and DaCosta, H.F.M., *Urea Thermolysis and NOx Reduction With and Without SCR Catalyst.* Applied Catalytic B: Environmental, 2003. **46**: p. 17-34.

46. Fisher, G.B., DiMaggio, C.L., and Sommers, J.W., *NOx Reactivity Studies of Prototype Catalysts for a Plasma-Catalyst Aftertreatment System.* SAE, 1999. **1999-01-3685**.

47. Blackburn, J.H., Pinchin, R., Nobre, J.I.T, Crichton, B.A.L., and H.W. Cruse, *Performance of Lubricating Oils in Vegetable Oil Ester-Fuelled Diesel Engines.* SAE, 1983(831355).

48. Andreae, M., Fang, H. and K. Bhandary, *Biodiesel and Fuel Dilution of Engine Oil.* SAE, 2007(2007-01-4036).

49. Parks, J., Partridge, B., and S. Whitacre, *Rapid In Situ Measurement of Fuel Dilution of Oil in a Diesel Engine using Laser-Induced Florescence Spectroscopy.* SAE, 2007(2007-01-4108).

50. Kimura, S., Aoki, O., Kitahara, Y., Aiyoshizawa, E., *Ultra-Clean Combustion Technology Combining a Low-Temperature and Premixed Combustion Concept for Meeting Future Emission Standards.* SAE, 2001. **2001-01-0200**.

51. Kawamoto, K., Araki, T., Shinzawa, M., Kimura, S., Koide, S., Shibuya, M., *Combination of Combustion Concept and Fuel Property for Ultra-Clean DI Diesel.* SAE, 2004. **2004-01-1868**.

52. Akihama, K., Takatori, Y., Inagaki, K., Sasaki, S., Dean, A., *Mechanism of the Smokeless Rich Diesel Combustion by Reducing Temperature.* SAE, 2001(2001-01-0655).

53. Kmimoto, T., Bae, M., *High Combustion Temperature for the Reduction of Particulate in Diesel Engines.* SAE, 1988. **880423**.

54. Zheng, M., Han, X., Tan, Y., Kobler, M., Ko, S-J., Wang, M., Mulenga, M., and Tjong, J., *Low Temperature Combustion of Neat Biodiesel Fuel on a Common-rail Diesel Engine.* SAE, 2008. **2008-01-1396**.

55. Zheng, M., Mulenga, M., Reader, T., Wang, M., and David Ting, *Influence of Biodiesel Fuel on Diesel Engine Performance and Emissions in Low Temperature Combustion.* SAE, 2006. **2006-01-3281**.

56. Fang, T., Lin, YC., Foong, TM., and Lee, CF., *Spray and Combustion visualization in an optical HSDI diesel engine operated in low-temperature combustion mode with biodiesel and diesel fuels.* SAE, 2008. **2008-01-1390**.

57. Northrop, W., Bohac, S., and Dennis Assanis, *Premixed low temperature combustion of biodiesel and blends in a high speed compression ignition engine.* SAE, 2009. **2009-01-0133**.

58. Karra, P., Veltman, M., and S.C. Kong, *Characteristics of Engine Emissions Using Biodiesel Blends in Low-Temperature Combustion Regimes.* Energy Fuels, 2008. **22**(6): p. 3763-3770.

59. Lee, P.-I., Lai, M-C., Peterson, A., Casarella, M., and Wu, M-C., *Effects of Fuels and Catalyst Entrance Section Length on the Performance of Urea SCR in a Light Duty Diesel Engine.* SAE, 2010. **2010-01-1173**.

60. Tatur, M., Nanjundaswamy, H., and Dean Tomazic, *Effects of Biodiesel Operation on Light-Duty Tier 2 Engine and Emission Control Systems.* SAE, 2008(2008-01-0080).

61. Senatore, A., Cardone, M., Allocca, L., and Vitolo, S., *Experimental Characterization of a Common Rail Engine Fuelled with Different Biodiesel.* SAE, 2005(2005-01-2207).

62. Fang, H.L. and H.F.M. DaCosta, *Urea thermolysis and NOx reduction with and without SCR catalysts.* Applied Catalytic B: Environmental, 2003. **46**: p. 17-34.

63. Fisher, G.B., C.L. DiMaggio, and J.W. Sommers, *NOx Reactivity Studies of Prototype Catalysts for a Plasma-Catalyst Afterment system.* SAE, 1999-01-3685.

64. Okubo, M., et al., *Simultaneous Reduction of Diesel Particulate and NOx Using Oxygen-Poor Nonthermal Plasma Application*, in *Industry Applications*

Conference. 42nd IAS Annual Meeting. 2007, IEEE: New Orleans, LA. p. 1864-1870.

65. *Catalyst-Based Diesel Particulate Filters and NOx Adsorbers: A Summary of the Technologies and the Effects of Fuel Sulfur.* Manufacturers of Emission Controls Association, 2000.

66. Ciardelli, C., et al., *Reactivity of NO/NO2-NH3 SCR system for diesel exhaust aftertreatment: Identification of the reaction network as a function of temperature and NO2 feed content.* Applied Catalytic B: Environmental, 2007. **70**: p. 80-90.

67. Tronconi, E., et al., *Redox features in the catalytic mechanism of the "standard" and "fast" NH3-SCR of NOx over a V-based catalyst investigated by dynamic methods.* Journal of Catalysis, 2007. **245**: p. 1-10.

68. Helden, R.c., et al., *Optimization of Urea SCR deNOx Systems for HD Diesel Engines.* SAE, 2004-01-0154.

69. Czerwinski, J., et al., *Testing of Combined DPF+SCR Systems for HD-retrofitting - VERTdePN.* SAE, 2009-01-0284.

70. He, Y., et al., *Opportunities and Challenges for Blended 2-Way SCR/DPF Aftertreatment Technologies.* SAE, 2009-01-0274.

71. Lee, J.H., M.J. Paratore, and D.B. Brown, *Evaluation of Cu-Based SCR/DPF Technology for Diesel Exhaust Emission Control.* SAE, 2008-01-0072.

72. Enderle, C., G. Vent, and M. Paule, *BLUETEC Diesel Technology - Clean, Efficient and Powerful.* SAE, 2008-01-1182.

73. Acharya, R., M. Alam, and A.L. Boehman, *Fuel System Interaction Effects on Urea-SCR Control of NOx in Diesel Exhaust Afterment.* SAE, 2006-01-0638.

74. Sullivan, J.A. and O. Keane, *A combination of NOx trapping materials and urea-SCR catalysts for use in the removal of NOx from mobile diesel engines.* Applied Catalytic B: Environmental, 2006. **70**: p. 205-214.

75. Muench, J., R. Leppelt, and R. Dotzel, *Extruded Zeolite Based Honeycomb Catalyst for NOx Removal from Diesel Exhaust.* SAE, 2008-01-1024.

76. Johnson, T., *Diesel Engine Emissions and Their Control.* Platinum Metals Review, 2008. **52**(1): p. 23-37.

77. Shost, M., et al., *Monitoring, Feedback, and Control of Urea SCR Dosing Systems for NOx Reduction: Utilizing an Embedded Model and Ammonia Sensing.* SAE, 2008-01-1325.

78. Chatterjee, D., et al., *Numerical Simulation of DOC + DPF + SCR Systems: DOC Influence on SCR Performance.* SAE, 2008-01-0867.

79. Schuler, A., et al., *Dynamic Model for the Selective Catalyric Reduction of NO with NH3 on Fe-Zeolite Catalysts.* SAE, 2008-01-1323.

80. Chen, M. and S. Williams, *Modelling and Optimization of SCR-Exhaust Aftertreatment Systems.* SAE, 2005-01-0969.

81. Lai, M.-C., et al., *Numerical and Experimental Characterizations of Automotive Catalytic Converter Internal Flows.* Journal of Fluids and Structures, 1992. **6**(4): p. 451-470.

82. Kim, J.Y., et al., *Flow Distribution and Pressure Drop in Diffuser-Monolith Flows.* Journal of Fluids Engineering 1995. **117**(3): p. 362-368.

83. Oesterle, J.J., et al., *Urea Systems in Focus - New Challenges and Solutions in the Development of Car and Commercial Vehicle Exhaust Systems.* SAE, 2008-01-1186.

84. Wurzenberger, J.C. and R. Wanker, *Multi-Scale SCR Modeling, 1D Kinetic Analysis and 3D System Simulation.* SAE, 2005-01-0948.

85. Peterson, A., et al., *Impact of Biodiesel Emission Products from a Multi-Cylinder Direct Injection Diesel Engine on Particulate Filter Performance.* SAE, 2009-01-1184.

86. Peterson, A.M., et al., *Effects of B20 on Emissions and the Performance of a Diesel Particulate Filter in a Light-Duty Diesel Engine*, in *Internal Combustion Engine Division (ICED) of ASME 2009 Fall Technical Conference*. ICEF2009-14096, ASME: Lucerne, Switzerland.

87. Peterson, A., et al., *Effects of B20 on Combustion, Emissions and Performance of a Light-Duty Diesel Engine* in *Internal Combustion Engine Division (ICED) of ASME 2009 Spring Technical Conference*. ICES2009-76167, ASME: Milwaukee, Wisconsin.

88. Tang, W., et al., *A Lumped/1D combined Approach for Modeling Wall-Flow Diesel Particulate Filters - Applicable to Integrated Engine/Afterreatment Simulation.* SAE, 2001. **2001-01-3971**.

89. Young, D., Warren, C., and Kishor P. Gadkaree, *Silicon Carbide for Diesel Particulate Filter Applications: Material Development and Thermal Design.* SAE, 2002. **2002-01-0324**.

90. Lai, M.-C., Chur T-H., Zhu, G., Sun, H., Tacina, R., and Chun K., *JP-A Fuel Evaporation Analysis in Conical Flame Tube Injector.* AIAA, 1991. **91-0345**.

91. Tacina, R., *Low NOx Potential of Gas Turbine Engines.* AIAA, 1990. **90-0550**.

92. Sun, H., Chue, T. H., Lai M-C., and Tacina R., *Atomization Characteristics of Capillary Fuel Injection inside a Venturi Nozzle.* Atomization and Sprays, 1997. **7**: p. 245-265.

93. Im, K., Kim, H., Lai, M-C., and Tacina, R., *Parametric Studies of Swirl Venturi Tube Injectors.* J. Propulsion and Power, 2001. **17**(3): p. 717-727.

94. Zhu, G., Lai, M-C., and Xiong, T. *Numerical and Experimental Study of the Non-Reacting Flowfield in a Cyclonic Combustor*. in *ASME COGEN TURBO POWER*. 1992. Houston, TX: ASME.

95. Zhu, G., Lai, M-C., and Lee, T., *A Parametric Study of Penetration and Mixing of Radial Jets in Necked-Down cylindrical Crossflow.* J. Propulsion and Power, 1995. **11**(2): p. 252-260.

96. Talpallikar, M.V., Smith C.E., Lai, M.C., and Holdeman, J., *CFD Analysis of Jet Mixing in Low NOx Flametube Combustors.* J. Engineering in Gas Turbine & Power, 1992. **114**: p. 416-424.

97. Peterson, A., Subramaniyam, S., Lai, M-C., Tacina, R., Tomsik, T., Yen, J., Lee, C-M., *Optimization of Swirler-Venturi Mixer Geometry for Fuel Reformer Application.* AIAA, 2005.

98. Subramaniyam, S., Mulemane, A., Im, K-S., Lia, M-C., Tacian, R., Tomsik, T., and Lee, C-M., *Spray and Fuel-Air Mixing of the Swirler/Venturi Mixers for LPP Combustor and Fuel Reformer Applications*, in *AIAA 42nd Aerospace Science Meeting*. 2004: Reno, NV.

99. Sun, H., Lai M-C., and Tacina R. *Exciplex LIF Visualization of Fuel Spray Vaporization Process inside a Venturi Nozzle*. in *1993 Joint Technical Meeting of Central and Eastern States Section, The Combustion Insitute*. 1993. New Orleans, LA.

ABSTRACT

THE EFFECT OF BIODIESEL BLENDS ON A MULTI-CYLINDER ENGINE AND TH IMPACT ON AFTERTREATMENT

By

AMY PETERSON

August 2013

Advisor: Dr. Ming-Chia Lai

Major: Mechanical Engineering

Degree: Doctor of Philosophy

Recently, topics including global warming, increased environmental awareness, recycling, and organically produced meat and vegetables have been prevalent in the media and research arenas. The rapidly increasing cost for fossil fuels and the pursuit of environmental conservation has brought about the interest in a renewable and clean burning fuel, specifically biodiesel. Biodiesel, or vegetable oil ester as it was originally referred to, has been improving and progressing since the early 1900's. Fortunately, significant advancement in the understanding of raw vegetable oil as a fuel as well as converting it to ethyl or methyl esters, now known as biodiesel, has been evolving for nearly a century after.

The objective of this study is predicated on the potential marketing of biodiesel blends, up to 20% by volume, without modification to standard production available engines to be used by the average consumer. The NextEnergy Biodiesel program is a

collaborative effort involving a variety of disciplines and expertise. Objectives include developing manufacturing methods for soy-based biodiesel, evaluating and recording parameters such as cetane number, oxidative stability, and lubricity made from different feedstocks to be used for engine testing. The evaluations of these selected fuels are then blended with ULSD and tested in single and multi-cylinder engines. The proceeding work specifically focuses on results from a multi-cylinder engine coupled with a diesel oxidation catalyst, diesel particulate filter and a selective catalytic reduction catalyst and the effect that biodiesel blends has on their performance and effectiveness.

AUTOBIOGRAPHICAL STATEMENT

AMY MICHELLE PETERSON

Education

9/02 – 12/12 Ph.D. Mechanical Engineering, *Wayne State University, Detroit MI*

Dissertation: "The Effect of Biodiesel Blends on a Multi-Cylinder Engine and the Impact on Aftertreatment"

Advisor: Dr. Ming-Chia Lai

9/00 – 8/02 M.S. Mechanical Engineering, *University of Michigan-Dearborn, Dearborn MI*

9/93 – 5/99 B.S. Mechanical Engineering, *University of Michigan-Dearborn, Dearborn MI*

B.S. Engineering Mathematics, *University of Michigan-Dearborn, Dearborn MI*

Research and Teaching Experience

5/09 – 8/09 Instructor, ME 4300 Thermal Fluid Design Course, *Wayne State University, Detroit MI*

9/05 – 5/08 Graduate Research Assistant/Teaching Assistant, *Wayne State University, Detroit MI*

Publications

1. SAE: 2010-01-1173, SAE: 2009-01-1184
2. Effects of B20 on the Aftertreatment System of a Light-Duty Diesel Engine ASME J. Engineering in Gas Turbine & Power, 132, 112802 (2010)
3. Optimization of Swirler-Venturi Mixer Geometry for Fuel Reformer Application AIAA 2005
4. Numerical Simulation of Coolant Electrolysis in Composite Plate PEM Fuel Cell Stacks FUELCELL 2005-74095.
5. Numerical Simulation of Water Management and Coolant Electrolysis in Composite Plate PEM Fuel Cell Stacks, Fuel Cell Seminar, 2006
6. Effects of B20 on Combustion, Emissions and Performance of a Light-Duty Diesel Engine, in ASME ICE Spring Technical Conference. 2009